Supporting information for the manuscript:

Effect of nuclearity and reduction state of central ligand on magnetic properties of hexaazatrinaphthylene-based cobalt(II) and iron(II) complexes: from extremely weak to record-breaking antiferromagnetic exchange interaction†

Maxim V. Mikhailenko,[a] Vladislav V. Ivanov,[a] Maxim A. Faraonov,[a] Aleksey V. Kuzmin,[b] Salavat S. Khasanov,[b] Ilya A. Yakushev,[c] Natalia N. Breslavskaya,[c] Elena N. Timokhina,[d] Tatiana Yu. Astakhova,[d] Akihiro Otsuka,[e] Hideki Yamochi,[e] Hiroshi Kitagawa[e] and Dmitri V. Konarev *[a]

[a]Federal Research Center of Problems of Chemical Physics and Medicinal Chemistry RAS, Chernogolovka, Moscow region, 142432 Russia; E-mail: konarev3@yandex.ru;

[b]Institute of Solid State Physics RAS, Chernogolovka, Moscow region, 142432 Russia;

[c]Kurnakov institute of General and Inorganic Chemistry, Russian Academy of Sciences, Moscow, Russia;

[d]Emanuel Institute of Biochemical Physics, RAS, Moscow, Russia;

[e]Division of Chemistry, Graduate School of Science, Kyoto University, Sakyo-ku, Kyoto,606-8502, Japan

Table of contents

Experimental section S3
IR-spectra of the complexes S12
Optical spectra S16
Crystal structures S19
Spin Hamiltonians for the fitting of magnetic data by PHI S27
Magnetic data S28
Computational details S63

Experimental section

Materials

Hexaazatrinaphthylene (HATNA) was obtained from hexaketocyclohexane octahydrate (Aldrich, $C_6O_6 \cdot 8H_2O$, >97%) and 4,5-diaminophthalonitrile (>98%, TCI reagents), whereashexaazatrianthracene (HATA) was obtained from hexaketocyclohexane octahydrate and 2,3-diaminonaphthalene (>98%, Aldrich) following previously reported general procedures[1-3]. Cryptand[2.2.2] (>98%) and anhydrous crystal violet (CVCl) were purchased from TCI reagents. Potassium graphite (KC_8) was purchased from Strem. Anhydrous $FeCl_2$ (>98%), $CoCl_2$ (>99%), CoI_2 (>95%) were purchased from Strem. *o*-Dichlorobenzene ($C_6H_4Cl_2$) was distilled over CaH_2 under reduced pressure, and *n*-hexane was distilled over Na/benzophenone under Ar. Solvents were degassed and stored in an MBraun 150B-G glove box. Compounds **1**–**9** were synthesized and stored in the glove box under a controlled atmosphere containing <1 ppm of H_2O and O_2. KBr pellets used for the IR and Ultraviolet (UV)–visible–near-infrared (NIR) analyses were prepared in the glove box.

General

The UV–visible–NIR spectra were measured using the KBr pellets with a PerkinElmer Lambda 1050 spectrometer in the 250–2500 nm range. The Fourier-transform infrared (FTIR) spectra (400–7800 cm^{-1}) were measured using the KBr pellets with a PerkinElmer Spectrum 400 spectrometer. The electron paramagnetic resonance (EPR) spectra were recorded for the polycrystalline samples **1**, **2** and **4-11** at room temperature with a JEOL JES-TE 200 X-band electron spin resonance spectrometer. A quantum design MPMS-XL superconducting quantum interference device (SQUID) magnetometer was used to measure the static magnetic susceptibilities of **1**, **2** and **4-11** at a 1 kOe magnetic field upon heating from 1.9 to 300 K and subsequent cooling from 300 to 1.9 K. The sample holder contribution and core temperature-independent diamagnetic susceptibility (χ_d) were subtracted from the experimental data. The χ_d

values were estimated by extrapolating the high-temperature data (60–300 K) and fitting the data with the expression: $\chi_M = C/(T - \Theta) + \chi_d$, where C is the Curie constant, and Θ is the Weiss temperature.

Synthesis

Crystals of **1**–**9** were synthesized using a diffusion technique. A reaction mixture was filtered into a 1.8-cm-diameter, 50-mL glass tube with a ground glass plug, and then 30 mL of *n*-hexane was layered over the solution. Slowly mixing the solutions over two months yielded precipitation of crystals. The solvent was then decanted from the crystals and washed with *n*-hexane. In all syntheses crystals have the same shape and color and their testing by X-ray diffraction indicates that they belong to one crystal phase.

$[(Co^{II}I_2)(HATNA)]^0 \cdot C_6H_4Cl_2$ (**1**). A mixture of HATNA (16.0 mg, 0.042 mmol) and three equivalents of $Co^{II}I_2$ (39 mg, 0.126 mmol) was stirred in 17 mL of *o*-dichlorobenzene for 24 h at 60°C. The ligand ~~is~~ was completely dissolved leaving some nonreacted black $Co^{II}I_2$ and the color of the solution turned dark brown. Solution was cooled down to room temperature and filtered in the diffusion tube. After slow mixing with *n*-hexane during one month black good quality prisms of **1** were obtained in the 73% yield. Composition determined by X-ray diffraction indicates that only one $Co^{II}I_2$ is coordinated to HATNA in spite of three equivalents of this reagent are used in the starting mixture. Microprobe analyses on the crystals of **1** confirmed the determined composition (the Co : Cl : I ratio is 1.0 : 2.1 : 2.0). Elemental analysis for **1**: $C_{30}H_{16}Cl_2CoI_2N_6$, M_r = 844.12: Calc. C = 42.68; H = 1.90, N = 9.95; Cl = 8.41; Found. C = 42.38; H = 1.82, N = 9.88; Cl = 8.29.

Complexes $\{(K^+)(crypt)\}\{(Co^{II}I_2)_2(HATNA)\}^- \cdot 2.75C_6H_4Cl_2$ (**2**) and $\{(K^+)(crypt)\}\{(Co^{II}Cl_2)_2(HATNA)\}^- \cdot 2.5C_6H_4Cl_2$ (**3**) were obtained similarly. A mixture of HATNA (16.0 mg, 0.042 mmol) with two equivalents of $Co^{II}I_2$ (26 mg, 0.084 mmol) for preparation of **2** or two equivalents of $Co^{II}Cl_2$ (11 mg, 0.0846 mmol) for preparation of **3** were stirred in 17 mL of *o*-dichlorobenzene for 24 h at 60°C providing deep brown (**2**) or light brown (**3**) mixtures. Half equivalent of cryptand[2.2.2] was added (8.0 mg, 0.021 mmol) together with an excess of potassium graphite as a reductant (16 mg, 0.1185 mmol). The mixture was stirred for another 24 h at 60°C and the color of the solution turned to brownish green. Solutions were cooled down to the room temperature and filtered into the tubes for the diffusion. Crystals were obtained as black bulks with the 65% and 14% yields, respectively. Crystals of **2** were obtained as a collection of good quality single crystals and their composition was determined by X-ray diffraction on single crystal. Microprobe analysis on the crystals of **2** confirmed the determined composition (the Co : Cl : I ratio is 1.0 : 2.8 : 2.0). Elemental analysis for **2**: $C_{58.50}H_{59}Cl_{5.50}Co_2I_4KN_8O_6$, M_r = 1829.67: Calc. C = 38.40; H = 3.22, N = 6.12; Found. C = 38.24; H = 3.12, N = 5.98. Crystals of **3** were obtained with small yield and we determined only their crystal stricture to study the effect of substitution of iodide to chloride at the Co^{II} ions.

Crystals of $\{(K^+)(crypt)\}\{(Fe^{II}I_2)_2(HATNA)\}^- \cdot 3C_6H_4Cl_2$ (**4**) were obtained similarly. A mixture of HATNA (16.0 mg, 0.042 mmol) with two equivalents of $Fe^{II}I_2$ (26 mg, 0.084 mmol) were stirred in 17 mL of *o*-dichlorobenzene for 24 h at 60°C providing deep brown mixture. Half equivalent of cryptand[2.2.2] was added (8.0 mg, 0.021 mmol) together with an excess of potassium graphite as a reductant (16 mg, 0.1185 mmol). The mixture was stirred for another 24 h at 60°C and the color of the solution turned to brownish green. Solutions were cooled down to the room temperature and filtered into the tubes for the diffusion. Crystals were obtained as black bulks with the 53% yield. Crystals were obtained as a collection of good quality single crystals and by X-ray diffraction was shown that they are isostructural to **2**. Microbrobe analysis on the crystals of **4** confirmed the determined composition (the Fe : Cl : I ratio is 1.0 : 2.9 : 2.0). Elemental analysis for **4**: $C_{60}H_{60}Cl_6Fe_2I_4KN_8O_6$, M_r = 1866.44: Calc. C = 38.61; H = 3.21, N = 6.00; Found. C = 38.44; H = 3.05, N = 5.89.

Complex $\{(K^+)(crypt)\}\{(Co^{II}I_2)_2(HATA)\}^- \cdot C_6H_4Cl_2$ (**5**) was obtained by the folloving procedure: a mixture of HATA (22.4 mg, 0.042 mmol) with two equivalents of $Co^{II}I_2$ (26 mg, 0.084 mmol) were stirred in 17 mL of *o*-dichlorobenzene for 24 h at 60°C providing brown color of the mixture. Half equivalent of cryptand[2.2.2] was added (8.0 mg, 0.021 mmol) together with an excess of potassium graphite as a reductant (16 mg, 0.1185 mmol). The mixture was stirred for another 24 h at 60°C and the color of the solution turned to brownish green. Solution was cooled down to room temperature and filtered into the tube for diffusion. Crystals were obtained as black bulks with the 72% yield. Crystals of **5** were obtained as good quality crystals and their composition was determined by X-ray diffraction on single crystal. Microprobe analysis (the Co : Cl : I ratio is 1.0 : 1.2 : 2.0) confirmed the determined composition. Elemental analysis for **4**: $C_{60}H_{58}Cl_2Co_2I_4KN_8O_6$, $M_r = 1722.60$: Calc. C = 41.83; H = 3.37, N = 6.50; Found. C = 41.65; H = 3.21, N = 6.44.

Compound $\{(K^+)(crypt)\}\{(Fe^{II}Cl_2)_3(HATNA)\}^{-}\cdot C_6H_{14}$ (**6**) was obtained via the interaction of HATNA (16.0 mg, 0.042 mmol) with three equivalents of $Fe^{II}Cl_2$ (17 mg, 0.1341 mmol) which were stirred in 17 mL of *o*-dichlorobenzene for 24 h at 60°C providing the formation of light brown solution. After that one equivalent of cryptand[2.2.2] was added (16.0 mg, 0.042 mmol) together with an excess of the reductant ~~s~~ potassium graphite (20 mg, 0.1481 mmol). The mixture was stirred for another 24 h at 60°C and the color of the solution turned to brownish green. Solution was cooled down to room temperature and filtered into the tube for the diffusion. Crystals were obtained as black blocks with the 72% yield. Complex **6** was obtained as good quality crystals and its composition was determined by X-ray diffraction on a single crystal. Microprobe analysis (the Fe : Cl ratio is 1.0 : 2.1) confirmed the determined composition. Elemental analysis for **6**: $C_{48}H_{62}Cl_6Fe_3KN_8O_6$, $M_r = 1266.40$: Calc. C = 45.49; H = 4.90, N = 8.84; Cl = 16.82; Found. C = 45.21; H = 4.71, N = 8.72; Cl = 16.71.

Compound $\{(K^+)(crypt)\}\{(Co^{II}Cl_2)_3(HATNA)\}^{-}$ (**7**) was obtained via the interaction of HATNA (16.0 mg, 0.042 mmol) with three equivalents of $Co^{II}Cl_2$ (17 mg, 0.1341 mmol) which were stirred in 17 mL of *o*-dichlorobenzene for 24 h at 60°C providing the formation of light brown solution. After that one equivalent of cryptand[2.2.2] was added (16.0 mg, 0.042 mmol) together with an excess of the reductant potassium graphite (20 mg, 0.1481 mmol). The mixture was stirred for another 24 h at 60°C and the color of the solution turned to brownish green. Solution was cooled down to room temperature and filtered into the tube for the diffusion. Crystals were obtained as black blocks with the 64% yield. Complex **7** was obtained as good quality crystals. It is isostructural to complex **6** with $Fe^{II}Cl_2$ but unit cell has smaller volume in comparison with **6**. Most probably that is due to smaller size of $\{(Co^{II}Cl_2)_3(HATNA)\}^{-}$ in comparison with Fe-containing analog in **6** and the absence of solvent C_6H_{14} solvent molecule (according to elemental analysis. Elemental analysis for **7**: $C_{42}H_{48}N_8O_6Co_3Cl_6K$, $M_r = 1189.5$: Calc. C = 42.41; H = 4.07, N = 9.42; Cl = 17.88; Found. C = 42.70; H = 4.07, N = 9.49; Cl = 18.04

Compound $\{(K^+)(crypt)\}_2\{(Fe^{II}Cl_2)_2(HATNA)\}^{2-}\cdot 3C_6H_4Cl_2$ (**8**) was obtained via the interaction of HATNA (16.0 mg, 0.042 mmol) with two equivalents of $Fe^{II}Cl_2$ (11 mg, 0.0868 mmol) which were stirred in 17 mL of *o*-dichlorobenzene for 24 h at 60°C providing the formation of light brown solution. Afterwards two equivalents of cryptand[2.2.2] was added (32.0 mg, 0.084 mmol) together with an excess of the reductants potassium graphite (28 mg, 0.2074 mmol). The mixture was stirred for another 24 h at 60°C and the color of the solution turned to deep red. Solution was cooled down to the room temperature and filtered into the tube for the diffusion. Crystals were obtained as black parallelepipeds with the 67% yield. Compound **8** was obtained as good quality crystals and its composition was determined by X-ray diffraction on single crystal. Microprobe analysis (the Fe : Cl ratio is 1.0 : 5.2) confirmed the determined composition. Compound is air-sensitive.

Compound $\{(K^+)(crypt)\}_2\{(Co^{II}I_2)_3(HATA)\}^{2-}\cdot 4C_6H_4Cl_2$ (**9**) was obtained via the interaction of HATA (22.4 mg, 0.042 mmol) with three equivalents of $Co^{II}I_2$ (39 mg, 0.126 mmol). They were stirred in 17 mL of *o*-dichlorobenzene for 24 h at 60°C providing the formation of dark brown solution. After that three equivalents of cryptand[2.2.2] was added (48.0 mg, 0.126 mmol) together with an excess of the reductants potassium graphite (36 mg, 0.2666 mmol). The mixture was stirred for another 24 h at 60°C and the color of the solution turned to deep red.

Solution was cooled down to room temperature and filtered into the tube for the diffusion. Crystals were obtained as black parallelepipeds with the 61% yield. Compound **9** was obtained as good quality crystals and its composition was determined by X-ray diffraction on single crystal. Microprobe analysis (the Co : Cl : I ratio is 1.0 : 2.7 : 2.1) confirmed the determined composition. Compound is air-sensitive. In spite of the employment of an excess of cryptand only dianionic species are formed indicating that this is maximal degree of reduction for potassium graphite as a reductant.

Compound $(CV^+)_2\{(Co^{II}Cl_2)_3(HATA)\}^{2-}\cdot 4C_6H_4Cl_2$ (**10**) was obtained via the interaction of HATA (22.4 mg, 0.042 mmol), three equivalents of $Co^{II}Cl_2$ (17 mg, 0.1341 mmol), two equivalents of CVCl (34.0 mg, 0.084 mmol) and an excess of potassium graphite as a reductant (30 mg, 0.222 mmol) were stirred in 17 mL of *o*-dichlorobenzene for 48 h at 60°C providing deep red-blue solution. It was cooled down to room temperature and filtered into the tube for the diffusion. Black plates were obtained with gold luster characteristic for the salts of CV^+. The yield is 74%. Compound **10** was obtained as good quality crystals having the same shape and color and composition of the compound was determined by X-ray diffraction analysis on single crystal. Several crystals tested from the synthesis show the same unit cell parameters. Microprobe analysis (the Co : Cl ratio is 1.0 : 4.7) confirmed the determined composition. Compound is air-sensitive.

For preparation of $\{(K^+)(crypt)\}_3\{(Co^{II}I_2\}_3(HATNA)\}^{3-}\cdot 3C_6H_4Cl_2\cdot 3C_6H_{14}$ (**11**) HATNA (16.0 mg, 0.042 mmol) and three equivalents of $Co^{II}I_2$ (39 mg, 0.126 mmol) were stirred in 17 mL of *o*-dichlorobenzene for 24 h at 60°C yielding dark brown solution. Three equivalents of cryptand[2.2.2] was added (48.0 mg, 0.126 mmol) together with an excess of the reductants potassium graphite (36 mg, 0.2666 mmol). This mixture was stirred for another 24 h at 60°C and the color of the solution turned to deep violet. Solution was cooled down to room temperature and filtered into the tube for the diffusion. Crystals were obtained as black blocks with the 52% yield. Compound **11** was obtained as good quality crystals and its composition was determined by X-ray diffraction analysis on single crystal. All crystals have the same color and shape and several tested crystals have the same unit cell parameters. Microprobe analysis (the Co : Cl : I ratio is 1.0 : 2.1 : 1.9) confirmed the determined composition. Crystals are very air-sensitive.

X-ray Crystallographic study

The diffraction intensity for the structural analyses of the crystals of **1**–**9** was collected on a "Gemini-R" CCD diffractometer with graphite monochromated MoK_α radiation using an Oxford Instrument Cryojet system. Raw data reduction to F^2 was performed using CrysAlisPro, Oxford Diffraction Ltd[4]. The structures were solved using a direct method and refined with the full-matrix least-squares method against F^2 using SHELX-2013[5]. Nonhydrogen atoms were refined in the anisotropic approximation. The positions of H atoms were calculated geometrically. Unit cell parameters were determined for **4**: triclinic, $P\bar{1}$, a = 13.9461(8), b = 14.4043(8), c = 18.3798(10) Å, α = 102.415(3), β = 109.413(3), γ = 95.682(3), V = 3341.4(3) Å^3. These parameters show that complex **4** is isostructural to **2** (Table S1). Unit cell parameters were also determined for **7**: a = 12.86(3), b = 13.65(4), c = 17.53(4) Å, α = 84.34(9), β = 74.65(6), γ = 65.60(10), V = 2704(18) Å^3. Unit cell parameters are close to those in **6** (Table S1) but unit cell volume is smaller nearly by 200 Å^3, since in all cases coordination units with cobalt have shorter Co-N bonds and more compact coordination assemblies. Also according to the elemental analysis **7** in contrast to **6** does not contain solvent *n*-hexane molecules. The crystal structure of **2** contains three positions of solvent $C_6H_4Cl_2$ molecules. In two fully occupied positions solvent molecules are disordered between two orientations with the 0.753(4)/0.247(4) and 0.630(3)/0.370(3) occupancies. One position is occupied with the 0.50 and 0.25 occupancies providing partial content of $C_6H_4Cl_2$ - 2.75 molecules per formula unit. One ethylene group of the {(K$^+$)crypt} cation is disordered between two positions having the 0.809(18)/0.191(18) occupancies. providing partial content of $C_6H_4Cl_2$ - 2.75 molecules per formula unit. One ethylene group of the {(K$^+$)crypt} cation is disordered between two positions having the 0.809(18)/0.191(18) occupancies. The crystal structure of **3** also contains three positions of solvent $C_6H_4Cl_2$ molecules. One solvent is ordered, but in another position solvent molecule is disordered between two orientations with the 0.603(2)/0.393(2) occupancies. One position is only partially occupied by the disordered solvent molecule with the 0.263(2)/0.237(2) occupancies. That provides partial content of $C_6H_4Cl_2$ - 2.50 molecules per formula unit.

Table S1. X-Ray diffraction data for the complexes **1-3**, **5-6**, and **8- 11.**

Compound	**1**	**2**	**3**	**5**	**6**	**8**	**9**	**10**	**11**
Emp. formula	$C_{60}H_{32}Cl_4Co_2I_4N_{12}$	$C_{58.50}H_{59}Cl_{5.50}Co_2I_4KN_8O_6$	$C_{57}H_{58}Cl_9Co_2KN_8O_6$	$C_{60}H_{58}Cl_2Co_2I_4KN_8O_6$	$C_{48}H_{62}Cl_6Fe_3KN_8O_6$*	$C_{78}H_{96}Cl_{10}Fe_2K_2N_{10}O_{12}$	$C_{192}H_{212}Cl_{16}Co_6I_{12}K_4N_{20}O_{24}$	$C_{110}H_{94}Cl_{14}Co_3N_{12}$	$C_{114}H_{174}Cl_6Co_3I_6K_3N_{12}O_{18}$**
M_r [g mol^{-1}]	1688.23	1829.67	1427.12	1722.60	1266.40	1910.04	5783.78	2257.06	3268.83
Color, shape	black prism	black bulk	black bulk	black bulk	black block	black parallelepiped	black plate	black plate	black block
Crystal system	triclinic	triclinic	triclinic	triclinic	triclinic	monoclinic	triclinic	monoclinic	trigonal
Space group	$P\bar{1}$	$P\bar{1}$	$P\bar{1}$	$P\bar{1}$	$P\bar{1}$	$C2/c$	$P\bar{1}$	$P2_1/c$	$P3_1/c$
a, Å	13.8179(5)	14.0660(6)	13.7417(3)	14.1231(3)	14.3774(14)	18.8633(4)	14.1114(4)	13.8315(3)	22.8767(5)
b, Å	14.0043(6)	14.2841(6)	15.0324(7)	14.5435(3)	14.5267(13)	21.2471(3)	26.8675(6)	35.4186(9)	22.8767(5)
c, Å	17.3358(8)	18.4462(8)	16.9381(7)	17.7888(4)	16.4927(13)	23.6207(4)	30.2615(9)	21.2974(8)	14.5786(3)
α, °	108.276(4)	102.279(4)	65.237(4)	69.258(2)	100.170(7)	90	82.183(2)	90	90
β, °	111.226(4)	109.739(4)	85.322(3)	72.192(2)	98.433(7)	112.108(2)	78.925(3)	94.961(3)	90
γ, °	97.419(3)	95.300(3)	87.508(3)	87.191(2)	117.085(9)	90	80.343(2)	90	120
V, Å^3	2855.6(2)	3353.9(3)	3166.4(2)	3246.0(1)	2915.6(5)	8770.9(3)	11036.0(5)	10394.3(5)	6607.5(3)
Z	2	2	2	2	2	4	2	4	2
ρ_{calc} [g cm^{-3}]	1.963	1.812	1.497	1.762	1.443	1.446	1.741	1.442	1.643
μ [mm^{-1}]	2.983	2.670	1.024	2.614	1.134	0.794	2.453	0.888	2.054
$F(000)$	1620	1785	1460	1682	1306	3960	5684	4628	3288
T [K]	150(1)	120(2)	120(2)	110(2)	109.8(4)	100(2)	100(2)	100(1)	104.0(3)
Max. 2Θ, °	29.597	29.563	29.561	28.282	26.8155	28.283	28.282	28.259	29.536
Reflns measured	39997	32536	55448	57650	13214	41619	108568	102836	65826
Unique reflns	13910	15764	15807	15458	9957	10795	51135	24944	11061
Parameters	715	912	810	815	832	514	2801	1217	363
Restraints	0	715	1305	527	1039	0	3779	580	550
Reflns [$F_o > 2(F_o)$]	10176	13852	13167	13571	6171	9722	26742	19809	7363
R_1 [$F_o > 2\sigma(F_o)$]	0.0655	0.0371	0.0397	0.0400	0.1230	0.0285	0.0826	0.0416	0.0630
wR_2 (all data)	0.2565	0.0913	0.1002	0.1140	0.3213	0.0782	0.1904	0.1034	0.1772
G.O.F	1.171	1.028	1.031	1.058	1.060	1.035	1.016	1.026	1.027
CCDC	2370265	2370268	2370269	2370271	2370272	2370274	2370275	2370276	2370278

*additionally complex contains one strongly disordered C_6H_{14} molecule which was SQUEEZED
**additionally complex contains three strongly disordered $C_6H_4Cl_2$ and C_6H_{14} molecules which were SQUEEZED

Crystal structure of **5** contains large cavity which is occupied by strongly disordered solvent $C_6H_4Cl_2$ molecule disordered between five orientations with the 0.25/0.25/0.25/0.125/0.125 occupancies. Totally one $C_6H_4Cl_2$ molecule was found per formula unit. Complex **6** contains one ordered $\{(Fe^{II}Cl_2)_3(HATNA)\}^-$ unit and two halves of crystallographically independent $\{(K^+)(crypt)\}$ cations indicating –1 charge on the coordination units. Besides this a solvent mask was calculated and 113 electrons were found in a volume of 396 Å^3 in one void per unit cell. This is consistent with the presence of one C_6H_{14} molecule per unit cell which account for 100 electrons per unit cell. Complex **8** contains only ordered components. Complex **9** contains four crystallographically independent ordered $\{(K^+)(crypt)\}$ cations and two crystallographically independent ordered $\{(Co^{II}I_2)_3(HATA)\}^{2-}$ anions indicating their dianionic state. There are eight positions of solvent $C_6H_4Cl_2$ molecules per two formula units. The molecules are ordered in two positions and are disordered between two orientations in five positions with the 0.821(7)/0.179(7), 0.758(7)/0.242(7), 0.706(6)/0.294(6), 0.576(6)/0.424(6), 0.671(7)/0.329(7) occupancies. In one position solvent molecule is disordered between three orientations with the 0.343(3)/0.321(3)/0.336(3) occupancies. In the crystal structure of **10** there are four positions of solvent $C_6H_4Cl_2$ molecules per one formula unit. Among them only one molecule is disordered between two orientations with the 0.8923(18)/0.1177(18) occupancies. Complex **11** has high-symmetry trigonal unit cell. In this cell only one third of $\{(Co^{II}I_2\}_3(HATNA)\}^{3-}$ is crystallographically independent. The $\{(K^+)(crypt)\}$cation has full occupancy and is statistically distributed over three orientations with the 0.3333 occupancy. A solvent mask was calculated and 709 electrons were found in a volume of 1827 Å^3 in two voids per unit cell. This is consistent with the presence of 3[$C_6H_4Cl_2$] and 3[C_6H_{14}] molecules per formula unit which account for 744 electrons per unit cell.

To keep a close ideal geometry in the disordered groups, the bond length restraints were applied along with the next-neighbor distances using the SADI SHELXL instruction. The bond length restraints were applied along with the next-neighbor distances using the SADI SHELXL instruction to keep a close ideal geometry in the disordered groups. This resulted in the usage of restraints to refine the crystal structures of **2** (715), **3** (1305), **4** (527), **5** (1039), **7** (3779), **8** (580) and **9** (550).

IR-spectra of the complexes

Table S2. IR-spectra (cm^{-1} in KBr pellets) of starting compounds and salts **1**, **2**, **4**, **6-8** and **11**

	Cryptand	HATNA	solvent	[(CoI$_2$)(HATNA)]^0 ·C$_6$H$_4$Cl$_2$ **1**	{(K$^+$)(crypt)}{(Co^{II}I$_2$)$_2$ (HATNA)}$^{\bullet-}$ 2.75C$_6$H$_4$Cl$_2$ **2**	{(K$^+$)(crypt)}{(Fe^{II}I$_2$)$_2$ (HATNA)}$^-$ ·3C$_6$H$_4$Cl$_2$ **4**	{(K$^+$)(crypt)} {(Fe^{II}Cl$_2$)$_3$ (HATNA)}$^{\bullet-}$ ·C$_6$H$_{14}$ **6**	{(K$^+$)(crypt)} {(Co^{II}Cl$_2$)$_3$ (HATNA)}$^-$ **7**	{(K$^+$)(crypt)}$_2$ {(Fe^{II}Cl$_2$)$_2$ (HATNA)}$^{2-}$· 3C$_6$H$_4$Cl$_2$ **8**	{(K$^+$)(crypt)}$_3$ {(Co^{II}I$_2$}$_3$ (HATNA)}$^{3-}$· 3C$_6$H$_4$Cl$_2^-$· 3C$_6$H$_{14}$ **11**
Cryptand	476w				-	466w*	-	466w*	534w*	514w
	528w				521w	525w*	520w	-	741sh*	755w*
	735m				739w	738w*	-	748w sh	933m	950m
	922m				901m	901w	930w	902m	-	-
	948w				951m	-	-	-	-	-
	982m				980w	-	-	950m	1039sh*	-
	1038w				1038sh	1034w*	1020m*	1031w*	1077s	1078m*
	1071m				1086s	1079sh*	1090s*	1081m*	1103s*	1104s
	1100s				1104s	1099s*	1104s	1102s*	1129s*	1133s*
	1127s				1131s*	1129s*	1132m*	1137s sh*	1207w*	-
	1213w				1216sh*	1219w*	-	1220w*	1302m	1299w
	1295m				1295w*	1299w*	-	1300w*	-	-
	1329m				-	1323w*	-	1325w*	1357m*	1354m*
	1360s				1365s*	1360m*	1360m*	1362s*	1445w*	1435w
	1446m				1455m*	1435w	1452m*	1445w*	1455w*	1465w
	1462m				1472m*	1455m*	1462m	1456w*	1480sh*	1473m
	1490w				-	1498m*	1473m*	1476w	2816w	2816w
	2790w				2814w	2812w	2815w	2817w	2875w*	2875w
	2877w				2883w	2885w*	2872w	2875w*	2963w	2965w
	2943w				2957w	2957w	2960w	2957w		
HATNA		413m		418m	416w	412w*	-	415m*	-	-
		501w		-	-	-	-	-	509w	-
		541w		541w	-	-	-	-	534w*	530w
		606m		610m	616s	606m*	630m	608m*	630m	634m
		757s		759s	761s	759s*	-	757m*	758m*	755w*
		771m		781w	772w	765sh*	-	766m*	789w	797w
		802w		796w	-	790w	801m	780w	808w	818w
		1020w		-	-	1034w	1020m*	1031w	-	1019w
		1078s		1082s	1079m	1085s*	1090s*	1087s*	1085s	1078m*
		1129w		1129s	1131s	1132s*	1132m*	1132s*	1129s*	1133s*
		1236w		1228sh	1231s	1230m*	-	1232s*	1237w	1239w
		1339m		1343m	1347sh	1348m*	-	1355s	-	-
		1364m		1369s	1365s*	1353s*	1360m*	1362s*	1357m*	1354m*
		1475w		1478w	1476sh	1470m*	1473m*	1473m*	1471m	1473m
		1495m		1495m	1500s	1498m*	-	1500m*	-	-
		1521w		1518w	1532w	1536w	-	1534w*	-	-
		1611w		1611w	1610w	1612w*	1610w	1611w*	1632w	1632w
		3056w		3057w	3056w	3057w*	3056w	3060w*	3057w	3059w
C$_6$H$_4$Cl$_2$			657w	658w	657w*		657m		658w	-
			748s	740w	754s*		740w		741sh*	755w*
			1030m	1032w	1034m*		1020m*		1039m*	1030m
			1122m	1129s	1131s*		1132m*		1129s*	-
			1453m	1454m	1455m*		1452m*		1455w*	1465w
C$_6$H$_{14}$			722s				-			-
			758w				740w			755w*
			882m				-			-
			1060m				1090s			1078m
			1342m				-			1354m
			1373s				1360m			-
			1460s				1462m*			1465w*

*****bands coincide, w - weak, m - middle, s – strong, sh- shoulder.

Table S3. IR-spectra (cm^{-1} in KBr pellets) of starting compounds and salts **5**, **9** and **10**.

	CVCl	Cryptand	HATA	$C_6H_4Cl_2$	$\{(K^+)(crypt)\}\{(Co^{II}I_2)_2(HATA)\}^{\bullet-}\cdot C_6H_4Cl_2$ **5**	$\{(K^+)(crypt)\}_2\{(Co^{II}I_2)_3(HATA)\}^{2-}\cdot 4C_6H_4Cl_2$ **9**	$(CV^+)_2\{(Co^{II}Cl_2)_3(HATA)\}^{2-}\cdot 4C_6H_4Cl_2$ **10**
Cat^+	CV^+	Cryptand			Cryptand	Cryptand	CV^+
	420w	476w			471w	468w	420w*
	522w	528w			508w	509w	508w
	561w	735m			743w	737w*	559w
	722m	922m			916w	932w	723w
	744m	948w			951w	950m	744w
	760m	982m			1034w	1031w	760w
	825w	1038w			1081w	1078m	825w
	847w	1071m			1106m	1088m	843w
	913m	1100s			1120w	1123m	912w
	940m	1127s			1234w	-	943w
	1172s	1213w			1299w	1300w	1174m*
	1190m	1295m			1359w	1353m	1188m
	1226w	1329m			1445w	1445w	1228w*
	1296m	1360s			1458w	1458m	1297w*
	1360s	1446m			1476w	1507m	1360s*
	1450w	1462m			2810w	2813w	1477w
	1477w	1490w			2880w	2881w	1524w
	1523w	2790w			2956w	2957w	1584s
	1586s	2877w					2855w
	2856w	2943w					2920*w
	2915w						
HATA			420w		421w	419w	420w*
			468w		457m	460w	-
			493w		-	-	-
			589w		601w	604w	605w
			620w		621w	-	-
			742s		748w	755w	744w*
			840w		840w	832w	835w
			876m		875w	872m	876w
			1076s		1089m	1104s	1063w
			1170w		1171w	1173m	1174m*
			1254w		1248w	1259w	1228w*
			1286w		1290w	1291w	1297w*
			1372w		1384w	1367w	1360s*
			1403s		1412w	1419s	1409w
			1530w		1531w	1512m	1514w
			1550w		1554w	1562w	1563w
			1630m		-	-	-
			2860w		2880w	2881w	2860w
			2921w		2922w	2957w	2925w
$C_6H_4Cl_2$				657w	652w*	-	655w*
				748s	748w*	746w*	753w*
				1030m	1034w*	1031w*	1032w*
				1122m	1120w*	1123m*	1124w*
				1453m	1458w*	1458m*	1458w*

*****bands coincide, w - weak, m - middle, s – strong.

The optical spectra of the obtained complexes were studied in the KBr pellets prepared in anaerobic conditions of the glovebox. The Fourier-transform infrared (FTIR) spectra (400–7800 cm^{-1}) were measured using the KBr pellets with a PerkinElmer Spectrum 400 spectrometer.

The IR spectra of the coordination complexes reproduces the spectra of the starting components with the shift of some bands up to 20 cm^{-1} and the redistribution of the intensity of these bands due to reduction and coordination of metal ions (Figs. S1 and S2, Table S1, S2).

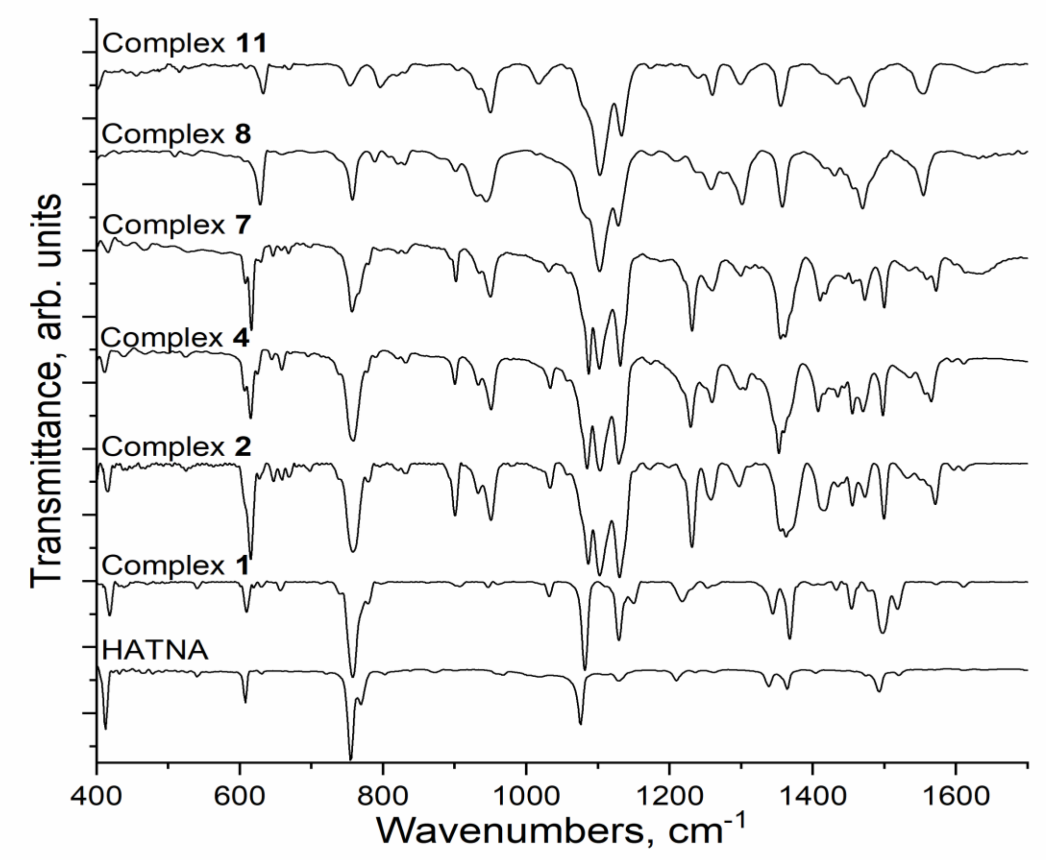

Figure S1. IR-spectrum of starting HATNA and the spectra of $[(CoI_2)(HATNA)]^0 \cdot C_6H_4Cl_2$ (**1**), $\{(K^+)(crypt)\}\{(Co^{II}I_2)_2(HATNA)\}^{\bullet-} \cdot 2.75C_6H_4Cl_2$ (**2**), $\{(K^+)(crypt)\}\{(Fe^{II}I_2)_2(HATNA)\}^{-} \cdot 3C_6H_4Cl_2$ (**4**), $\{(K^+)(crypt)\}\{(Co^{II}Cl_2)_3(HATNA)\}^{-}$ (**7**), $\{(K^+)(crypt)\}_2\{(Fe^{II}Cl_2)_2(HATNA)\}^{2-} \cdot 3C_6H_4Cl_2$ (**8**) and $\{(K^+)(crypt)\}_3\{(Co^{II}I_2\}_3(HATNA)\}^{3-} \cdot 3C_6H_4Cl_2 \cdot 3C_6H_{14}$ (**11**) in KBr pellets. Pellets for **1**, **2**, **4**, **7**, **8** and **11** were prepared in anaerobic conditions.

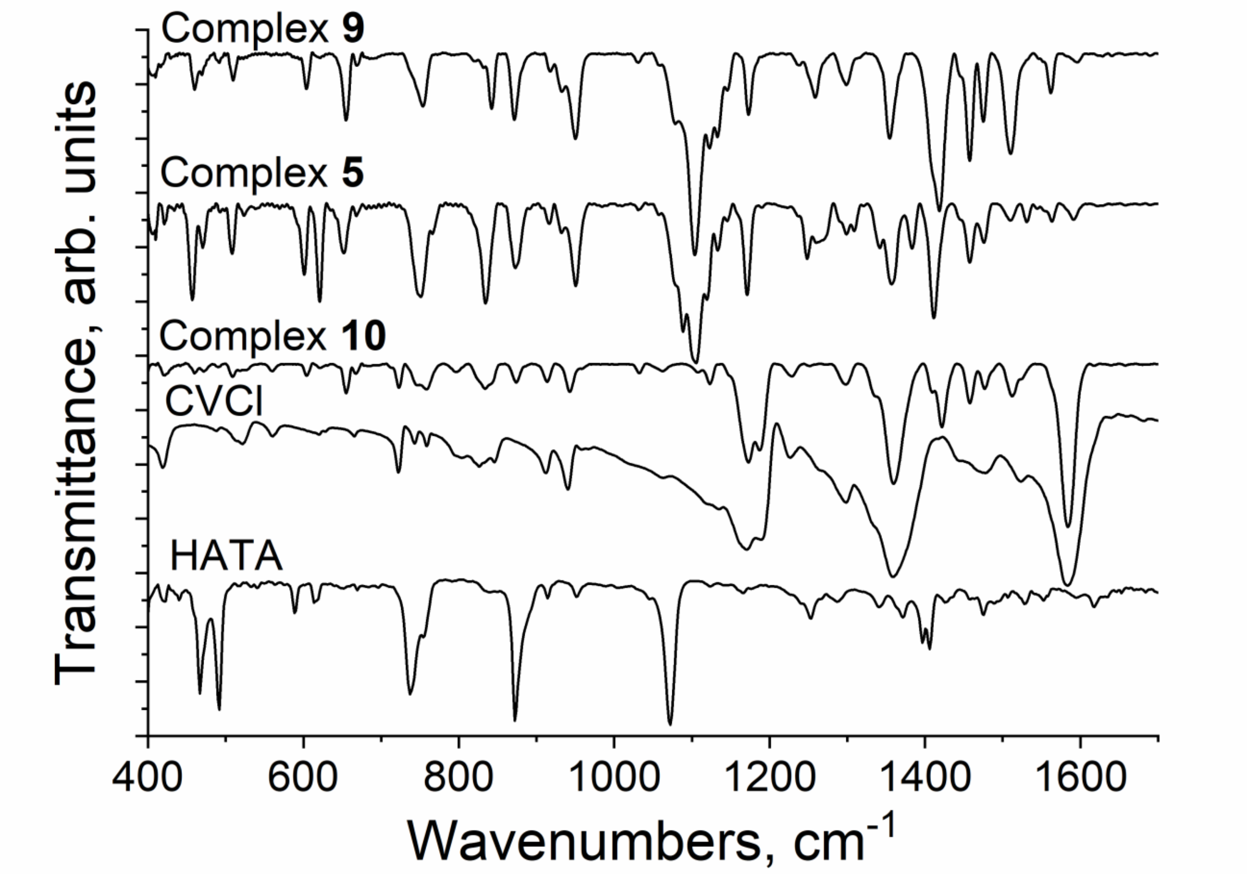

Figure S2. IR-spectrum of starting HATA, CVCl and the spectra of $\{(K^+)(crypt)\}\{(Co^{II}I_2)_2(HATA)\}^{\bullet-}\cdot C_6H_4Cl_2$ (**5**), $\{(K^+)(crypt)\}_2\{(Co^{II}I_2)_3(HATA)\}^{2-}\cdot 4C_6H_4Cl_2$ (**9**) and $(CV^+)_2\{(Co^{II}Cl_2)_3(HATA)\}^{2-}\cdot 4C_6H_4Cl_2$ (**10**) in KBr pellets. Pellets for **5**, **9** and **10** were prepared in anaerobic conditions.

Optical spectra

The UV–visible–NIR spectra were measured using the KBr pellets with a PerkinElmer Lambda 1050 spectrometer in the 250–2500 nm range (Table S4). Starting HATNA has only one resolved band in the spectra at 304 nm (Fig. S3a), whereas HATA having slight red color in the powder form manifest two bands in the UV spectrum at 285 and 364 nm (Fig. S3b). Preparation of neutral coordination $[(\mathrm{Co^{II}I_2})(\mathrm{HATNA})]^0$ assembly in **1** does not noticeably affect the optical spectrum of the ligand. The increase of the negative charge on the ligand provides the shift of the main absorption band of HATNA to smaller energies from 304 (neutral HATNA) to 370 nm (for trianion in **11**). Besides, new transitions appear for the anionic complexes due to the population of the ligand LUMO providing broad signals in the NIR range (980-1070 nm for the monoanions **2**, **3** and trianion **11**; 840 and 1160 nm for the dianion **9**). The complexes with HATA have similar features in the spectra of coordinated anions showing broad band at 1000 nm in the spectrum of coordinated monoanion in **5** and double bands at 920 and 1030-1040 nm for the dianions **9** and **10**. Complex **10** additionally contains an intense band at 594 nm in the spectrum, which is attributed to the $\mathrm{CV^+}$ cations. This cation generally has very intense absorption in the visible range with a maximum nearly at the same position.

Table S4. Optical spectra for the starting compounds and obtained complexes (excepting **3**).

N	Composition	Absorption bands, nm
	HATNA	304, 390 (shoulder)
	HATA	285, 364
1	$(\mathrm{CoI_2})(\mathrm{HATNA})]^0$	304, 347, 400 (shoulder), 700 weak
2	$\{(\mathrm{Co^{II}I_2})_2(\mathrm{HATNA})\}^-$	330, 505 (shoulder), 970, 1150 (broad)
4	$\{(\mathrm{Fe^{II}I_2})_2(\mathrm{HATNA})\}^-$	311, 350 split, 1045, 1160 (broad)
5	$\{(\mathrm{Co^{II}I_2})_2(\mathrm{HATA})\}^-$	284 (shoulder), 371, 1060 (broad)
6	$\{(\mathrm{Fe^{II}Cl_2})_3(\mathrm{HATNA})\}^-$	320, 1070 (broad)
7	$\{(\mathrm{Co^{II}Cl_2})_3(\mathrm{HATNA})\}^-$	320, 680, 1075 (broad)
8	$\{(\mathrm{Fe^{II}Cl_2})_2(\mathrm{HATNA})\}^{2-}$	378, 840, 1164, 1600 (CT band, broad)
9	$\{(\mathrm{Co^{II}I_2})_3(\mathrm{HATA})\}^{2-}$	296, 406, 542, 925, 1034
	CVCl	310, 595
10	$\{(\mathrm{Co^{II}Cl_2})_3(\mathrm{HATA})\}^{2-}$	305, 414, 594 (CV), 928, 1042
11	$\{(\mathrm{Co^{II}I_2}\}_3(\mathrm{HATNA})\}^{3-}$	370, 640, 1070 (broad)

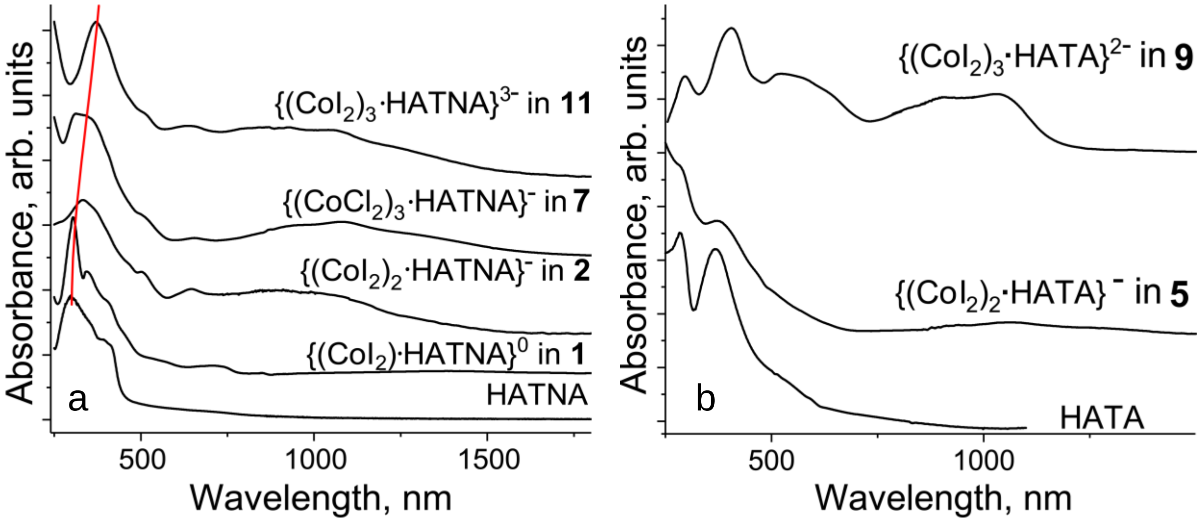

Figure S3. Spectra of starting ligands HATNA and HATA and the complexes in KBr pellets prepared in anaerobic conditions: (a) **1**, **2**, **7** and **11**; (b) **5** and **9**.

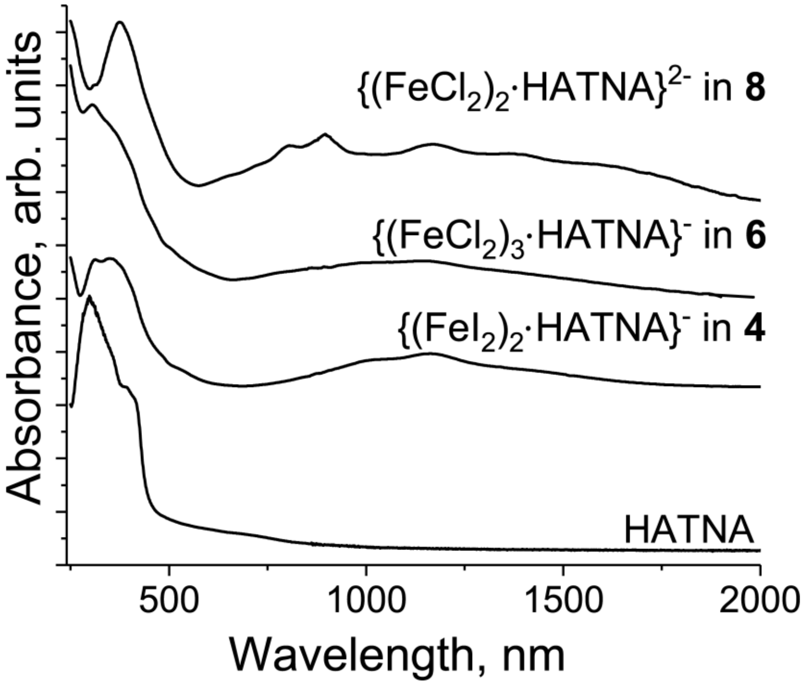

Figure S4. Spectra of starting ligand HATNA and the complexes in KBr pellets prepared in anaerobic conditions: $\{(K^+)(crypt)\}\{(Fe^{II}I_2)_2(HATNA)\}^{-}\cdot 3C_6H_4Cl_2$ (**4**); $\{(K^+)(crypt)\}\{(Fe^{II}Cl_2)_3(HATNA)\}^{-}\cdot C_6H_{14}$ (**6**), $\{(K^+)(crypt)\}_2\{(Fe^{II}Cl_2)_2(HATNA)\}^{2-}\cdot 3C_6H_4Cl_2$ (**8**).

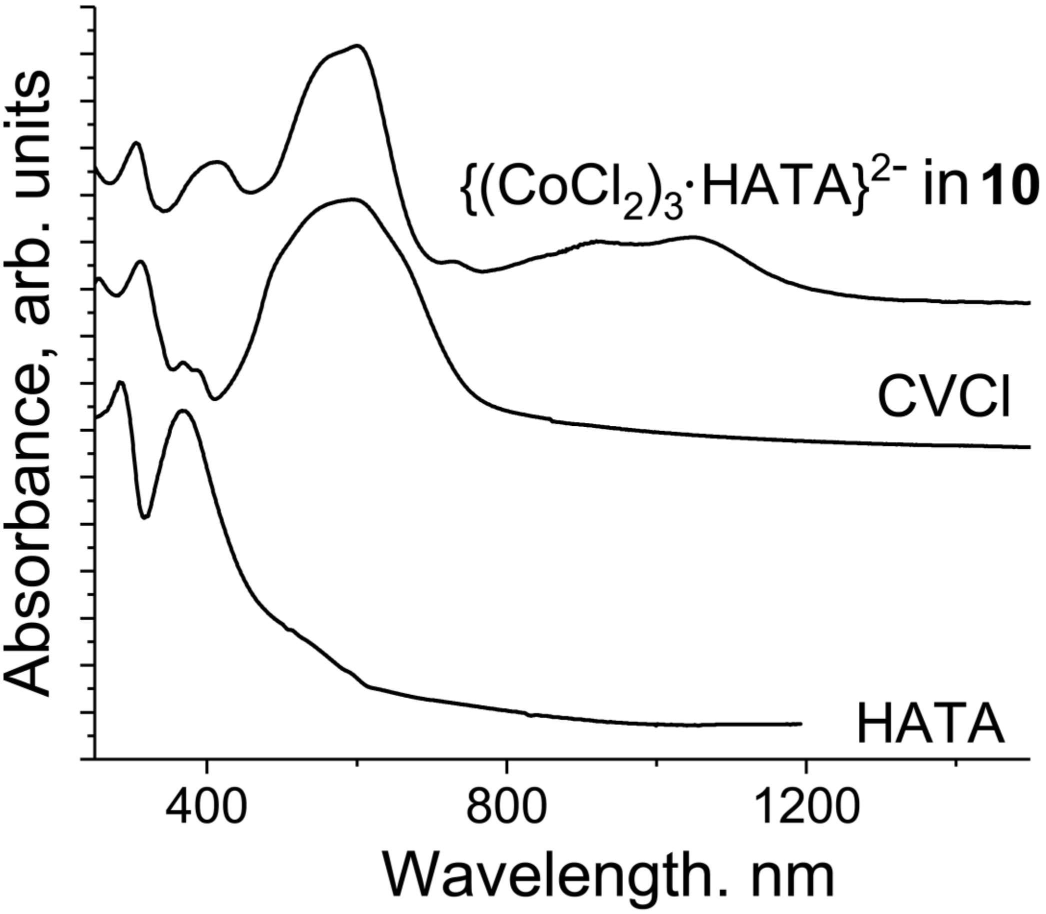

Figure S5. Spectra of starting ligand HATA and CVCl and the complex in KBr pellet prepared in anaerobic conditions: $\{(CV^+)_2\}\{(Co^{II}Cl_2)_3(HATA)\}^{2-}\cdot 4C_6H_4Cl_2$ **(10).**

Crystal structures

The labeling color for each atomic species is same to that in main text.

Complex **1**.

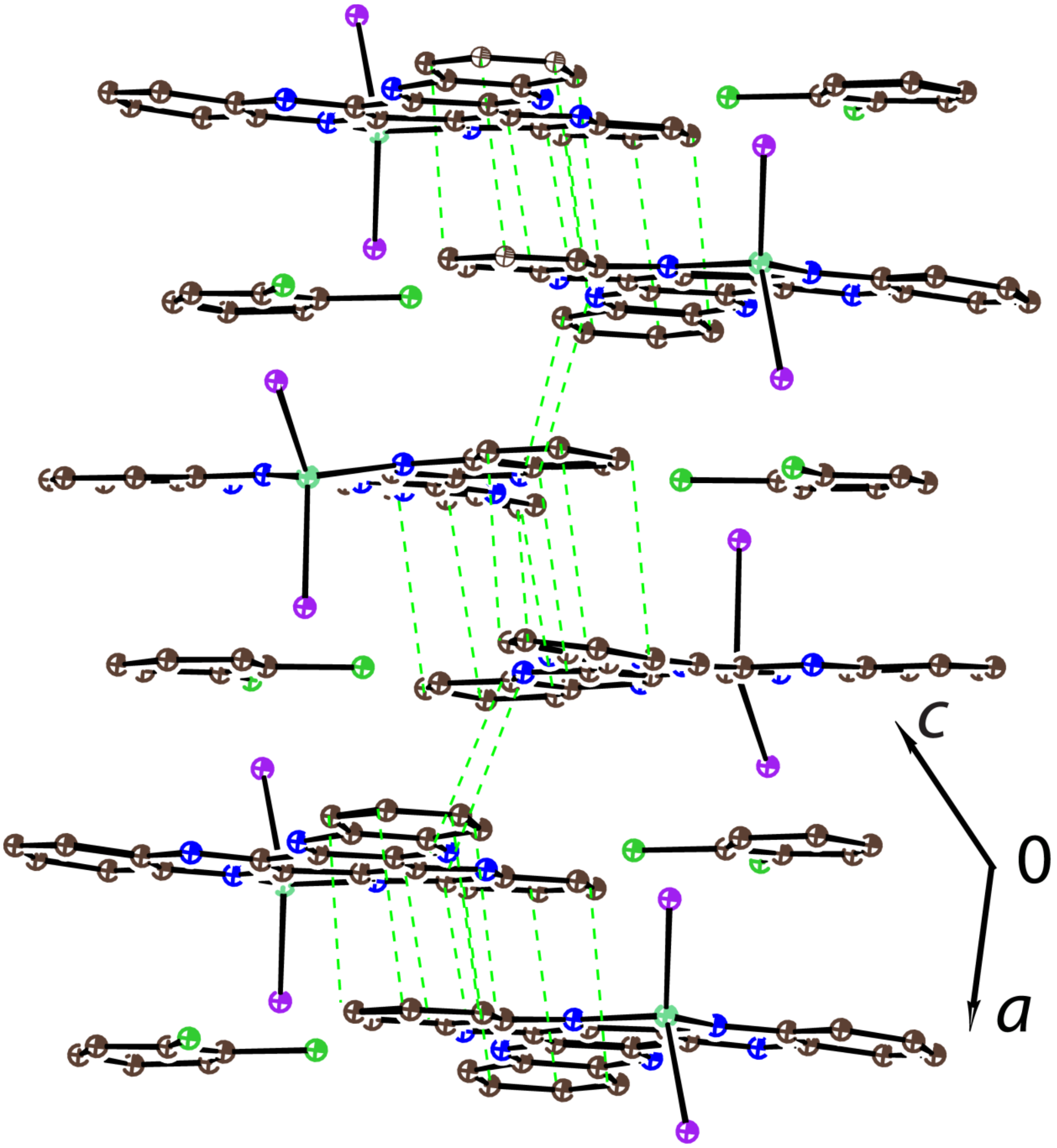

Figure S6. View on the dimerized stacks in complex $[(\mathrm{Co^{II}I_2})(\mathrm{HATNA})]^0\cdot \mathrm{C_6H_4Cl_2}$ (**1**). Van der Waals contacts are shown by green dashed lines. Ortep[6] drawing with equivalent isotropic atomic displacement parameters is shown.

Complex **2.**

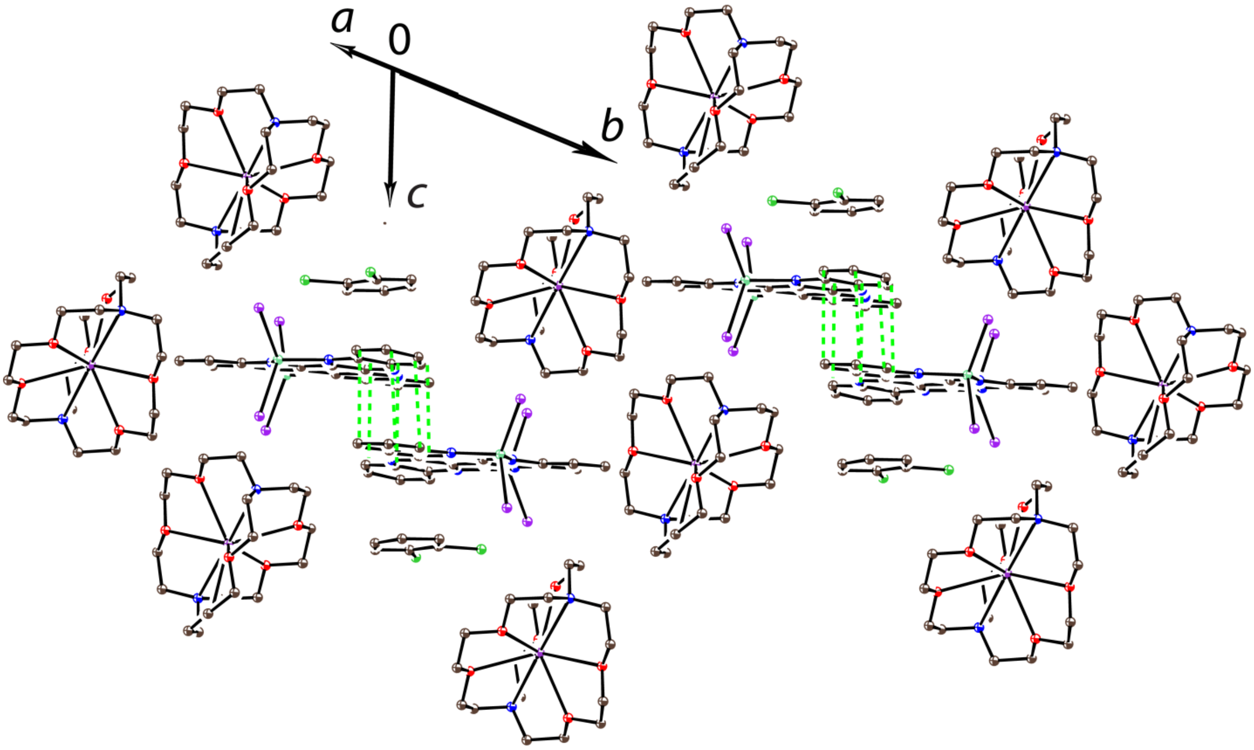

Figure S7. View on the dimers from the $\{(Co^{II}I_2)_2(HATNA)\}^-$ anions and isolated by the $\{(K^+)(crypt)\}$cations and solvent $C_6H_4Cl_2$ molecules in $\{(K^+)(crypt)\}\{(Co^{II}I_2)_2(HATNA)\}^- \cdot 2.75C_6H_4Cl_2$ (**2**). Van der Waals contacts are shown by green dashed lines. Ortep[6] drawing with equivalent isotropic atomic displacement parameters is shown.

Complex **3.**

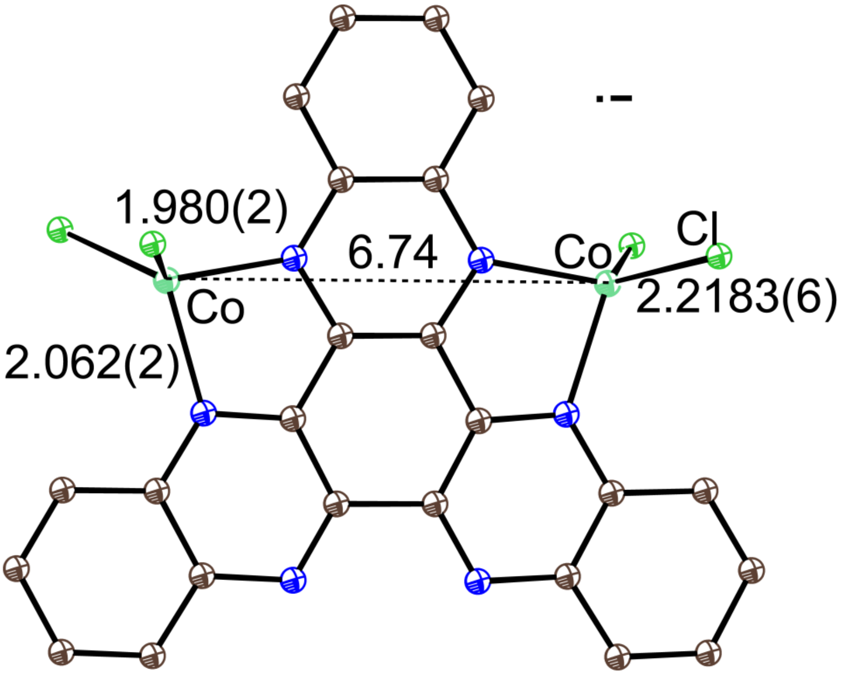

Figure S8. Molecular structure of $\{(Co^{II}Cl_2)_2(HATNA)\}^-$ in **3**. Charge of the units and average bond length are shown. Carbon is shown by brown, nitrogen by blue, cobalt by aquamarine and chloride by lime green colors. Ortep[6] drawing with equivalent isotropic atomic displacement parameters is shown.

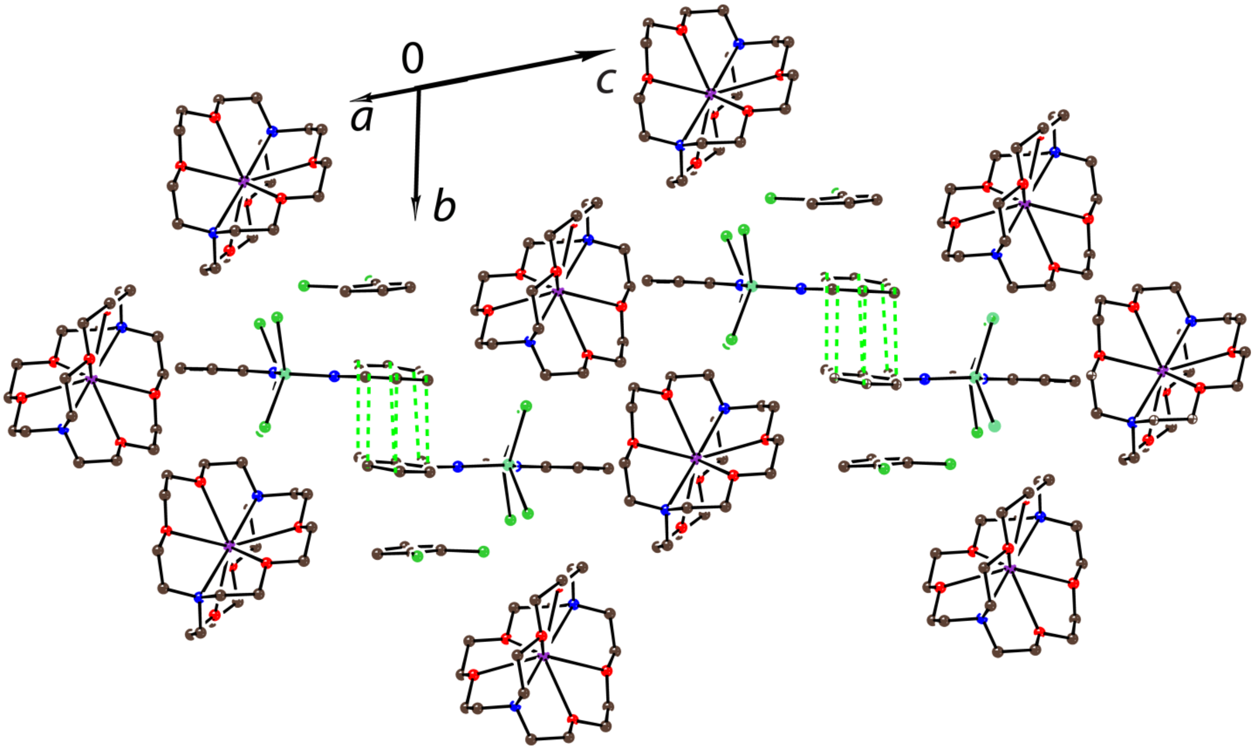

Figure S9. View on the dimers from the $\{(Co^{II}Cl_2)_2(HATNA)\}^-$ anions and isolated by the $\{(K^+)(crypt)\}$ cations and solvent $C_6H_4Cl_2$ molecules in $\{(K^+)(crypt)\}\{(Co^{II}Cl_2)_2(HATNA)\}^-\cdot 2.5C_6H_4Cl_2$ (**3**). Van der Waals contacts are shown by green dashed lines. Ortep[6] drawing with equivalent isotropic atomic displacement parameters is shown.

Complex **8**.

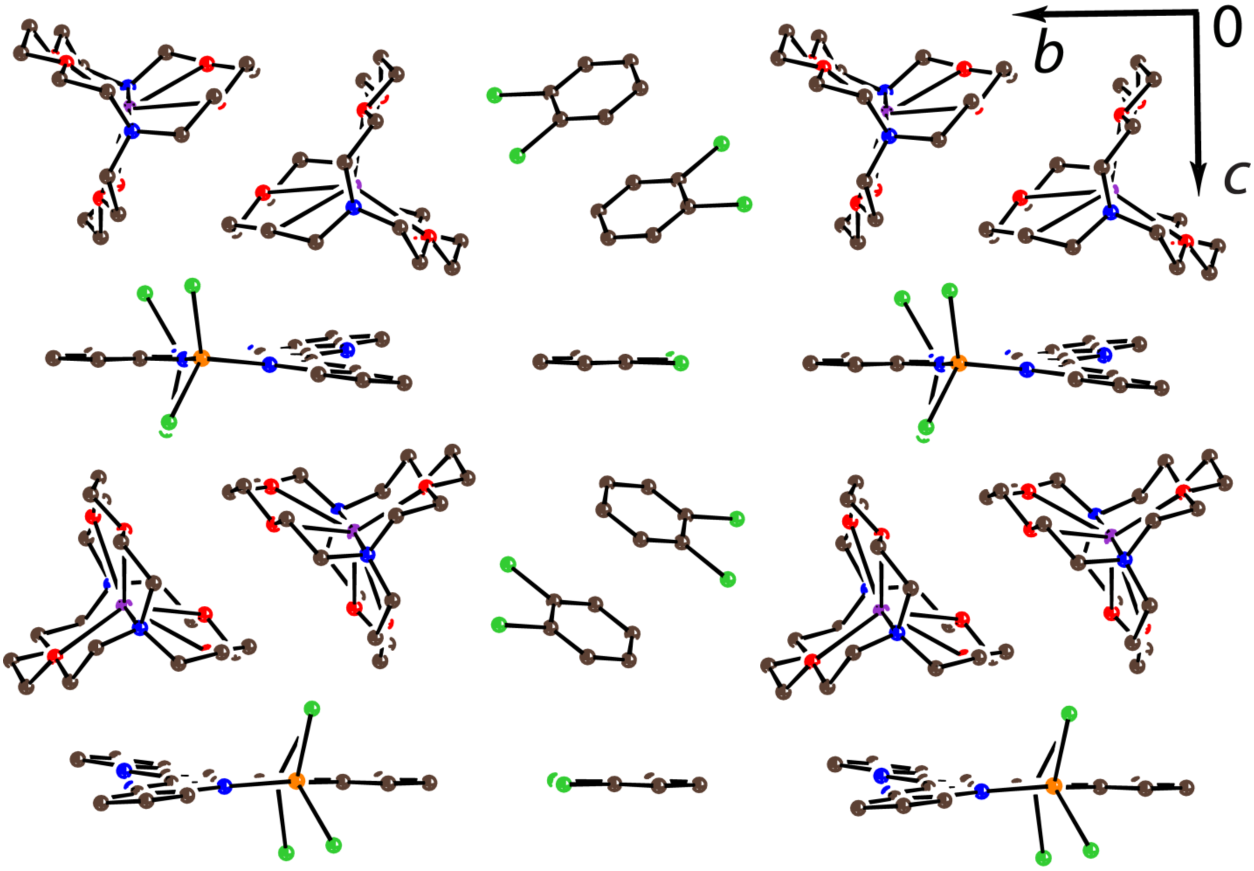

Figure S10. View on the packing of the $\{(Fe^{II}Cl_2)_2(HATNA)\}^{2-}$ dianions isolated by the $\{(K^+)(crypt)\}$ cations and solvent $C_6H_4Cl_2$ molecules in $\{(K^+)(crypt)\}_2\{(Fe^{II}Cl_2)_2(HATNA)\}^{2-}\cdot 3C_6H_4Cl_2$ in complex **8**. Ortep[6] drawing with equivalent isotropic atomic displacement parameters is shown.

Complex **10**.

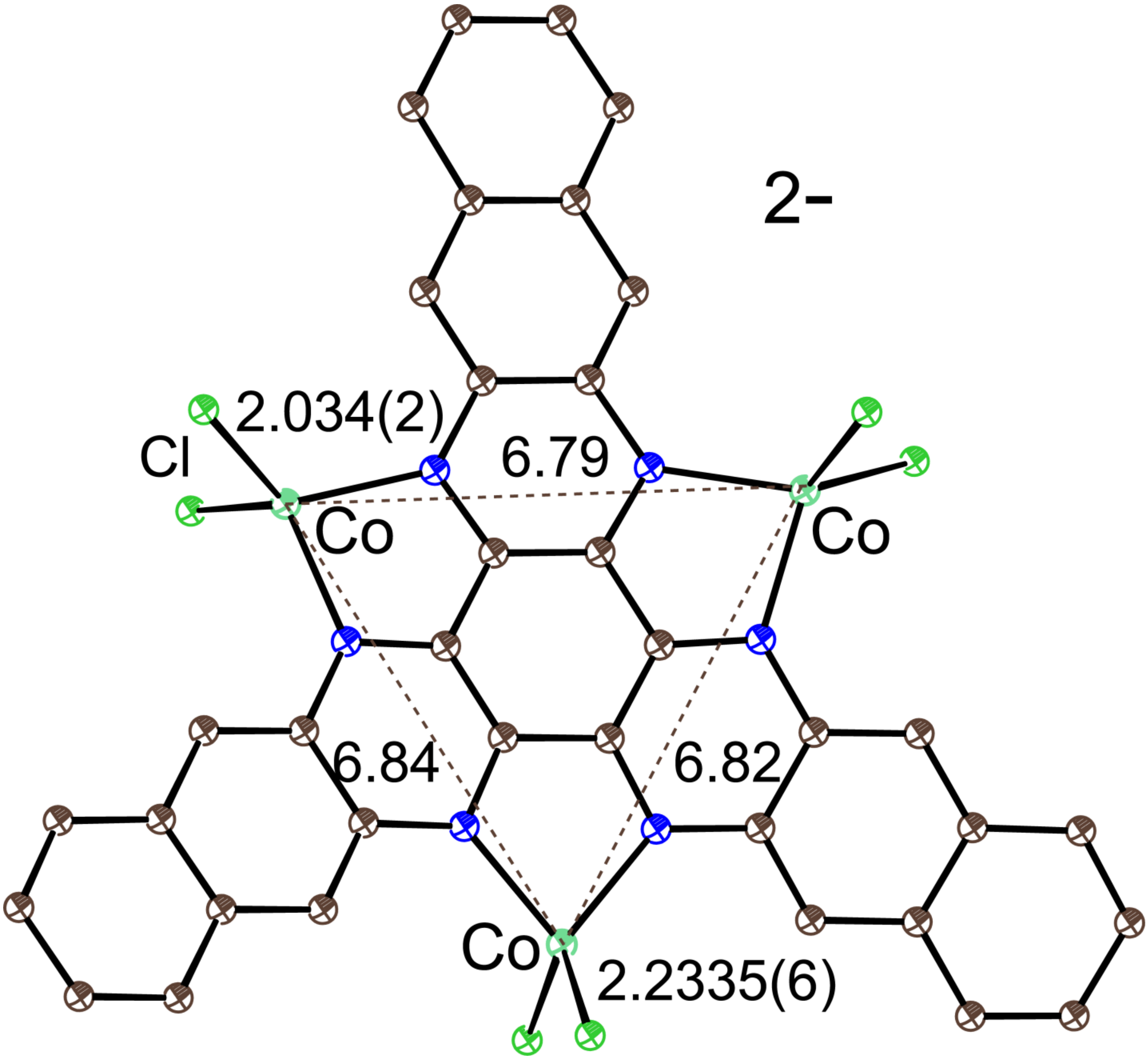

Figure S11. Molecular structure of the $\{(Co^{II}Cl_2)_3(HATA)\}^{2-}$ dianions in $(CV^+)_2\{(Co^{II}Cl_2)_3(HATA)\}^{2-}\cdot 4C_6H_4Cl_2$ in **10**. Charge of the units and average bond length are shown. Carbon is shown by brown, nitrogen by blue, cobalt by aquamarine and chloride by lime green colors. Ortep[6] drawing with equivalent isotropic atomic displacement parameters is shown.

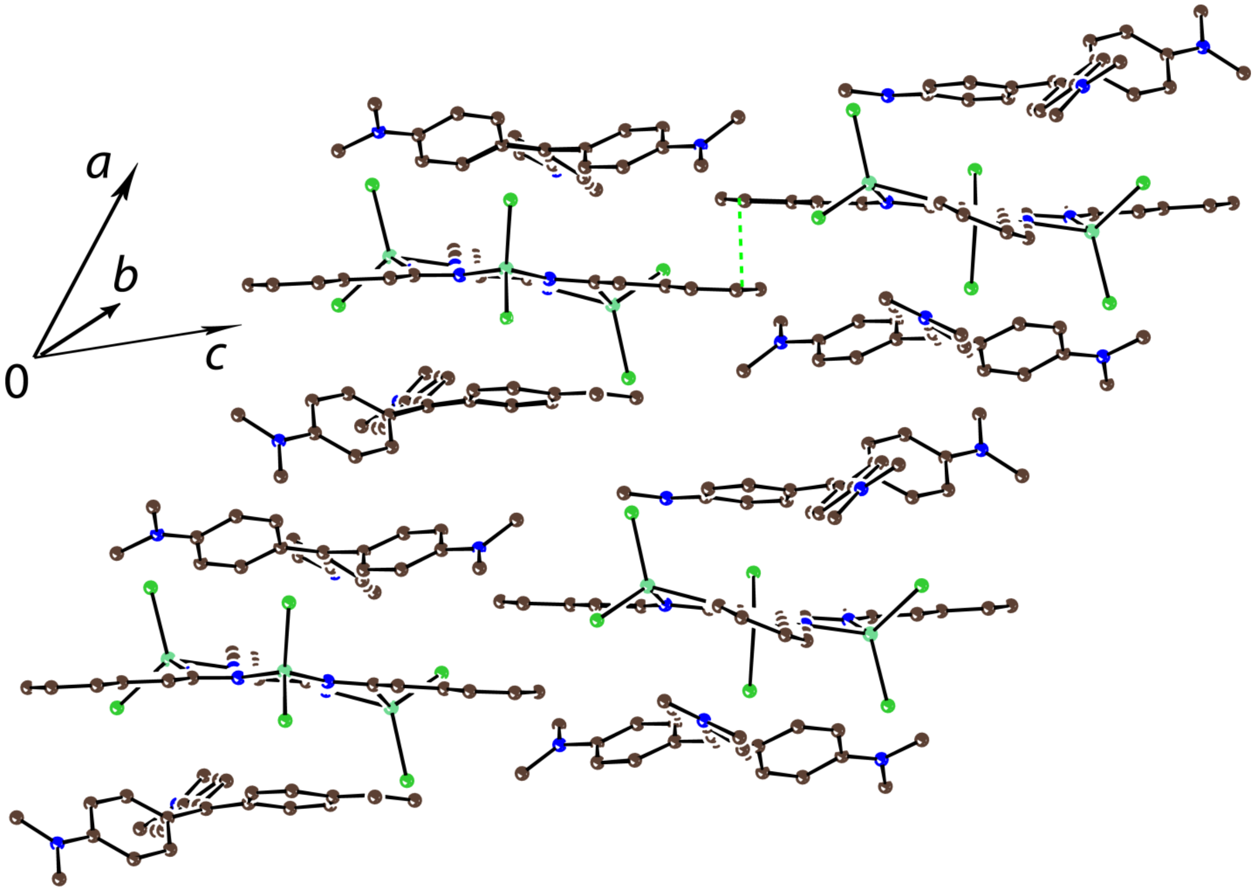

Figure S12. View on the packing of the $\{(\mathrm{Co^{II}Cl_2})_3(\mathrm{HATA})\}^{2-}$ dianions isolated by the $\mathrm{CV^+}$ cations in the stacks of $(\mathrm{CV^+})_2\{(\mathrm{Co^{II}Cl_2})_3(\mathrm{HATA})\}^{2-}\cdot 4\mathrm{C_6H_4Cl_2}$ (**10**). Van der Waals contacts are shown by green dashed lines. Ortep[6] drawing with equivalent isotropic atomic displacement parameters is shown.

Complex **11**.

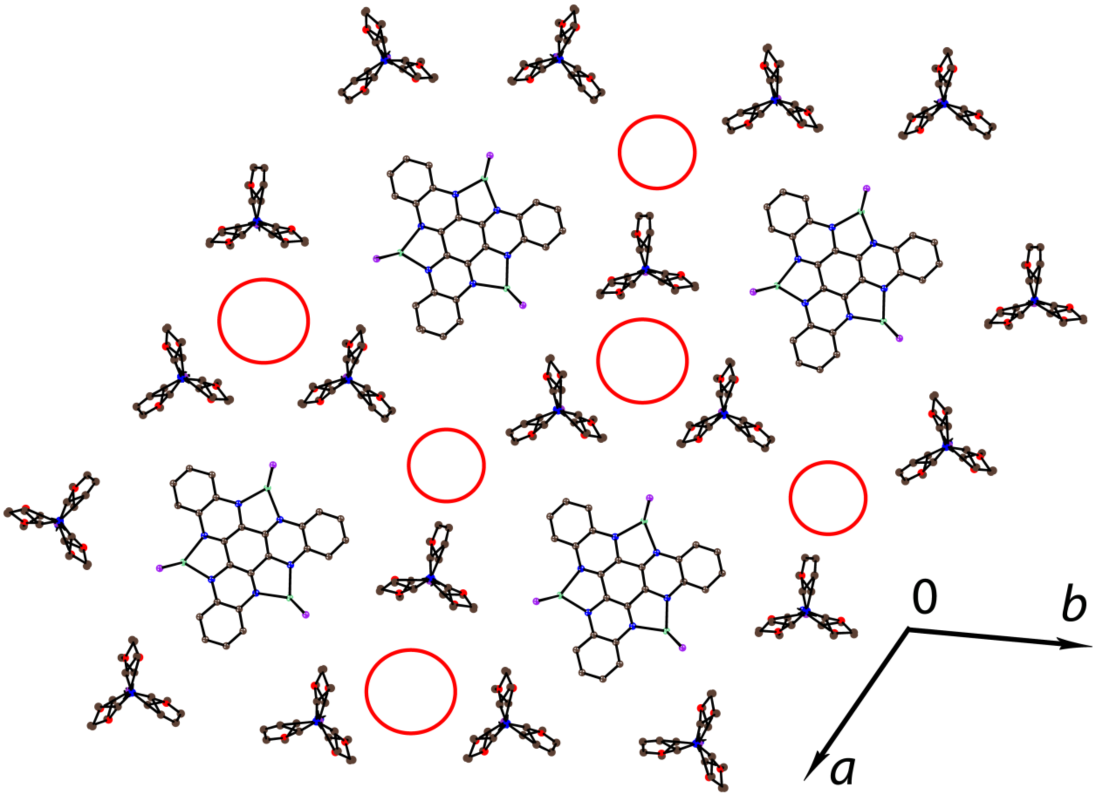

Figure S13. View on the layers composed of the{$(Co^{II}I_2)_3$(HATNA)}$^{3-}$ trianions and surrounded by three {(K^+)(crypt)} cations in {(K^+)(crypt)}$_3${$(Co^{II}I_2)_3$(HATNA)}$^{3-}$$\cdot 3C_6H_4Cl_2$ $\cdot 3C_6H_{14}$ (**11**). Rotationally disordered cations are shown only in one orientation with 0.33 occupancy. Large and small red circles show positions of strongly disordered solvent $C_6H_4Cl_2$ molecules. Ortep[6] drawing with equivalent isotropic atomic displacement parameters is shown.

Spin Hamiltonians for the fitting of magnetic data by PHI

Spin Hamiltonian $\hat{H}$ for complex **1**:

$$\hat{H}_1 = D\cdot\left(\hat{S}_z^2 - \frac{1}{3}\cdot\vec{\hat{S}}^2\right) + \mu_B(g_x H_x \hat{S}_x + g_y H_y \hat{S}_y + g_z H_z \hat{S}_z)$$

where $\vec{\hat{S}}$ denotes the Co^{II} spins, *D* is the axial Co^{II} ZFS, g is the Co^{II} g-factor.

Spin Hamiltonians $\hat{H}$ for complexes **2**, **4** and **6-11**:

$$\hat{H}_2 = -2J\cdot(\vec{\hat{S}_1}\,\overrightarrow{\hat{S}_{HAT}} + \vec{\hat{S}_2}\,\overrightarrow{\hat{S}_{HAT}}) + D\cdot\sum_{i=1}^{2}(\hat{S}_{zi}^2 - \frac{1}{3}\cdot\vec{\hat{S}_i}^2) + \mu_B(g_{Co}(\hat{S}_1+\hat{S}_2) + g_{HAT}\overrightarrow{\hat{S}_{HAT}})\cdot\vec{H}$$

(here J is metal-radical exchange coupling)

$$\hat{H}_4 = \hat{H}_2 \text{ but with Fe}^{II}\text{ spins}$$

$$\hat{H}_6 = -2J_1\cdot\sum_{i=1}^{3}\vec{\hat{S}_i}\cdot\overrightarrow{\hat{S}_{HAT}} - 2J_2\cdot\sum_{i\neq j}^{i,j\in\{1,2,3\}}\vec{\hat{S}_i}\cdot\vec{\hat{S}_j} + D\cdot\sum_{i=1}^{3}(\hat{S}_{zi}^2 - \frac{1}{3}\cdot\vec{\hat{S}_i}^2) + \mu_B(g_{Fe}\sum_{i=1}^{3}\vec{\hat{S}_i} + g_{HAT}\overrightarrow{\hat{S}_{HAT}})\cdot\vec{H}$$

$$\hat{H}_7 = \hat{H}_6 \text{ but with Co}^{II}\text{ spins}$$

$$\hat{H}_8 = -2J\cdot\vec{\hat{S}_1}\,\vec{\hat{S}_2} + D\cdot\sum_{i=1}^{2}(\hat{S}_{zi}^2 - \frac{1}{3}\cdot\vec{\hat{S}_i}^2) + \mu_B g_{Fe}(\hat{S}_1+\hat{S}_2)\cdot\vec{H}$$

(here J is Fe^{II}–Fe^{II} exchange coupling)

$$\hat{H}_9 = -2J\cdot\sum_{i\neq j}^{i,j\in\{1,2,3\}}\vec{\hat{S}_i}\cdot\vec{\hat{S}_j} + D\cdot\sum_{i=1}^{3}(\hat{S}_{zi}^2 - \frac{1}{3}\cdot\vec{\hat{S}_i}^2) + \mu_B g_{Co}\sum_{i=1}^{3}\vec{\hat{S}_i}\cdot\vec{H}$$

$$\hat{H}_{10} = \hat{H}_9$$

$$\hat{H}_{11} = -2J_1\cdot\sum_{i=1}^{3}\vec{\hat{S}_i}\cdot\overrightarrow{\hat{S}_{HAT}} - 2J_2\cdot\sum_{i\neq j}^{i,j\in\{1,2,3\}}\vec{\hat{S}_i}\cdot\vec{\hat{S}_j} + D\cdot\sum_{i=1}^{3}(\hat{S}_{zi}^2 - \frac{1}{3}\cdot\vec{\hat{S}_i}^2) + \mu_B(g_{Co}\sum_{i=1}^{3}\vec{\hat{S}_i} + g_{HAT}\overrightarrow{\hat{S}_{HAT}})\cdot\vec{H}$$

where $\vec{\hat{S}_1}$, $\vec{\hat{S}_2}$, and $\vec{\hat{S}_3}$ denote the Co^{II} or Fe^{II} spins, $\overrightarrow{\hat{S}_{HAT}}$ denotes the HAT-ligand spin, J_1 denotes the Co^{II}–HAT or Fe^{II}–HAT, J_2 denotes Co^{II}–Co^{II} or Fe^{II}–Fe^{II} exchange values, respectively, g_{Co} is the Co^{II} g-factor, g_{Fe} is the Fe^{II} *g*-factor and g_{HAT} is the HAT-ligand g-factor (fixed at 2.0) and $\vec{H}$ is the magnetic field.

The experimental data for complex **5** and additionally complexes **2** and **4** were approximated considering them as the coupled spin systems with total spins *S* = 5/2 (for **2** and **5**) and 7/2 (for **4**). The following general Hamiltonian was used:

$$\hat{H} = D\cdot(\hat{S}_z^2 - \frac{1}{3}\cdot\vec{\hat{S}}^2) + \mu_B g\vec{\hat{S}}\cdot\vec{H}$$

Magnetic data.

Complex **1**.

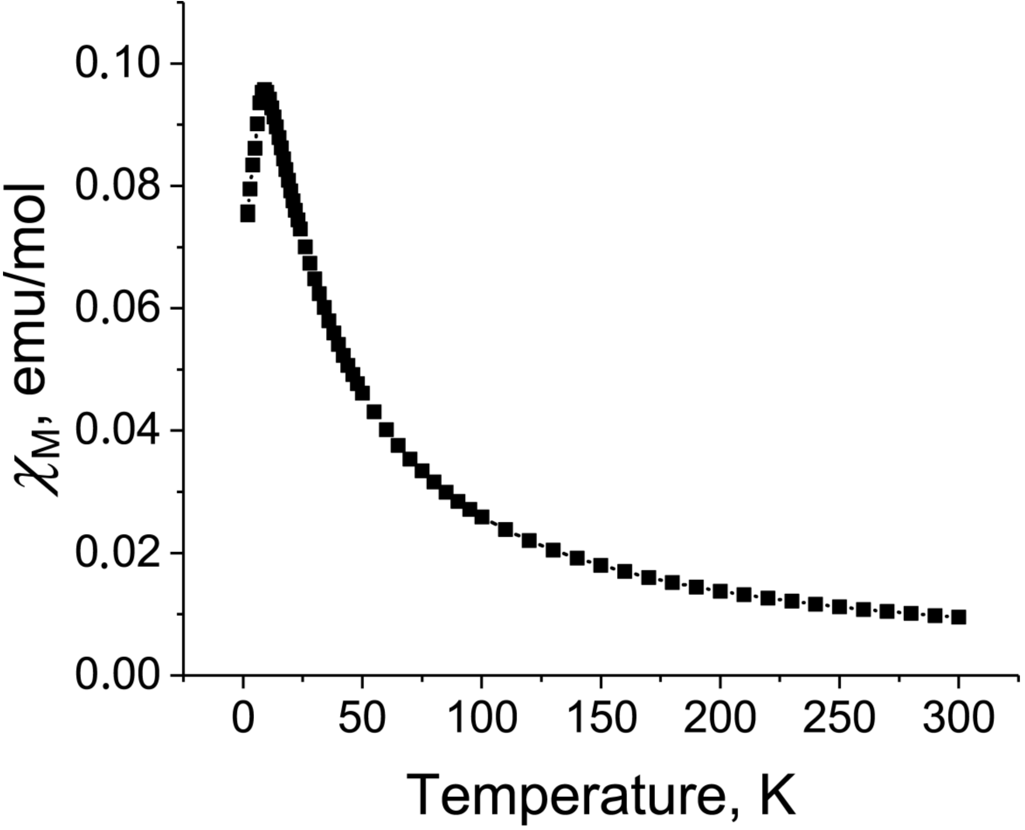

Figure S14. Temperature dependence for molar magnetic susceptibility of polycrystalline $[(Co^{II}I_2)(HATNA)]^0 \cdot C_6H_4Cl_2$ (**1**) in the 1.9-300 K range after the subtraction of temperature independent contribution and contribution from the Curie impurities (less than 5% of *S* = 1/2 spins per formula unit).

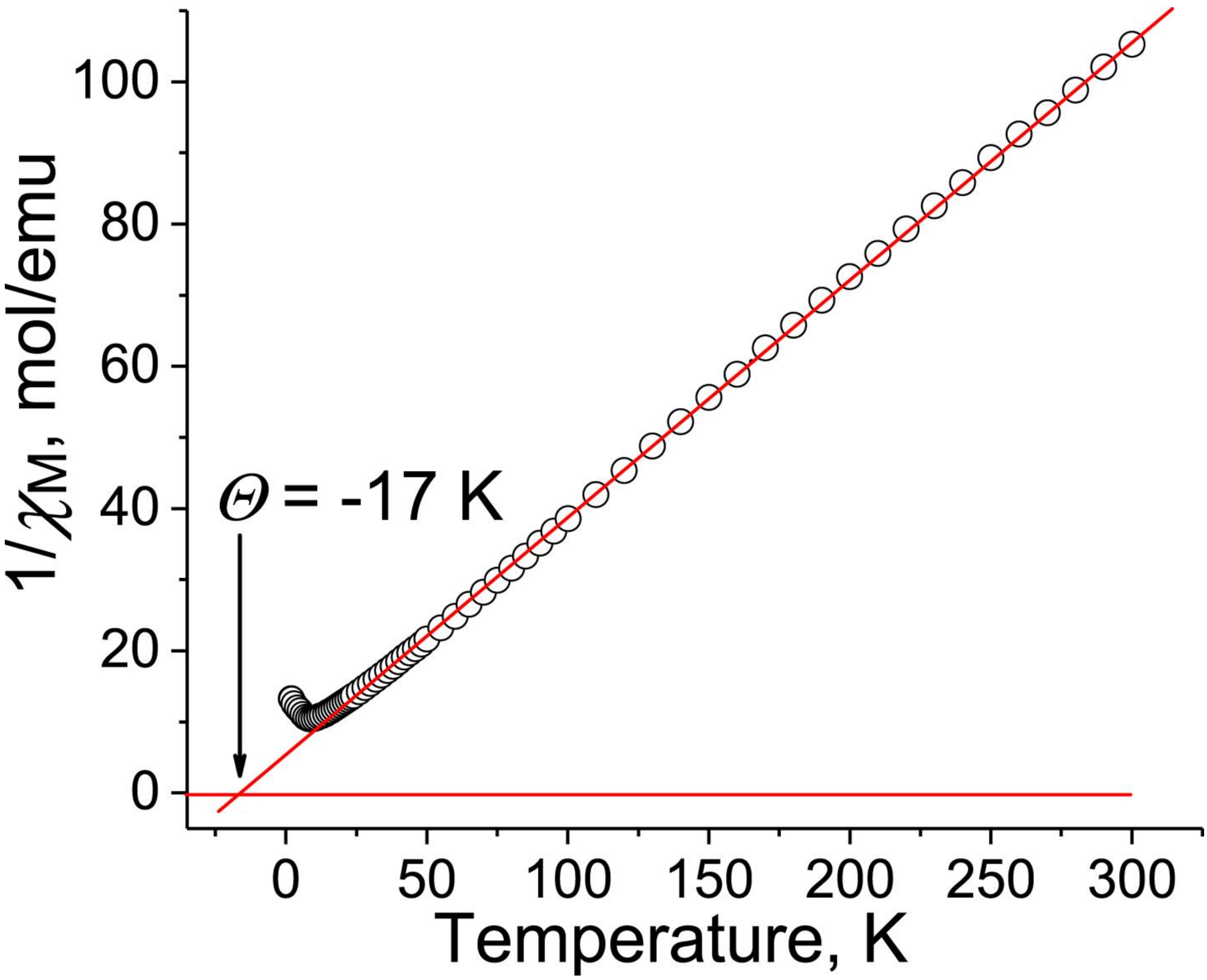

Figure S15. Temperature dependence of reciprocal molar magnetic susceptibility and approximation of the data by the Curie-Weiss law with Weiss temperature (*Θ*) of -17 K for polycrystalline **1** in the 1.9-300 K range.

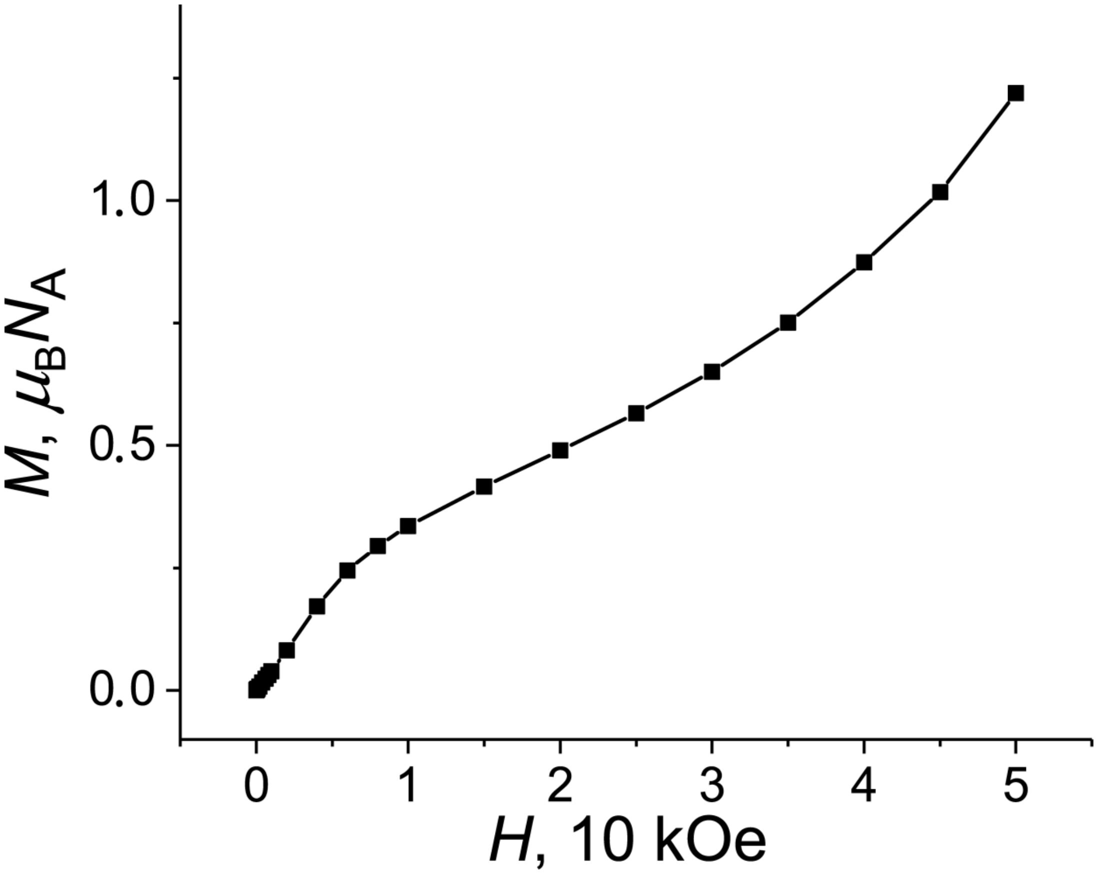

Figure S16. Dependence of magnetization of polycrystalline **1** *vs* magnetic field up to 50 kOe at 2 K (black line is a guide to the eye).

Complex **2**.

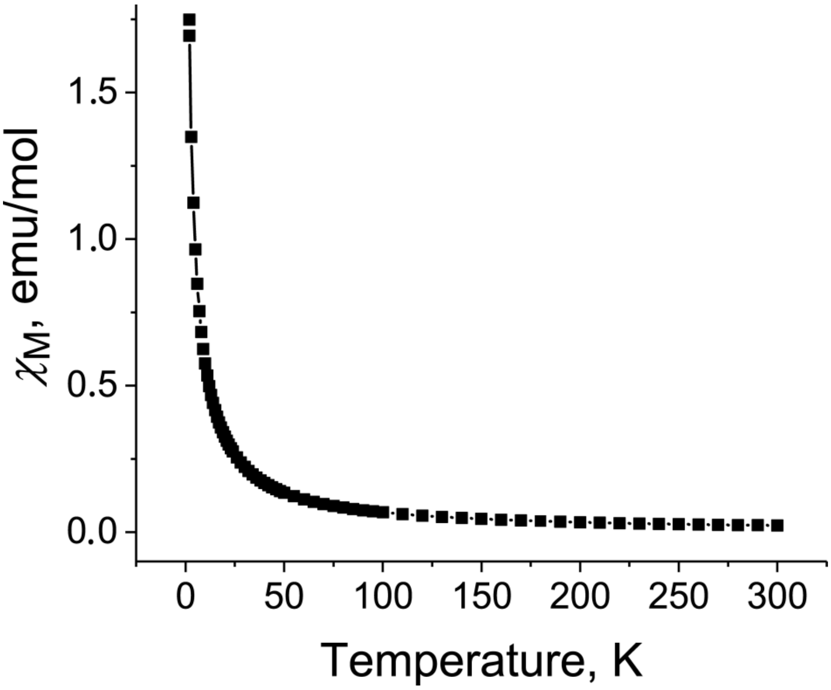

Figure S17. Temperature dependence for molar magnetic susceptibility of polycrystalline $\{(K^+)(crypt)\}\{(Co^{II}I_2)_2(HATNA)\}^-\cdot 2.75C_6H_4Cl_2$ (**2**) in the 1.9-300 K range after the subtraction of temperature independent contribution.

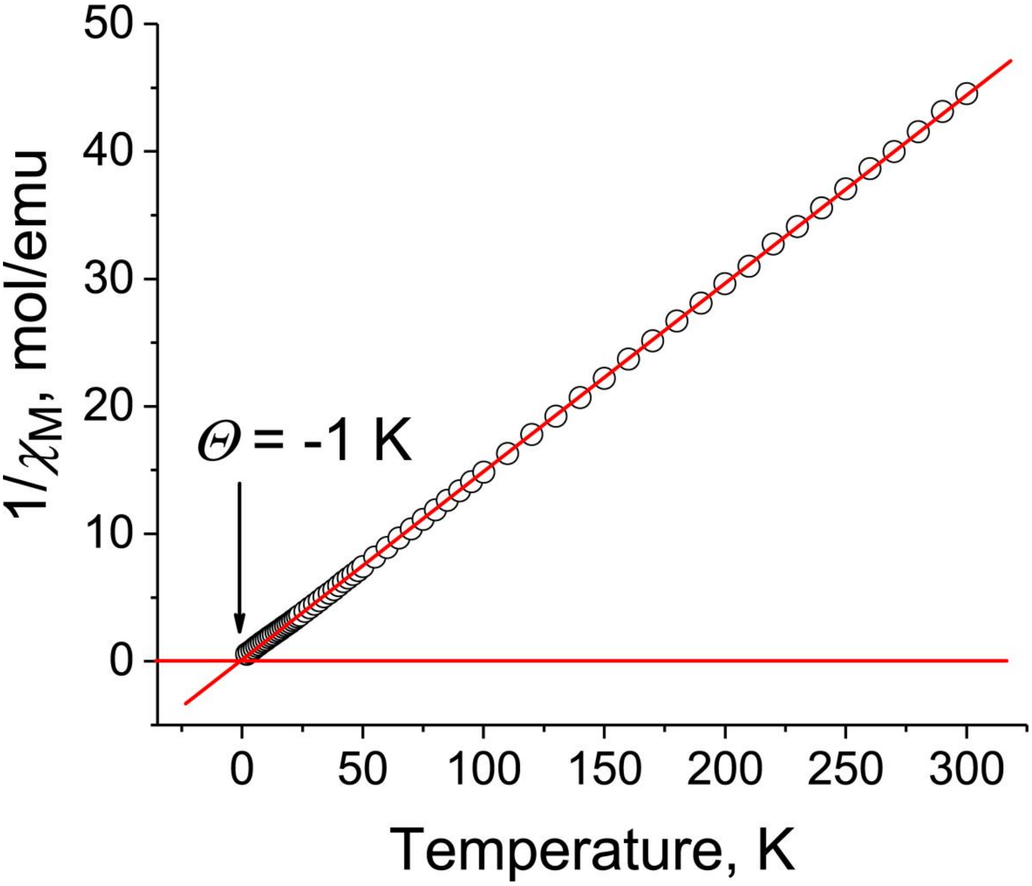

Figure S18. Temperature dependence of reciprocal molar magnetic susceptibility and approximation of the data by the Curie-Weiss law with Weiss temperature (Θ) of -1 K for polycrystalline **2** in the 1.9-300 K range.

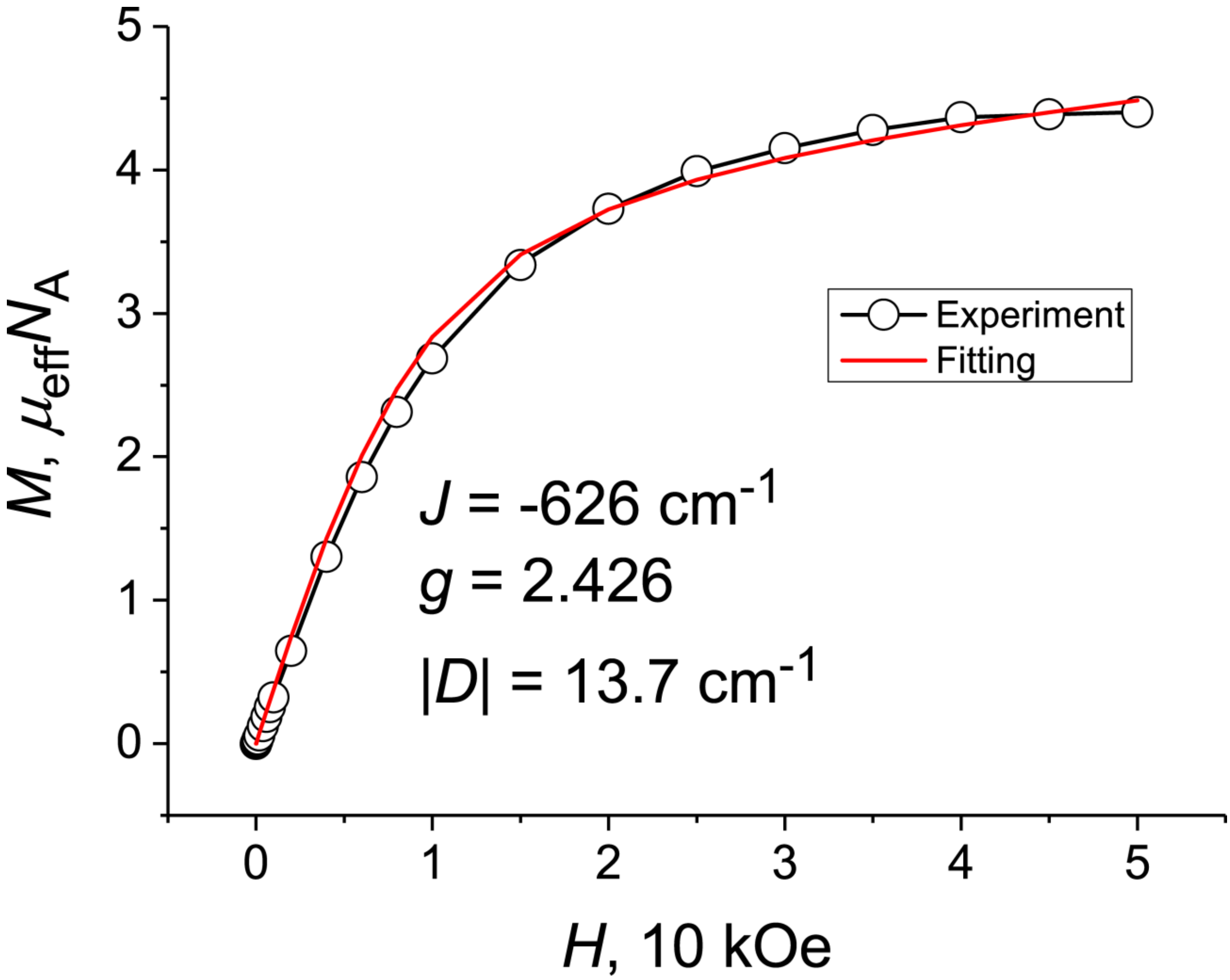

Figure S19. Dependence of magnetization of polycrystalline **2** *vs.* magnetic field (open circles) up to 50 kOe magnetic field at 2 K and fitting of the data by PHI[7] (red curve) with the same parameters as was used for the fitting of temperature dependence of the $\chi_M T$ values (Fig. 6a in the manuscript).

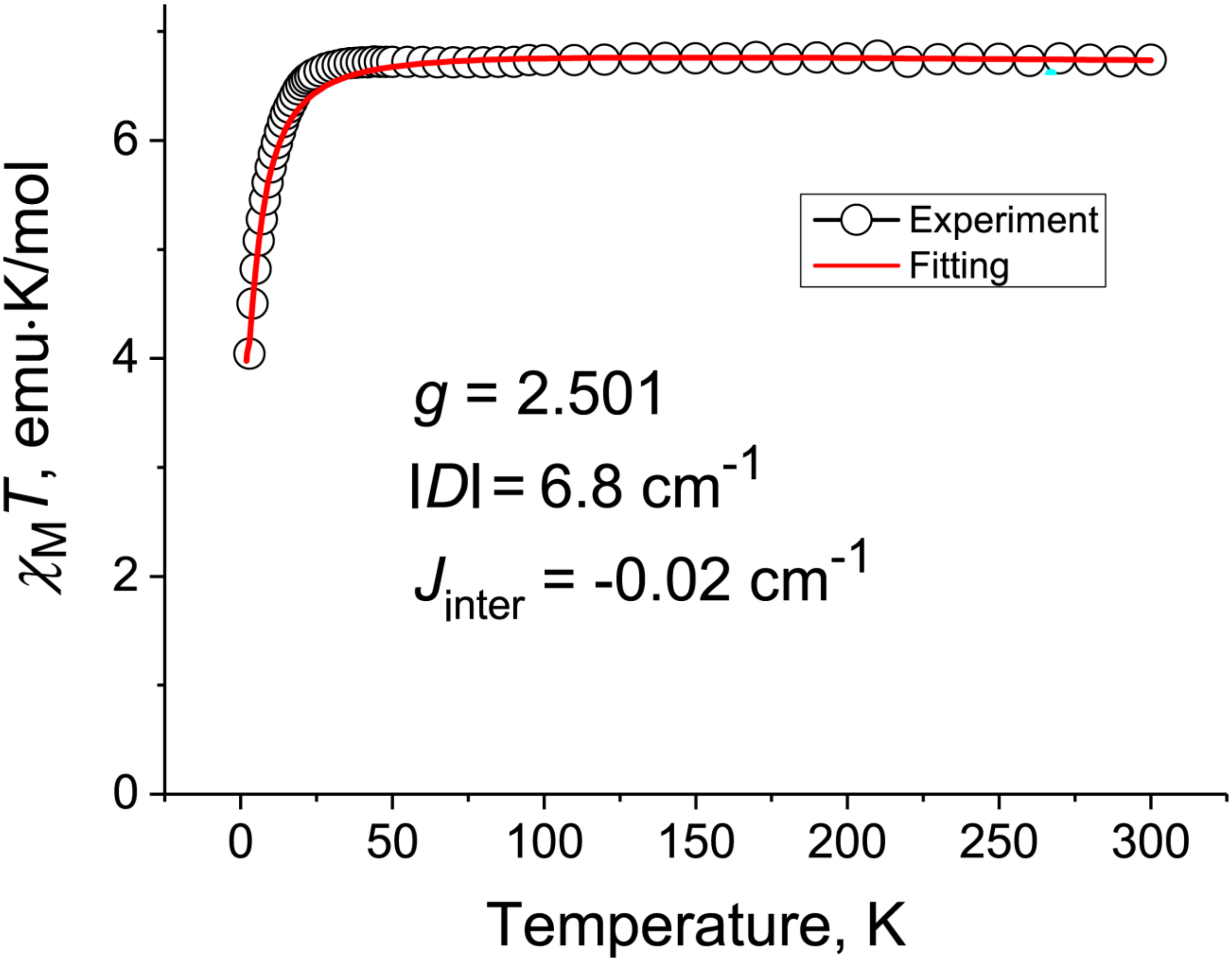

Figure S20. Temperature dependence of $\chi_M T$ values (open circles) and fitting of the data by PHI[7] (red curve) for **2** as for the high-spin system with the S =5/2 spin state. The parameters of fitting are shown.

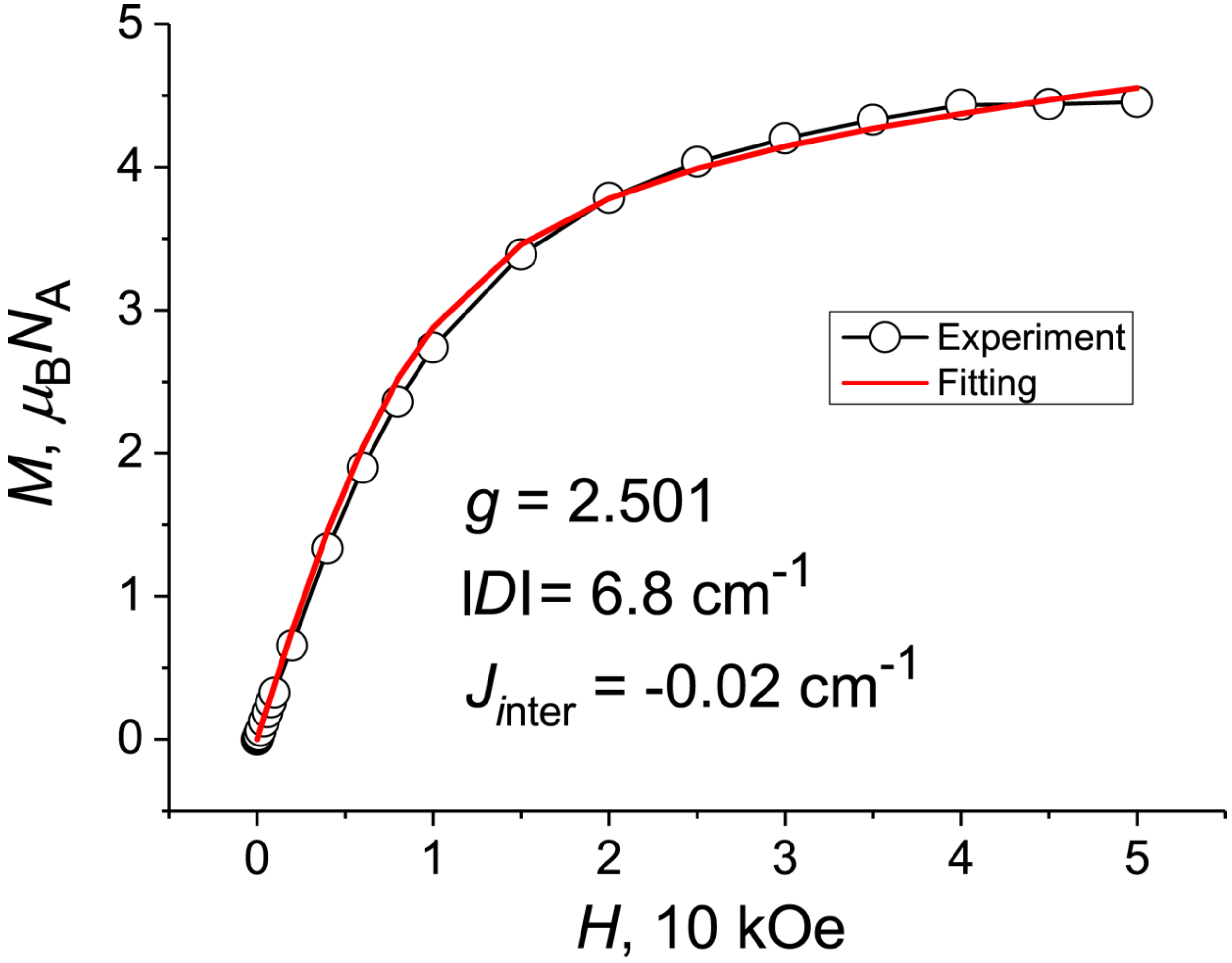

Figure S21. Dependence of magnetization of polycrystalline **2** *vs.* magnetic field (open circles) up to 50 kOe magnetic field at 2 K and fitting of the data by PHI[7] (red curve) as for the high-spin system with the *S* =5/2 spin state. The parameters of fitting are shown.

Complex **4.**

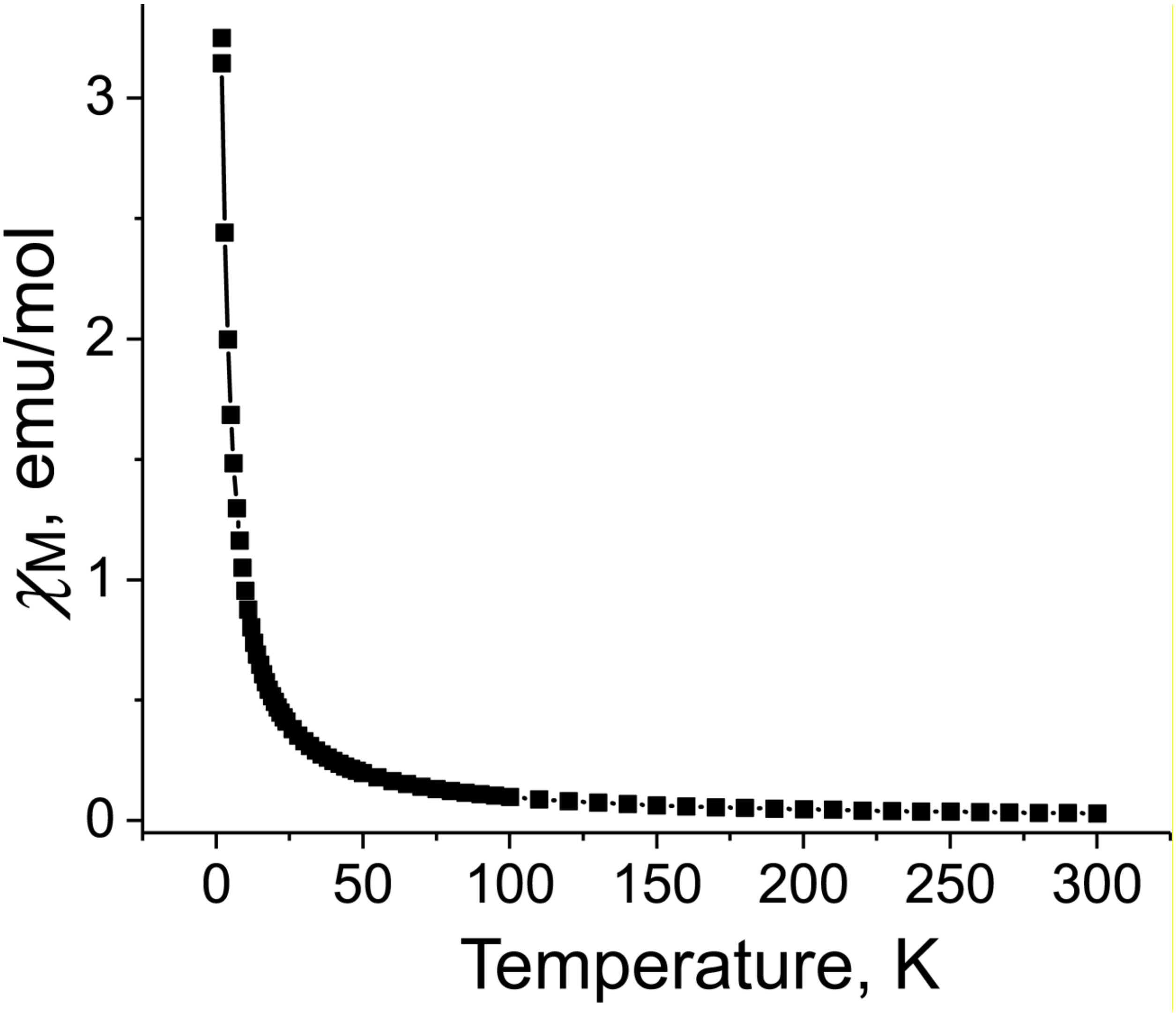

Figure S22. Temperature dependence for molar magnetic susceptibility of polycrystalline $\{(K^+)(\text{crypt})\}\{(\text{Fe}^{\text{II}}\text{I}_2)_2(\text{HATNA})\}^-\cdot 3C_6H_4Cl_2$ (**4**) in the 1.9-300 K range after the subtraction of temperature independent contribution.

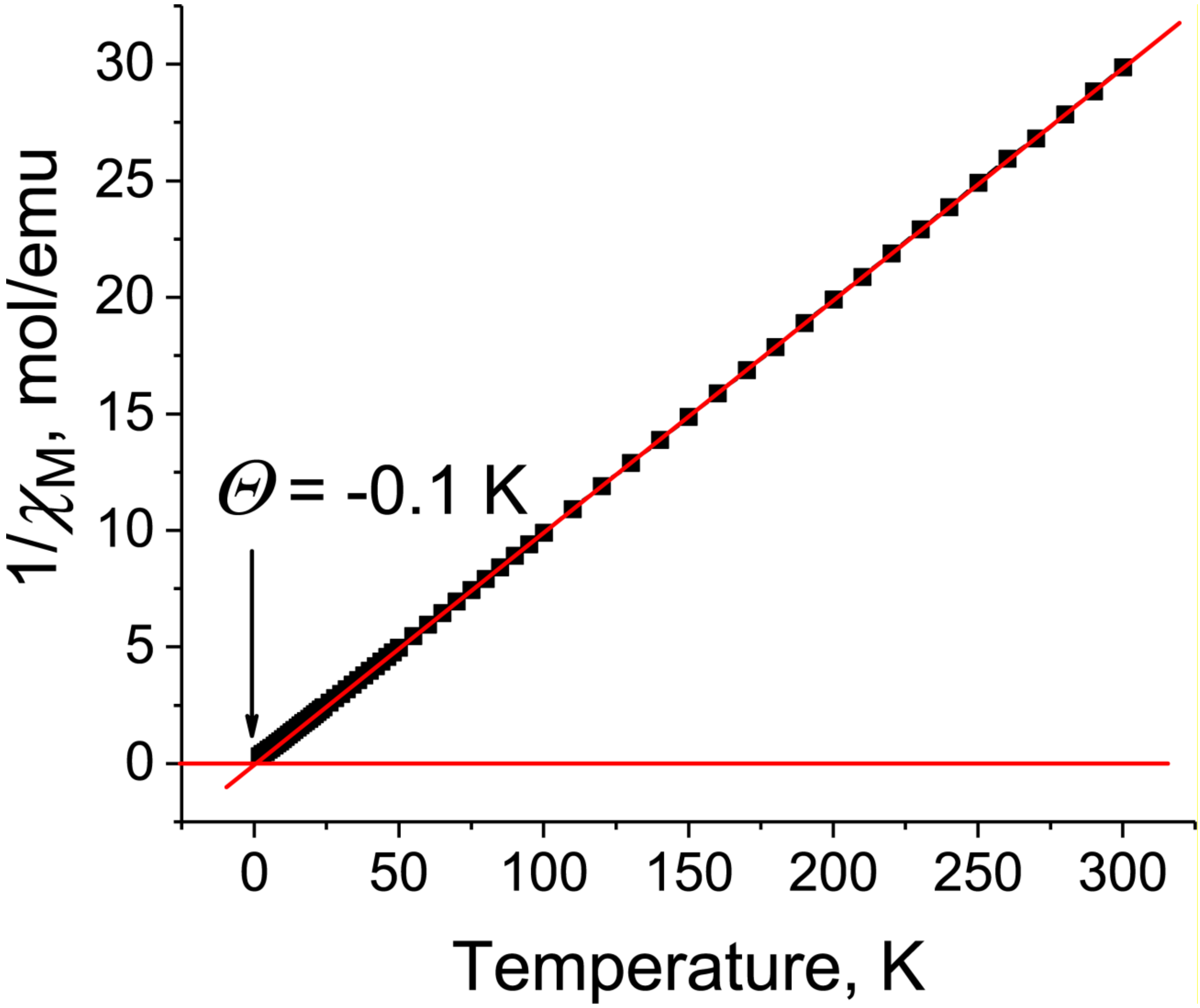

Figure S23. Temperature dependence of reciprocal molar magnetic susceptibility and approximation of the data by the Curie-Weiss law with Weiss temperature (Θ) of -0.1 K for polycrystalline **4** in the 1.9-300 K range.

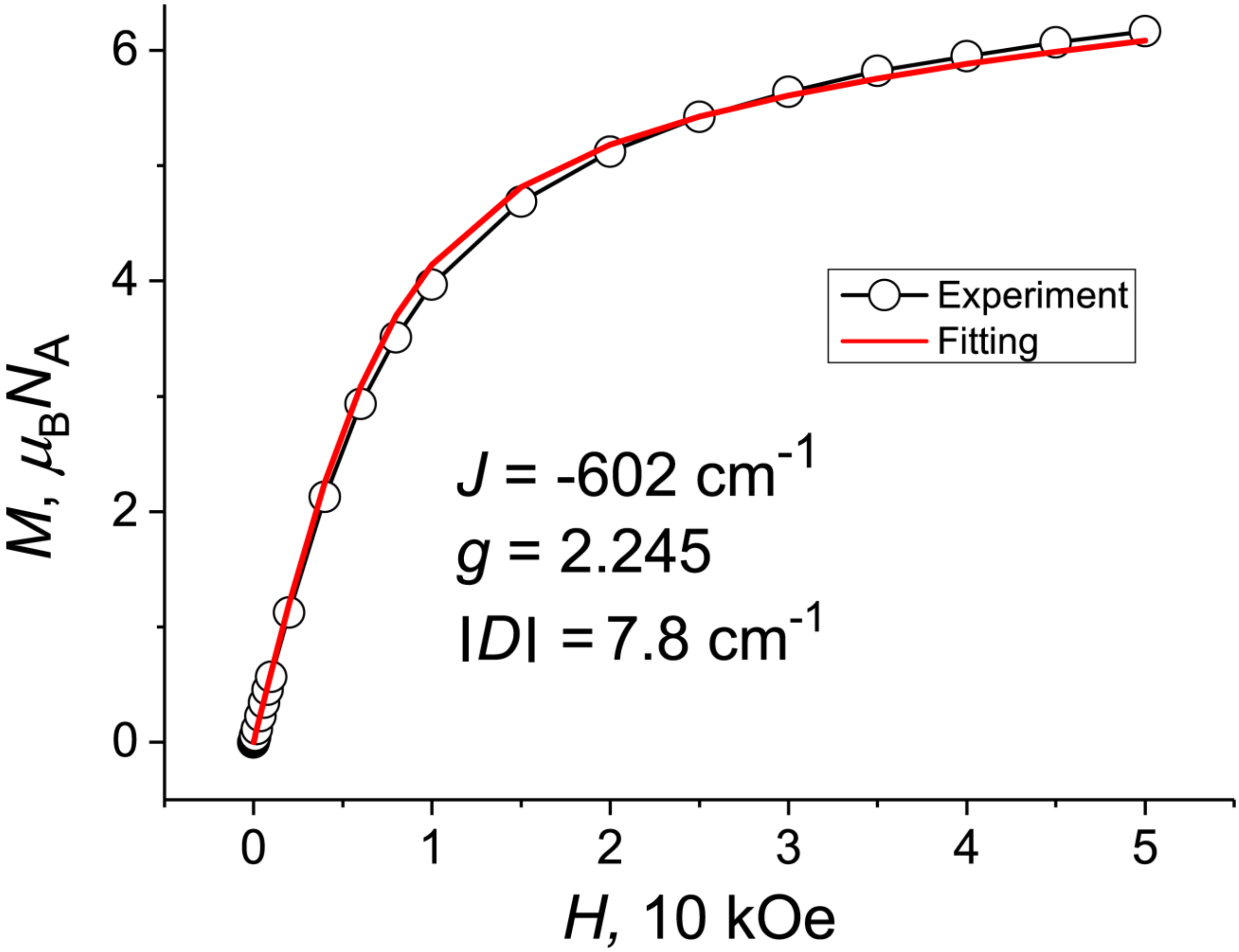

Figure S24. Dependence of magnetization of polycrystalline **4** *vs.* magnetic field (open circles) up to 50 kOe magnetic field at 2 K and fitting of the data by PHI[7] (red curve) with the same parameters as was used for the fitting of temperature dependence of the $\chi_M T$ values (Fig 6b in the manuscript).

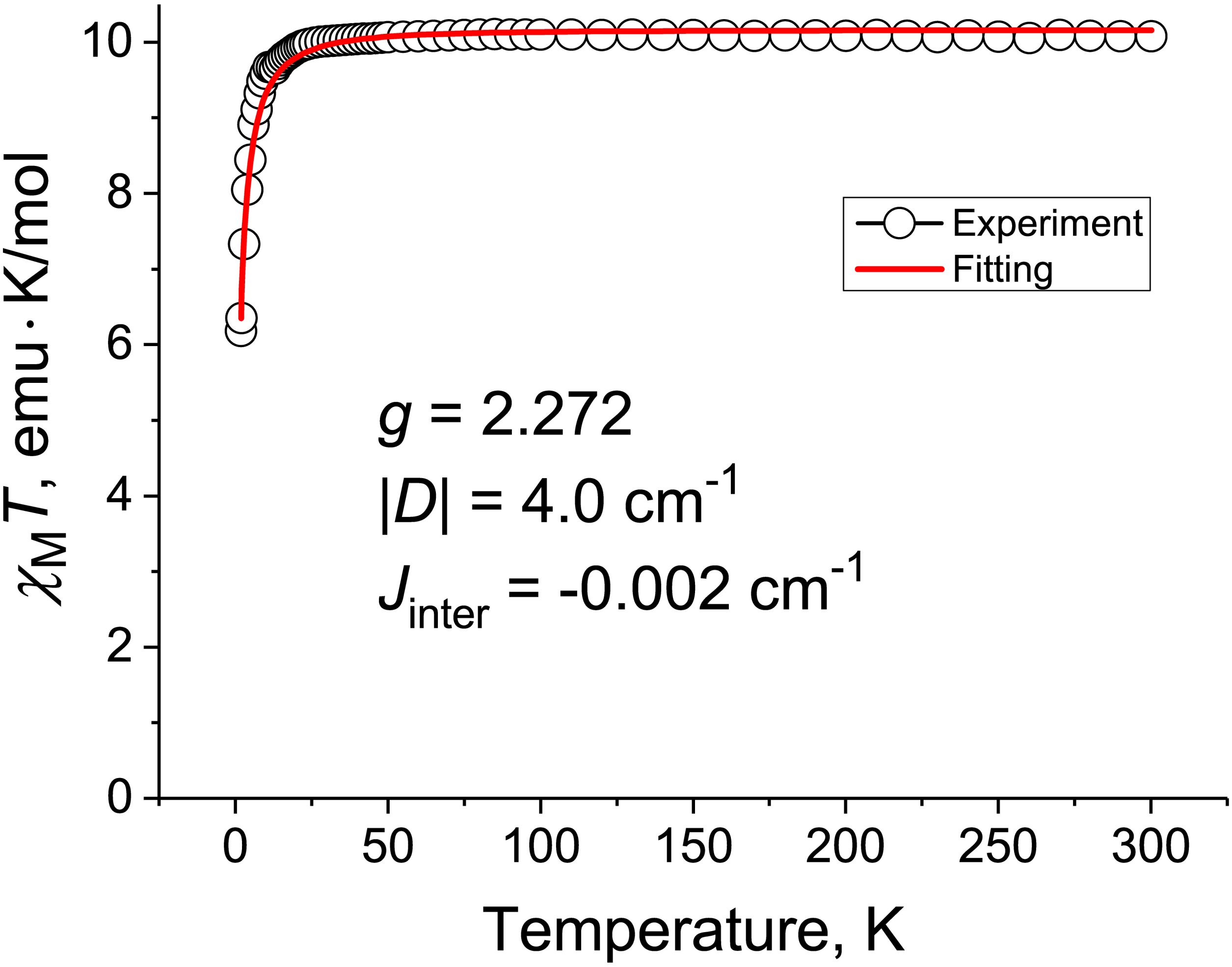

Figure S25. Temperature dependence of $\chi_M T$ values (open circles) and fitting of the data by PHI[7] (red curve) for **4** as for the high-spin system with the $S = 7/2$ spin state. The parameters of fitting are shown.

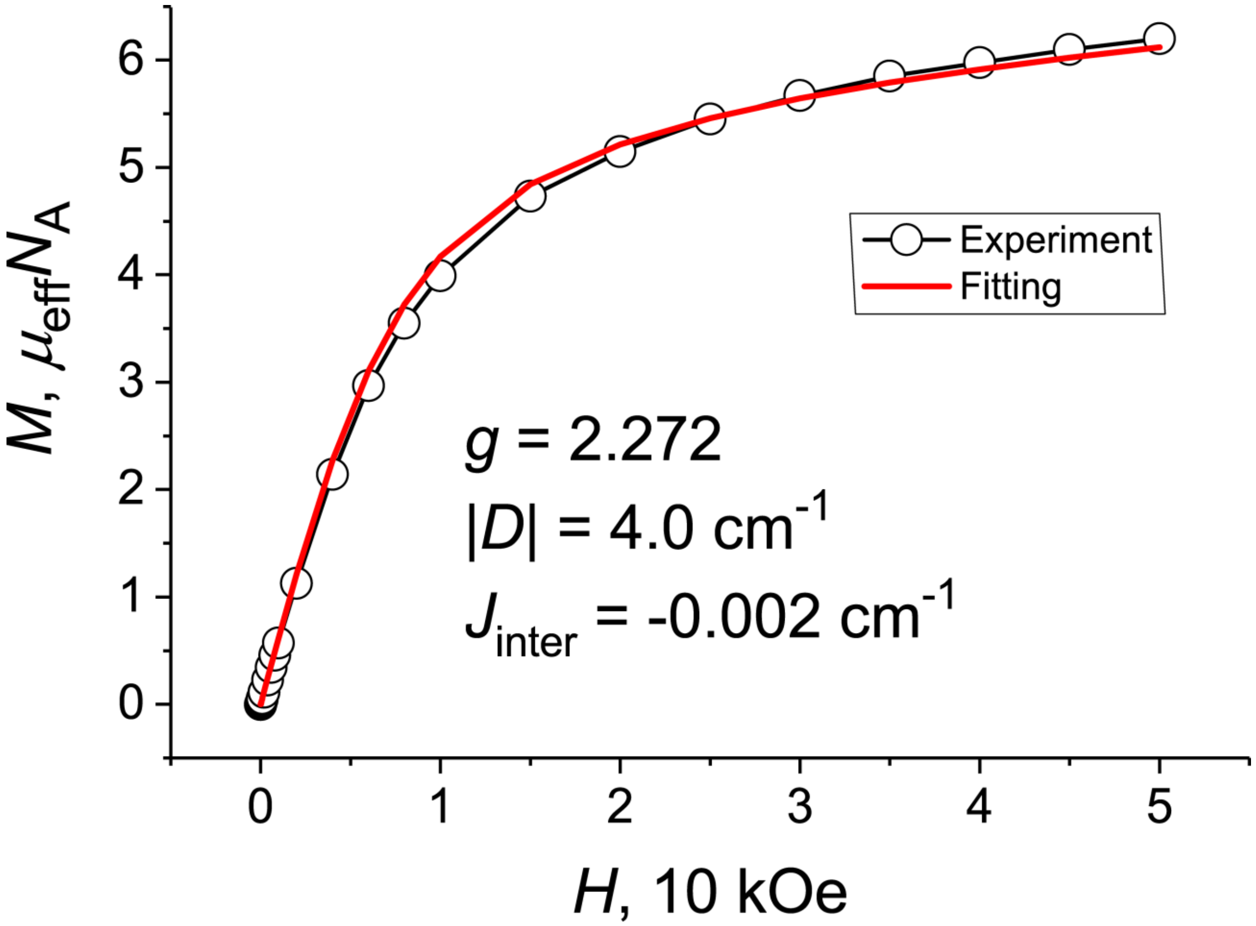

Figure S26. Dependence of magnetization of polycrystalline **4** *vs.* magnetic field (open circles) up to 50 kOe magnetic field at 2 K and fitting of the data by PHI[7] (red curve) as for the high-spin system with the $S = 7/2$ spin state. The parameters of fitting are shown.

Complex **5**

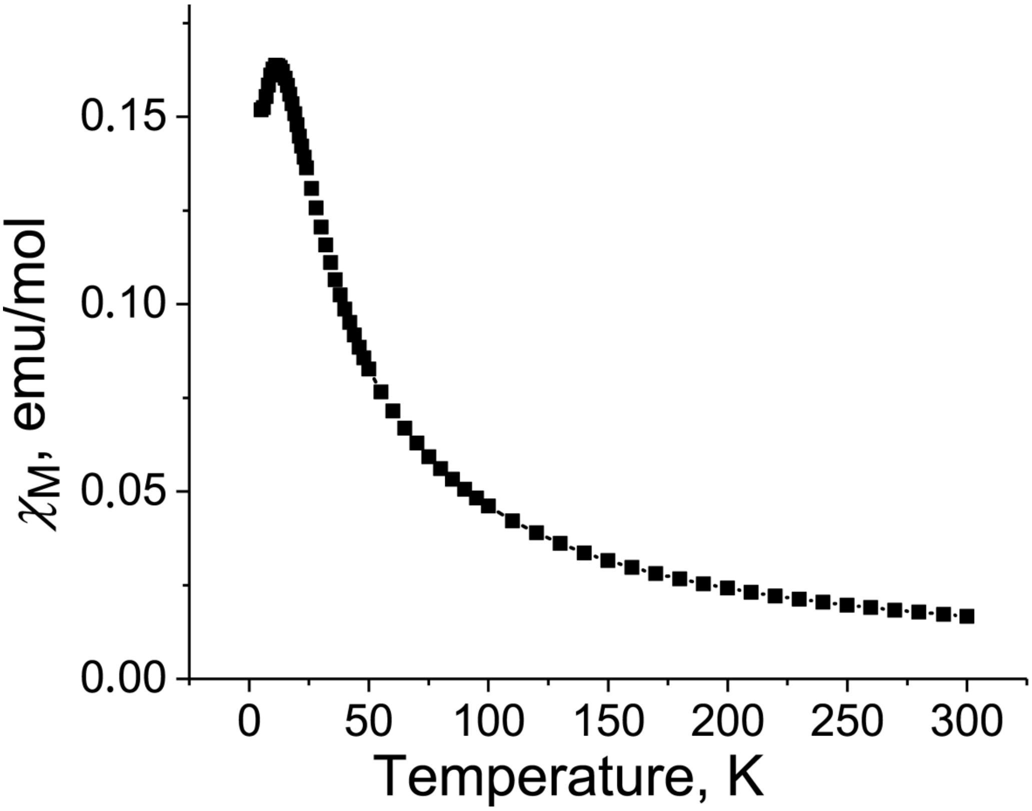

Figure S27. Temperature dependence for molar magnetic susceptibility of polycrystalline $\{(K^+)(crypt)\}\{(Co^{II}I_2)_2(HATA)\}^-\cdot C_6H_4Cl_2$ (**5**) in the 1.9-300 K range after the subtraction of temperature independent contribution and Curie impurities (less than 6% of *S* = 1/2 spins per formula unit).

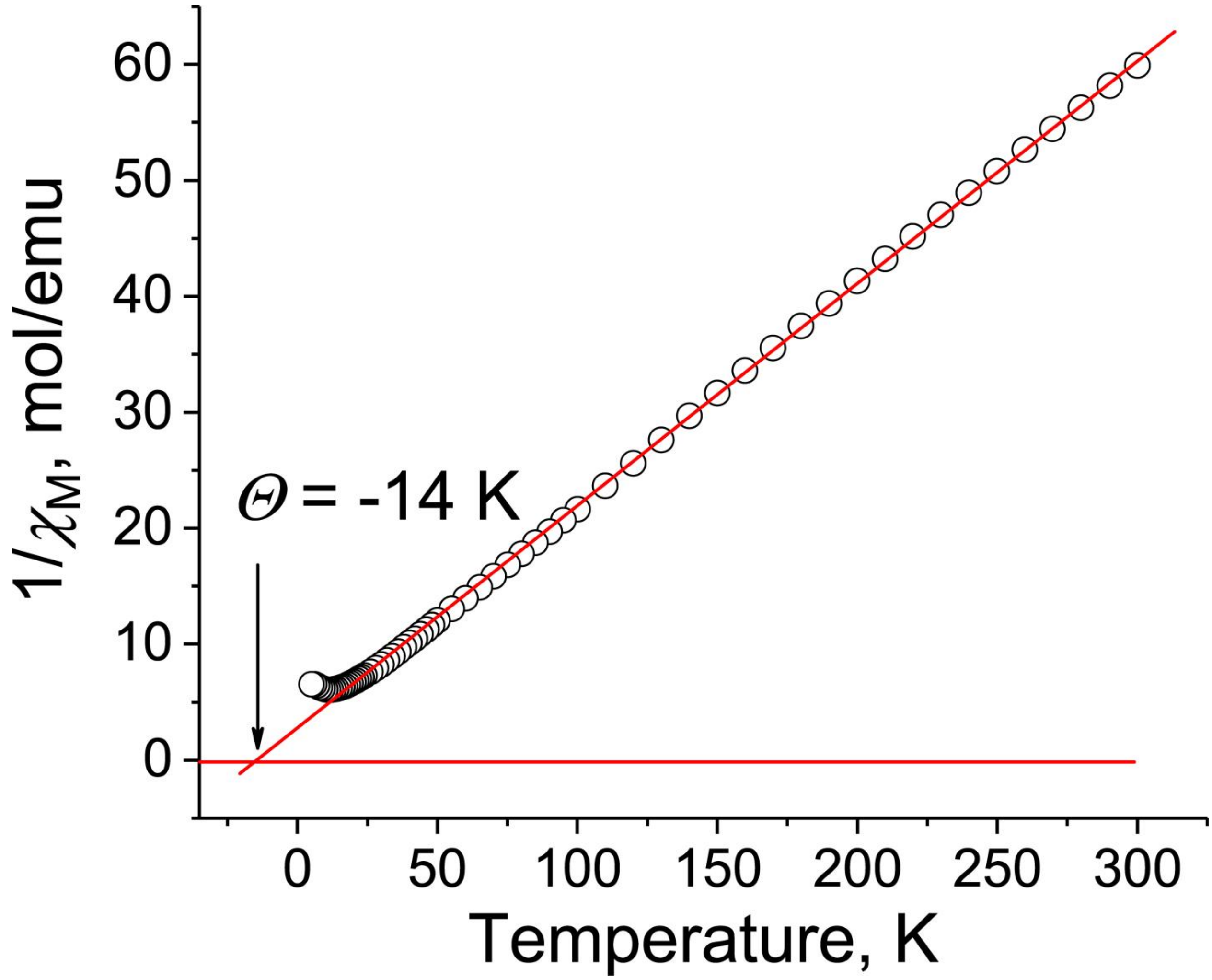

Figure S28. Temperature dependence of reciprocal molar magnetic susceptibility and approximation of the data by the Curie-Weiss law with Weiss temperature (*Θ*) of -14 K for polycrystalline **5** in the 1.9-300 K range.

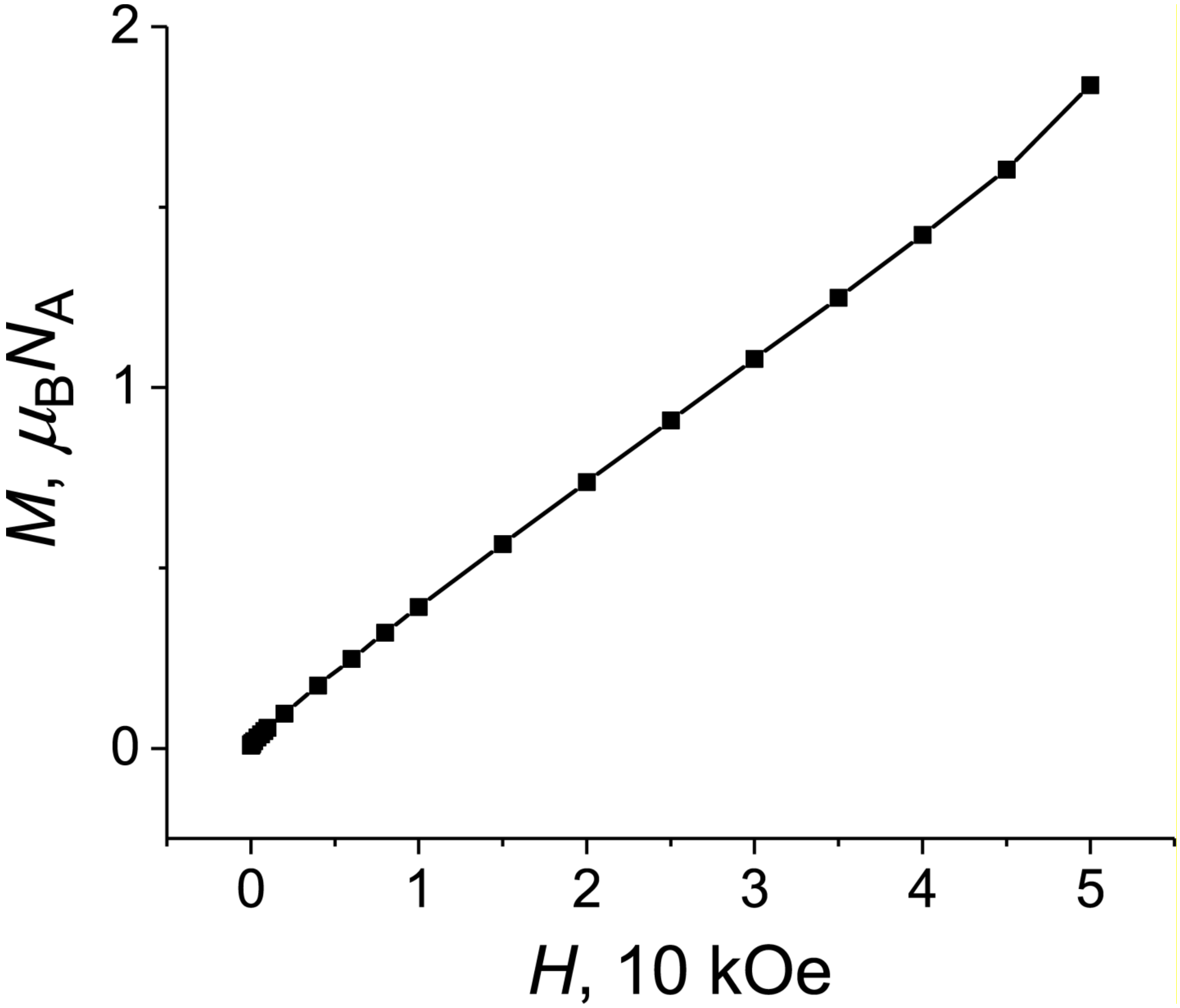

Figure S29. Dependence of magnetization for polycrystalline **5** *vs* magnetic field up to 50 kOe at 2 K (black line is a guide to the eye). Mainly contribution from the Curie impurities is observed at 2 K.

Complex **6**.

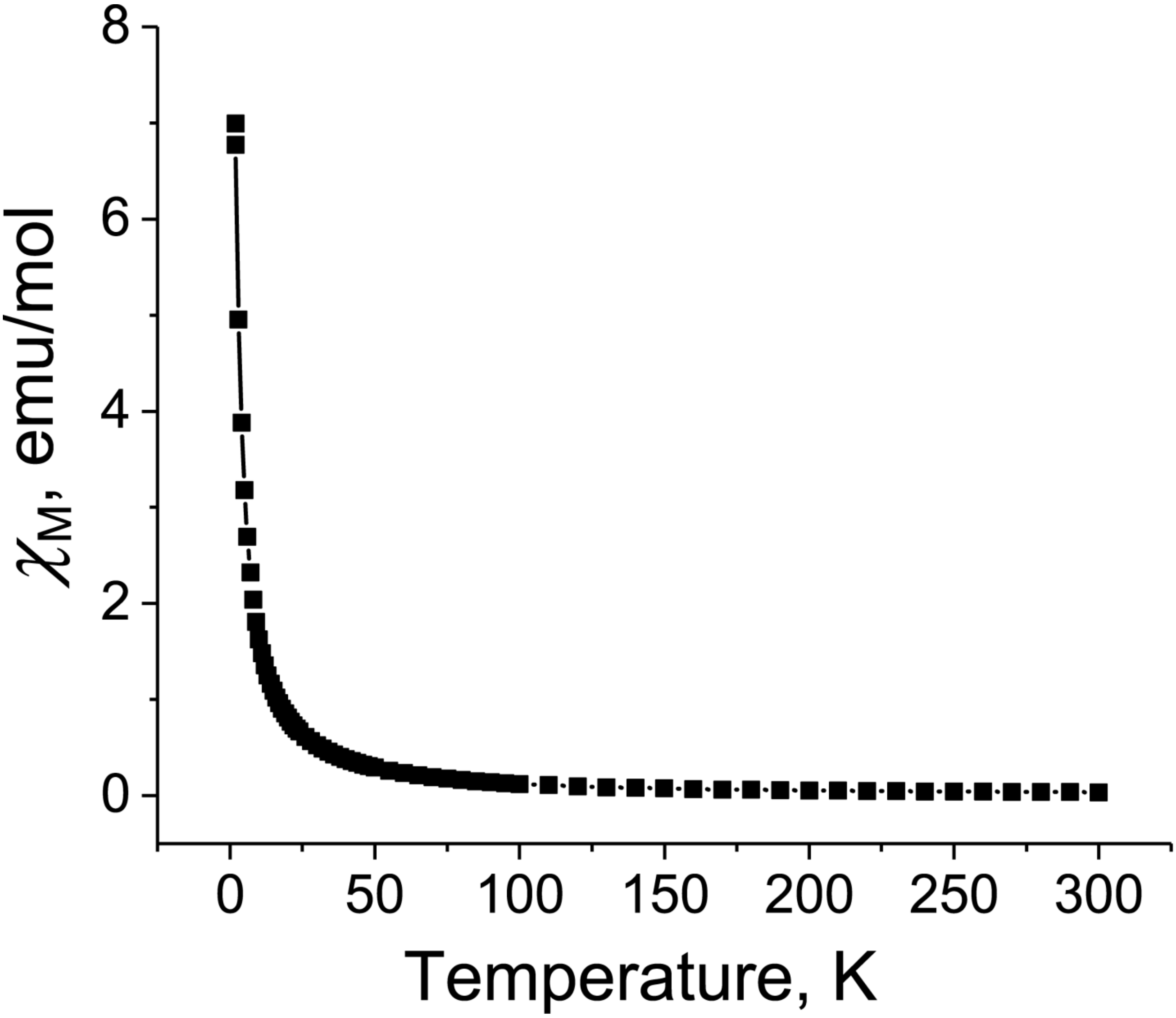

Figure S30. Temperature dependence for molar magnetic susceptibility of polycrystalline $\{(K^+)(crypt)\}\{(Fe^{II}Cl_2)_3(HATNA)\}^- \cdot C_6H_{14}$ (**6**) in the 1.9-300 K range after the subtraction of temperature independent contribution.

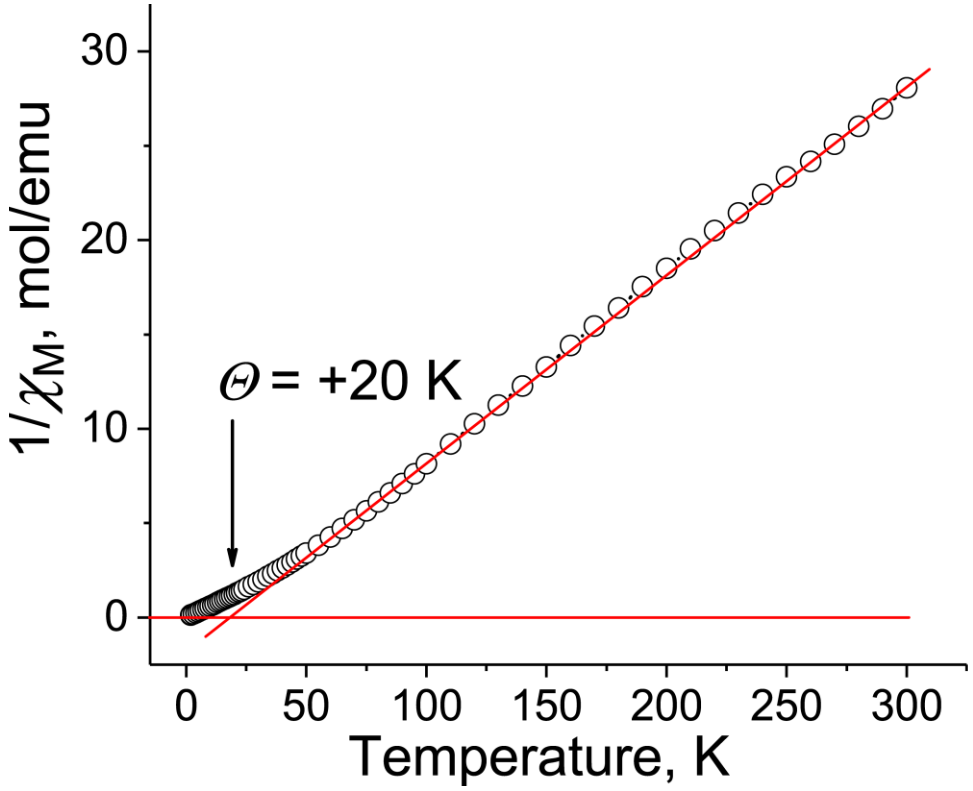

Figure S31. Temperature dependence of reciprocal molar magnetic susceptibility of polycrystalline **6** allowing to determine Weiss temperature of Θ = +20 K.

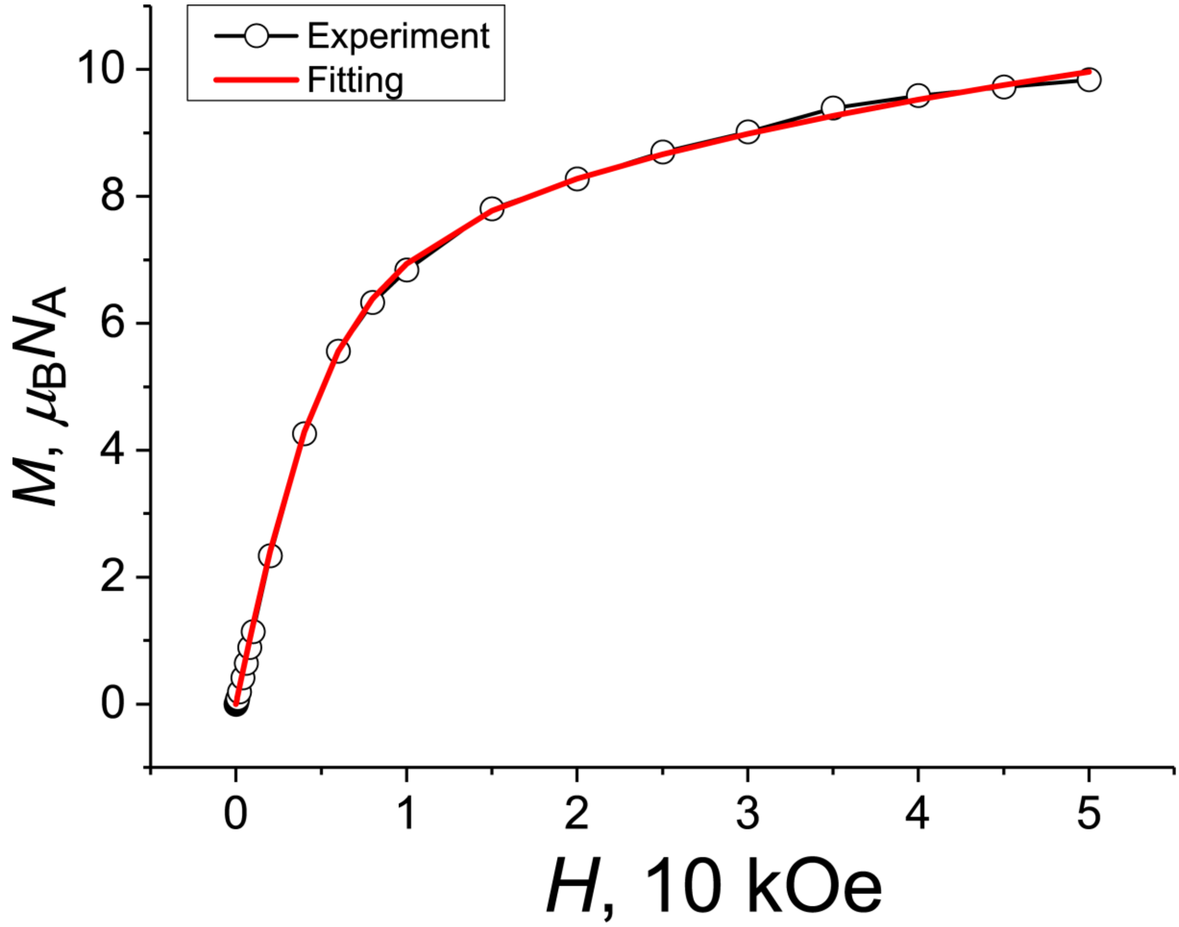

Fig. S32. Dependence of magnetization for polycrystalline **6** *vs.* magnetic field up to 50 kOe at 2 K and fitting of the data by PHI[7] (red curve) with the same parameters as was used for the fitting of the $\chi_M T$ values (Fig. 7a in the manuscript).

Complex 7.

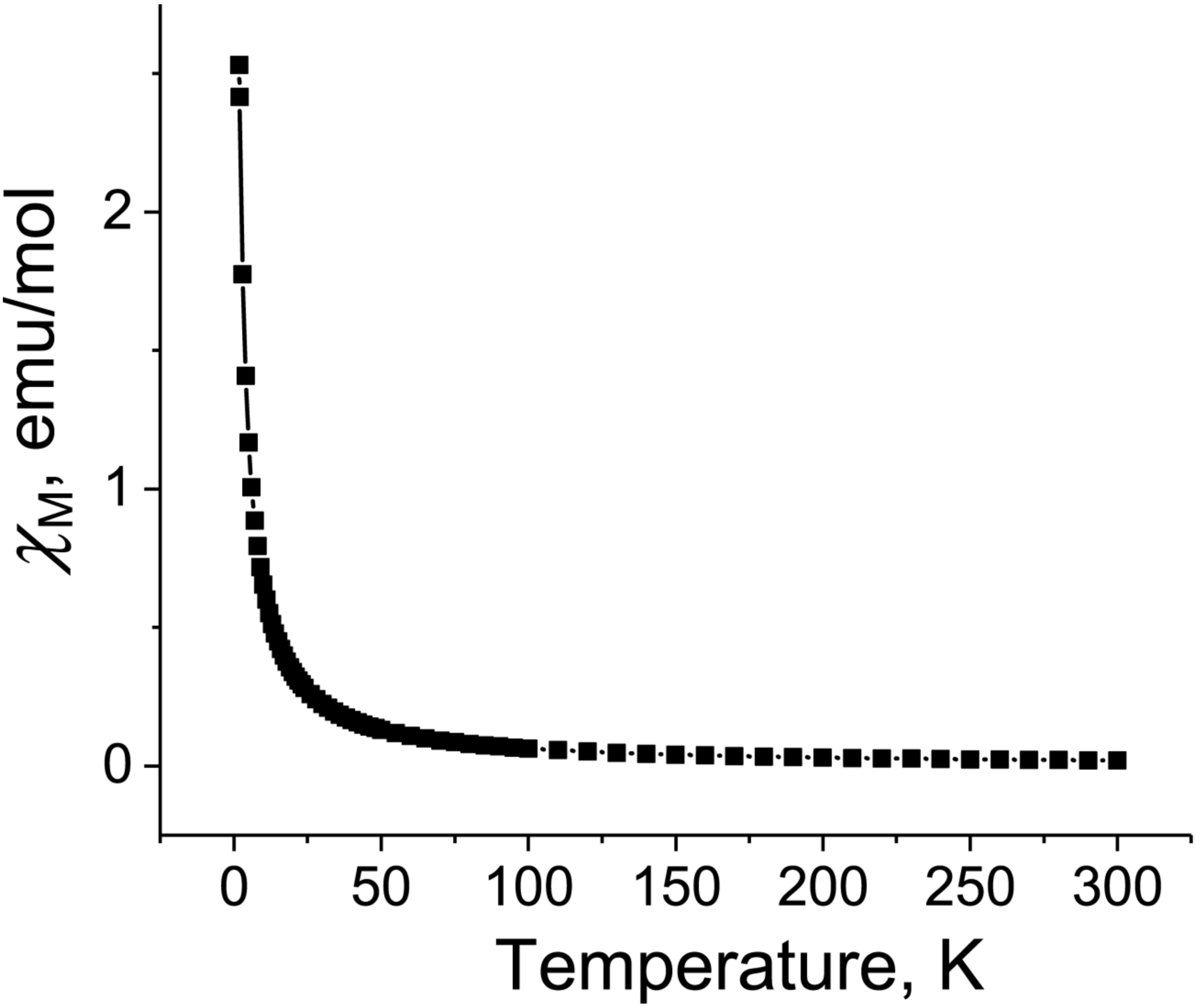

Figure S33. Temperature dependence for molar magnetic susceptibility of polycrystalline $\{(K^+)(\text{crypt})\}\{(\text{Co}^{II}\text{Cl}_2)_3(\text{HATNA})\}^-$ (**7**) in the 1.9-300 K range after the subtraction of temperature independent contribution.

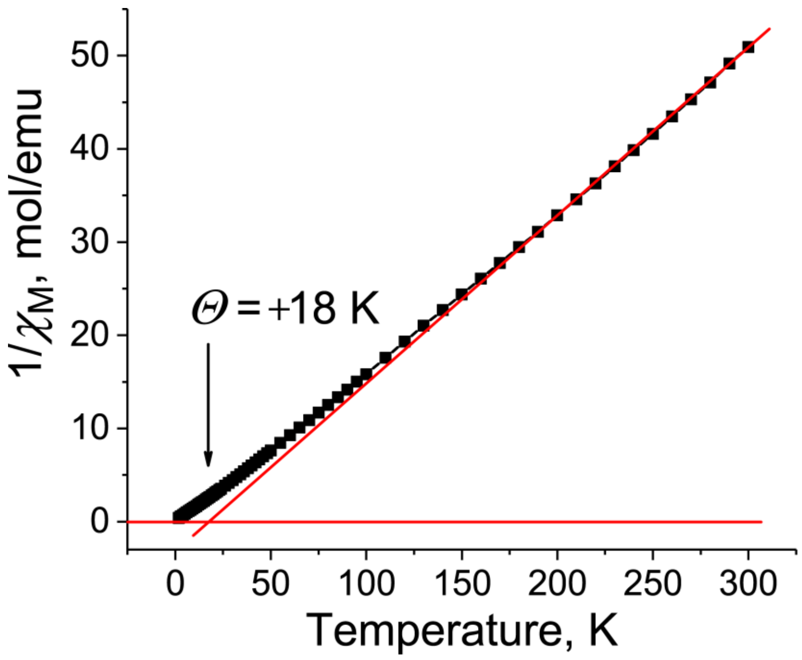

Figure S34. Temperature dependence of reciprocal molar magnetic susceptibility of polycrystalline **7** allowing to determine Weiss temperature of Θ = +18 K

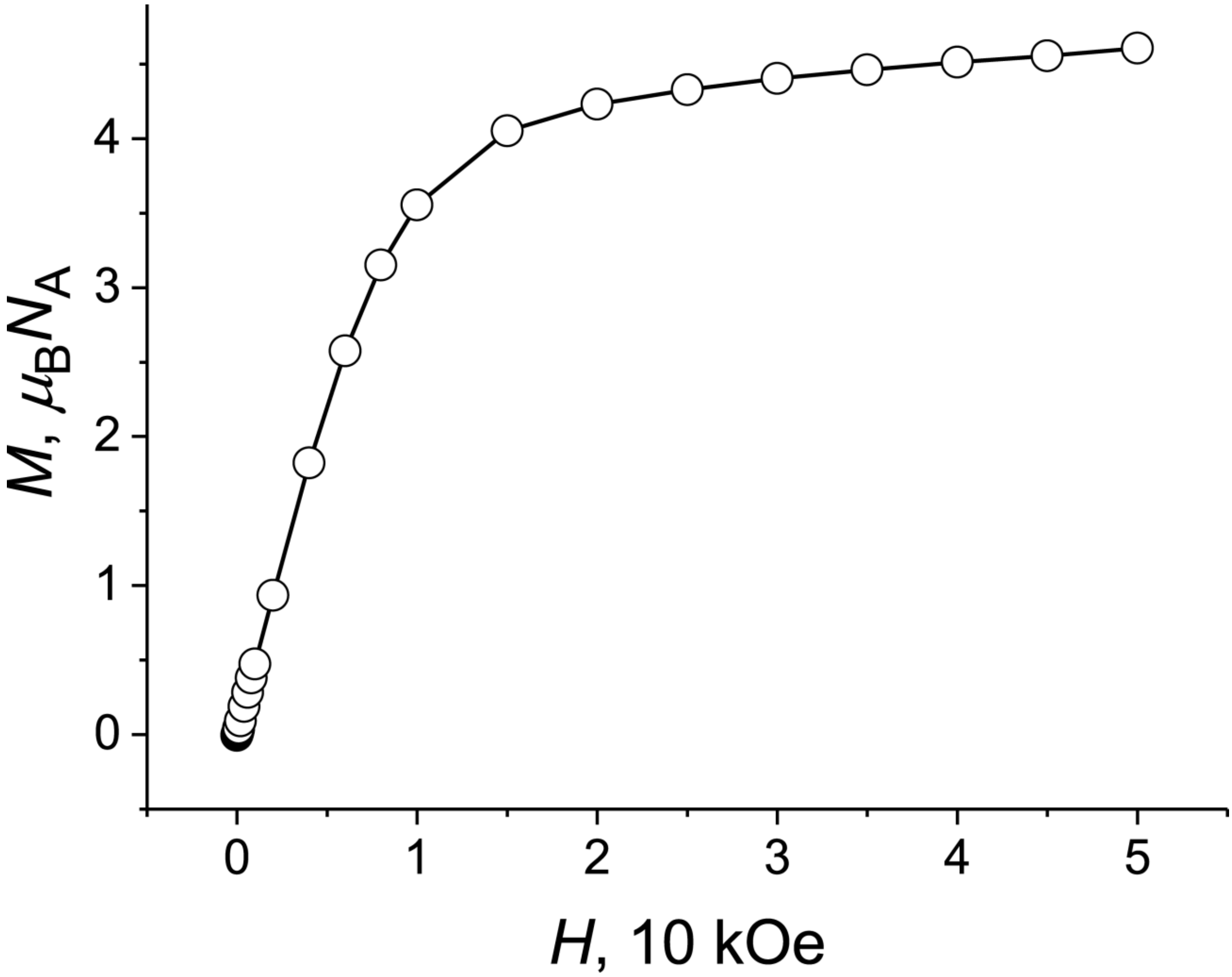

Figure S35. Dependence of magnetization of polycrystalline **7** *vs.* magnetic field up to 50 kOe at 2 K (black line is a guide to the eye).

Complex **8**.

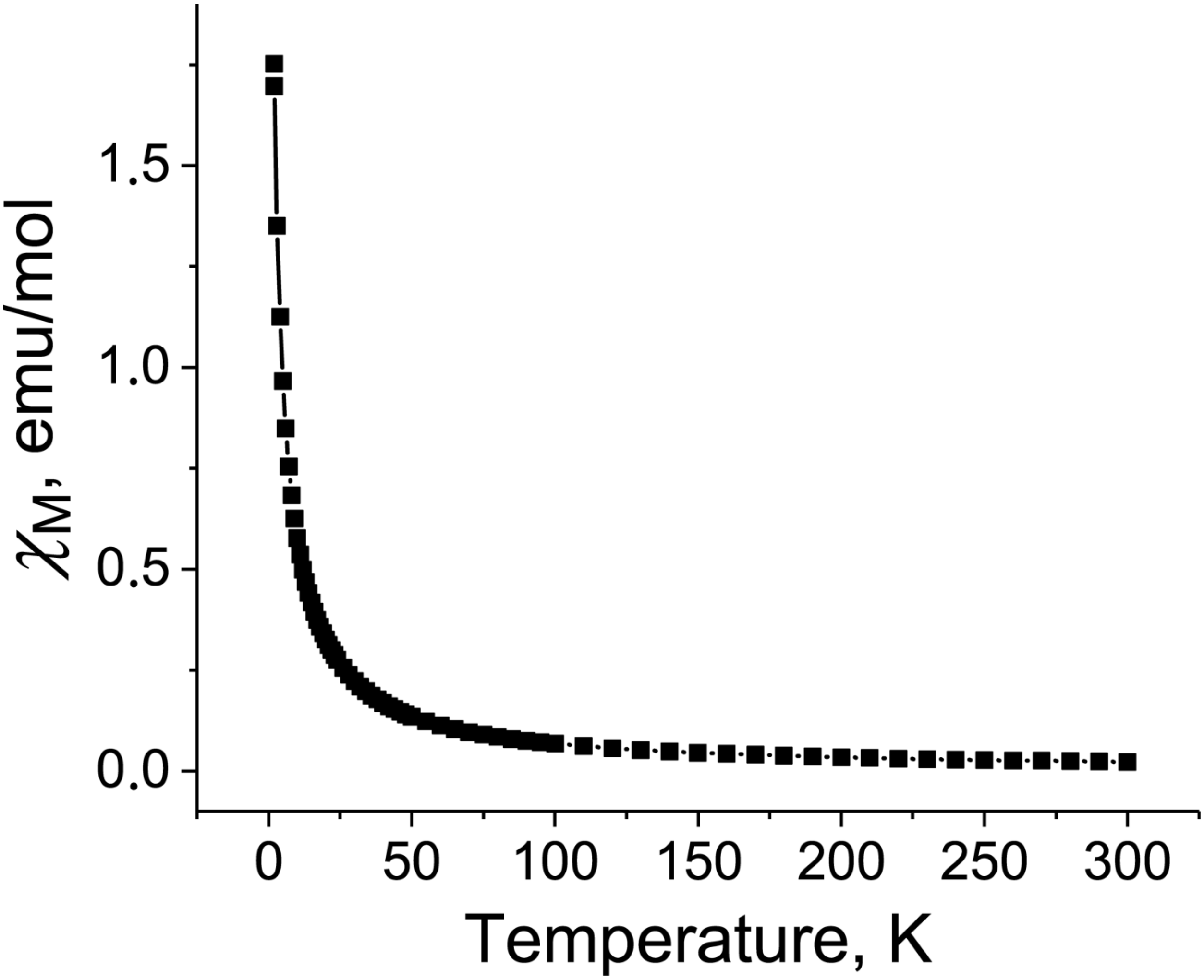

Figure S36. Temperature dependence for molar magnetic susceptibility of polycrystalline $\{(K^+)(crypt)\}_2\{(Fe^{II}Cl_2)_2(HATNA)\}^{2-}\cdot 3C_6H_4Cl_2$ (**8**) in the 1.9-300 K range after the subtraction of temperature independent contribution.

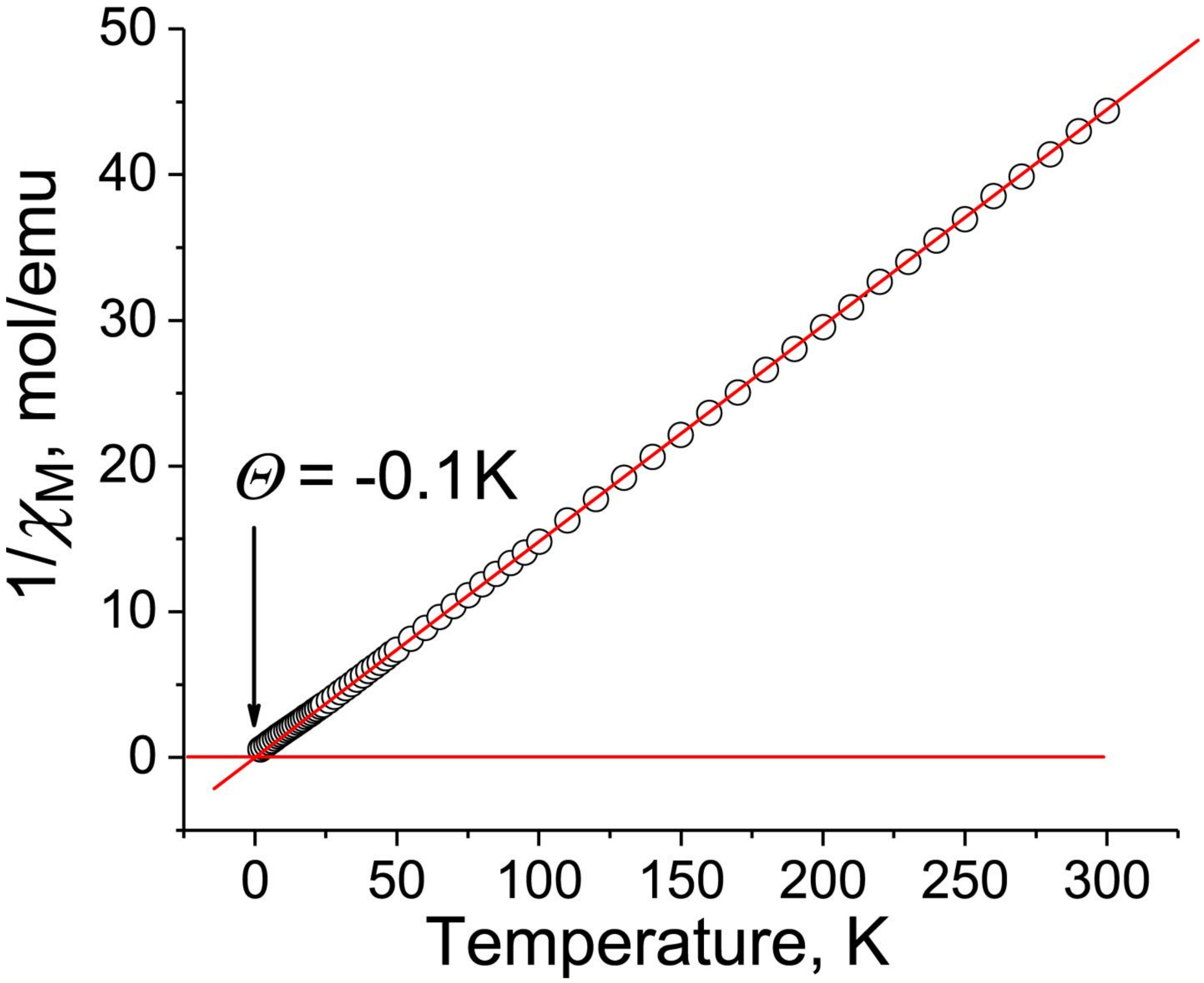

Figure S37. Temperature dependence of reciprocal molar magnetic susceptibility and approximation of the data by the Curie-Weiss law with Weiss temperature (Θ) of -0.1 K for polycrystalline **8** in the 1.9-300 K range.

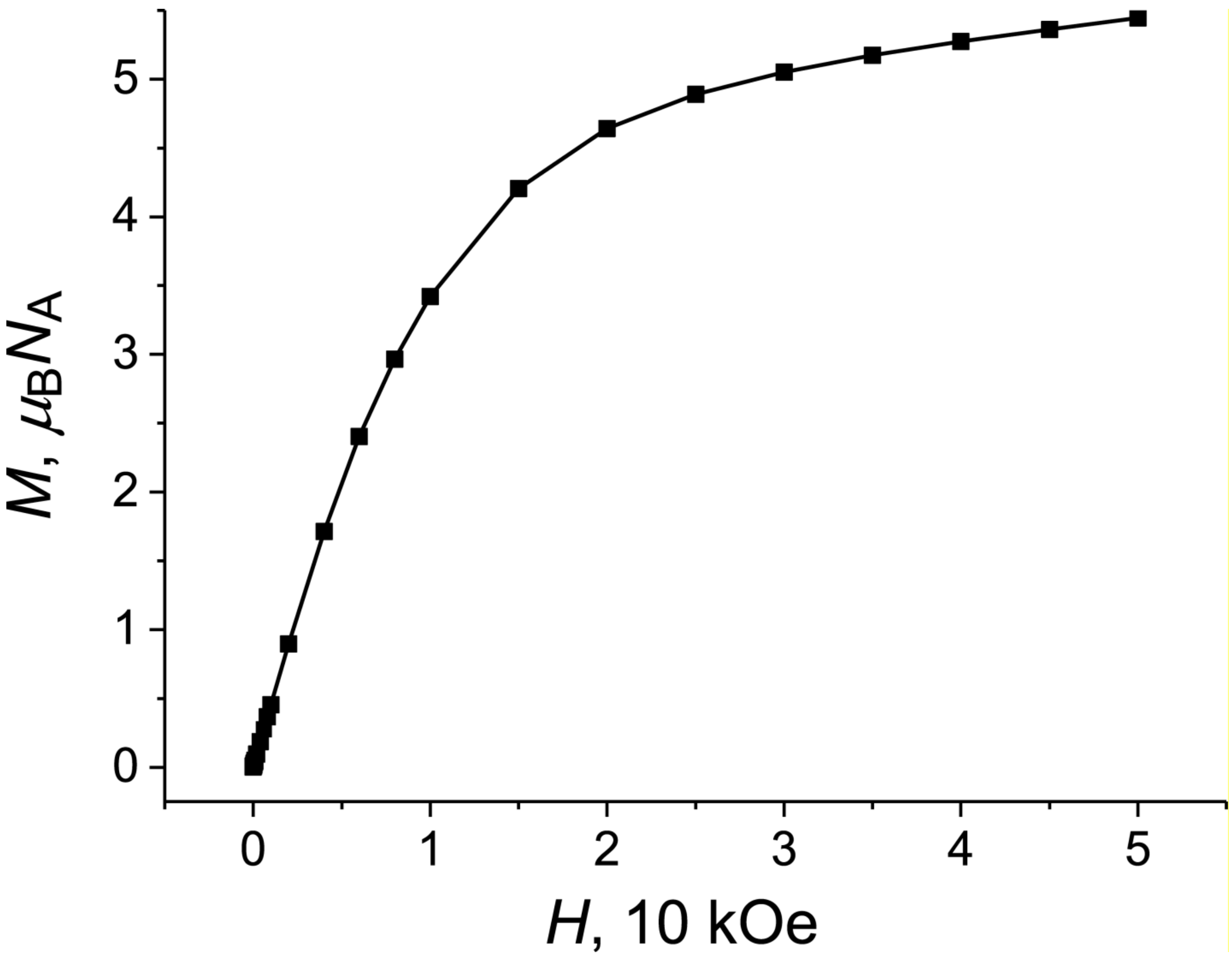

Figure S38. Dependence of magnetization of polycrystalline **8** *vs.* magnetic field up to 50 kOe at 2 K (black line is a guide to the eye).

Complex **9**.

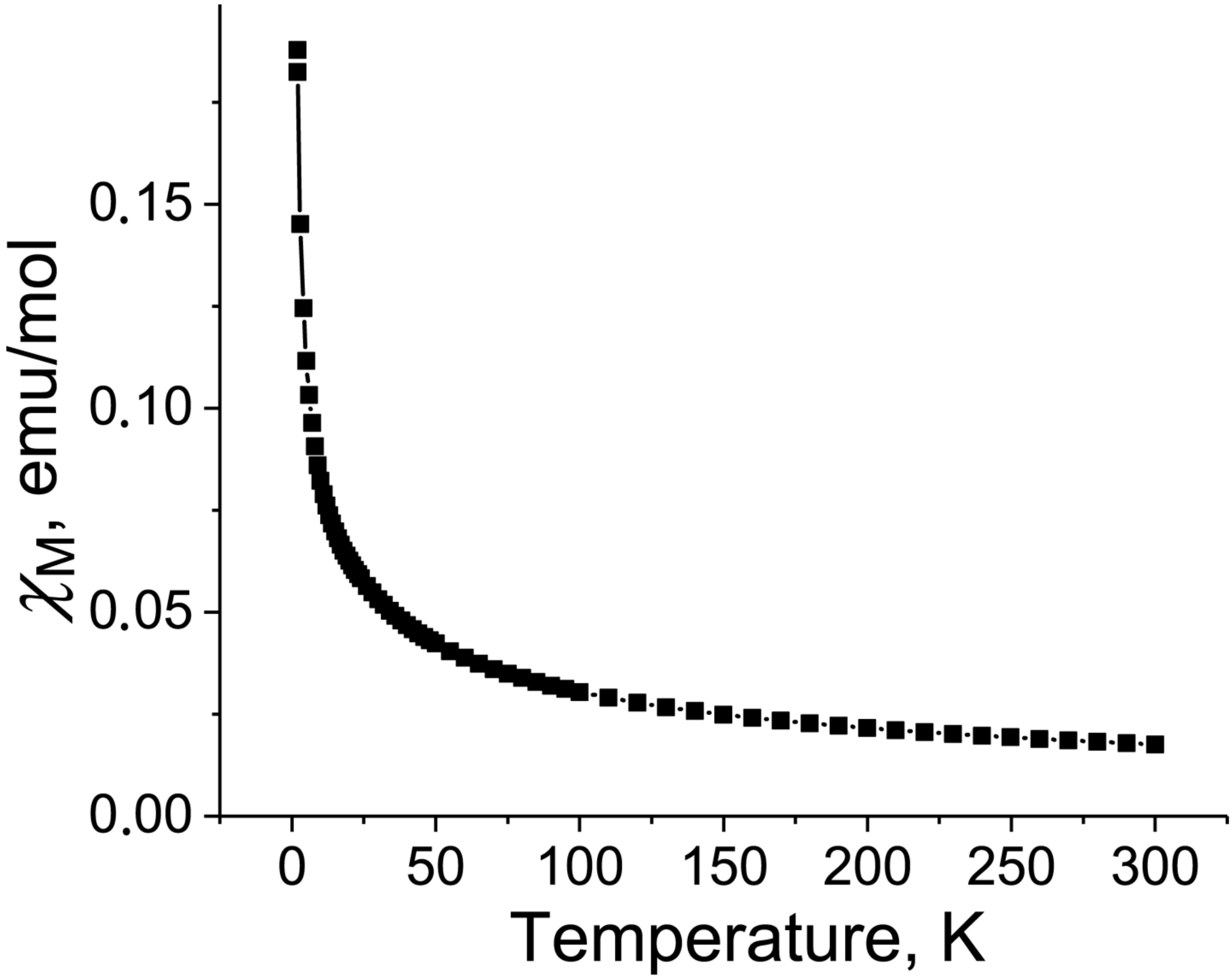

Figure S39. Temperature dependence for molar magnetic susceptibility of polycrystalline $\{(K^+)(crypt)\}_2\{(Co^{II}I_2)_3(HATA)\}^{2-}\cdot 3C_6H_4Cl_2$ (**9**) in the 1.9-300 K range after the subtraction of temperature independent contribution.

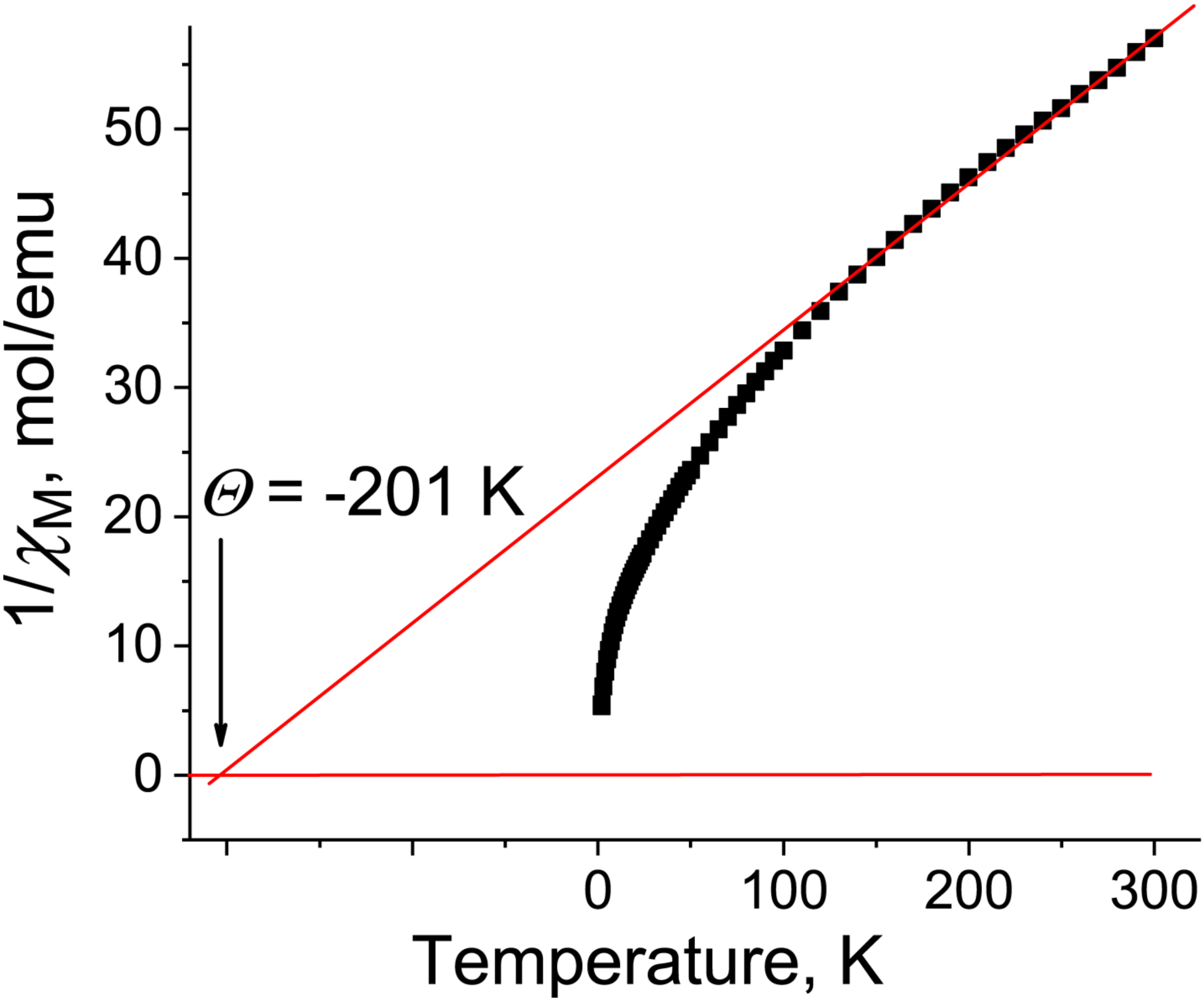

Figure S40. Temperature dependence of reciprocal molar magnetic susceptibility and approximation of the data by the Curie-Weiss law with Weiss temperature (*Θ*) of -201 K for polycrystalline **9** in the 1.9-300 K range.

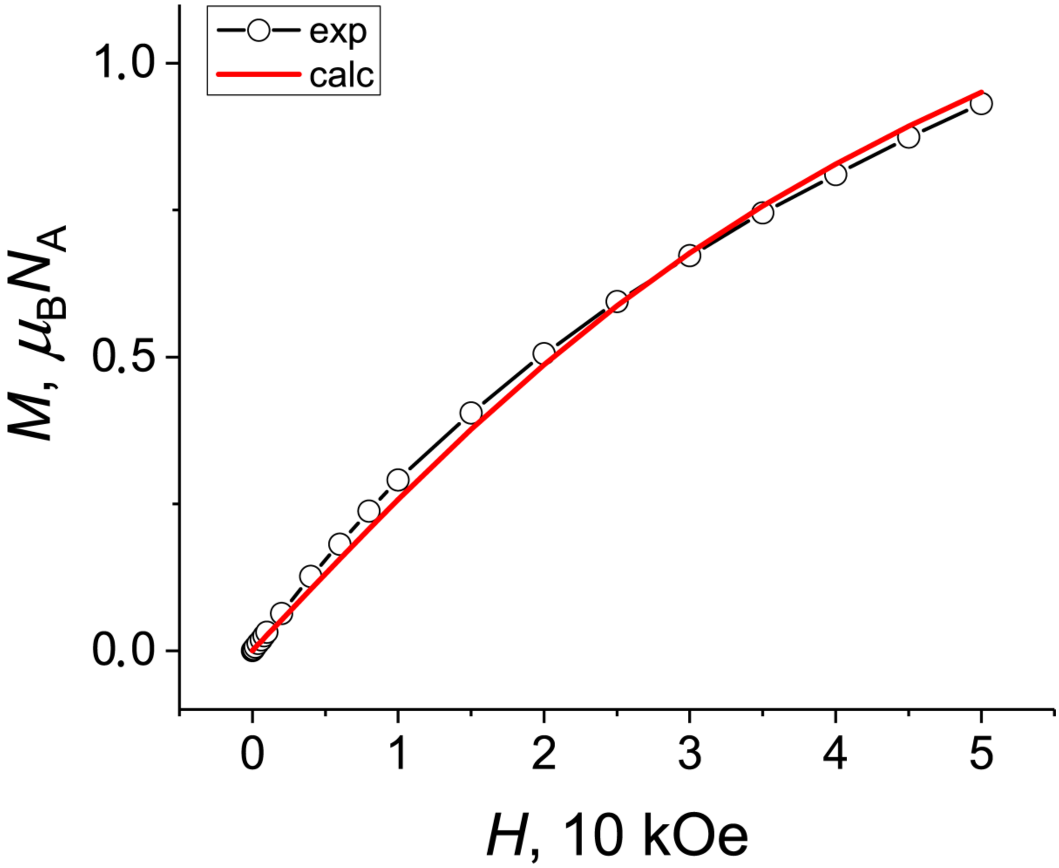

Figure S41. Dependence of magnetization of polycrystalline **9** *vs.* magnetic field (open circles) up to 50 kOe magnetic field at 2 K and fitting of the data by PHI[7] (red curve) with the same parameters as was used for the fitting of temperature dependence of molar magnetic susceptibility (Fig. 8b in the manuscript).

Compound **10**

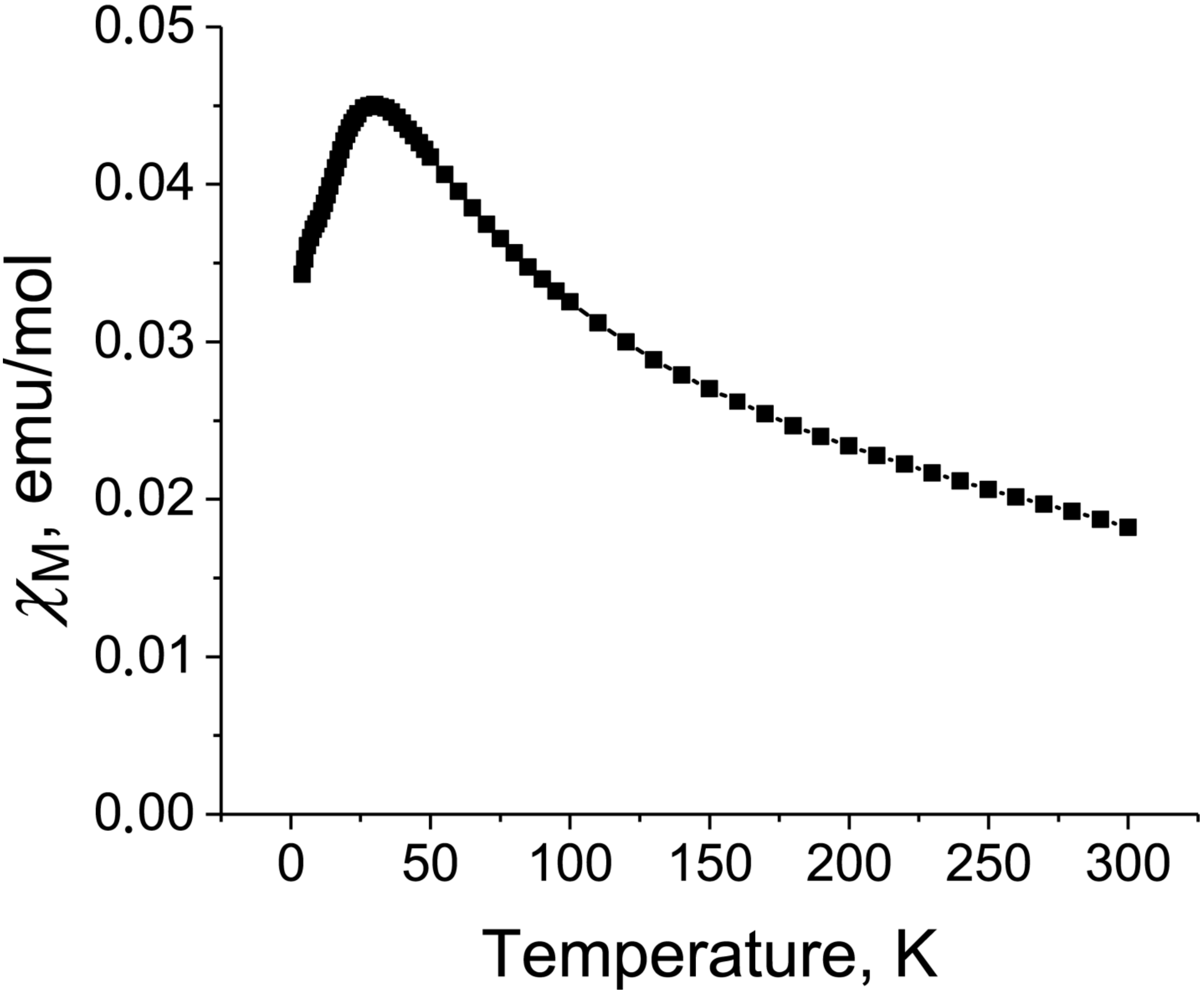

Figure S42. Temperature dependence for molar magnetic susceptibility of polycrystalline $(CV^+)_2\{(Co^{II}Cl_2)_3(HATA)\}^{2-}\cdot 4C_6H_4Cl_2$ (**10**) in the 1.9-300 K range after the subtraction of temperature independent contribution and contribution from the Curie impurities (less than 6% of $S = 1/2$ spins per formula unit.

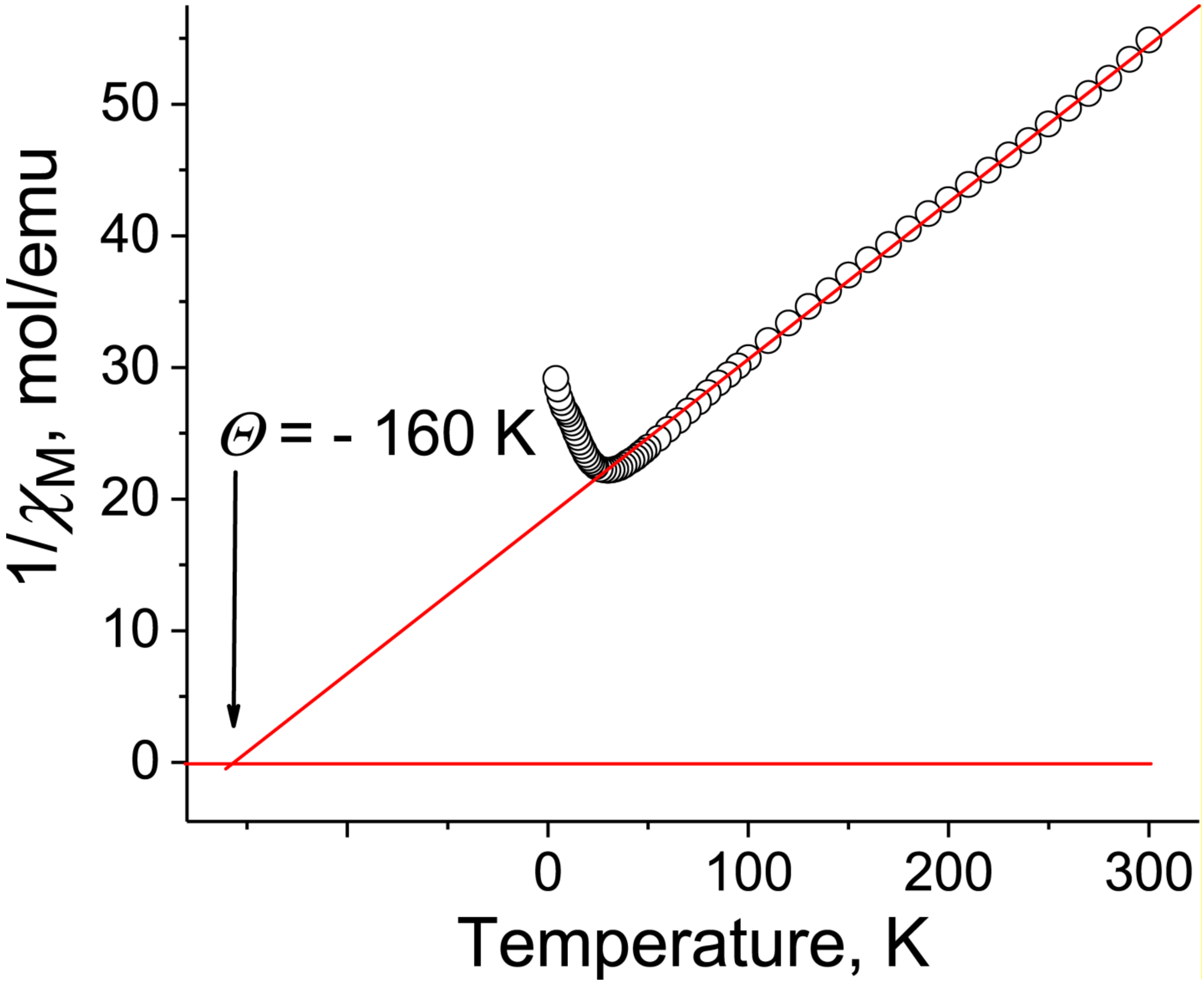

Figure S43. Temperature dependence of reciprocal molar magnetic susceptibility and approximation of the data by the Curie-Weiss law with Weiss temperature (*Θ*) of -160 K for polycrystalline **10** in the 1.9-300 K range.

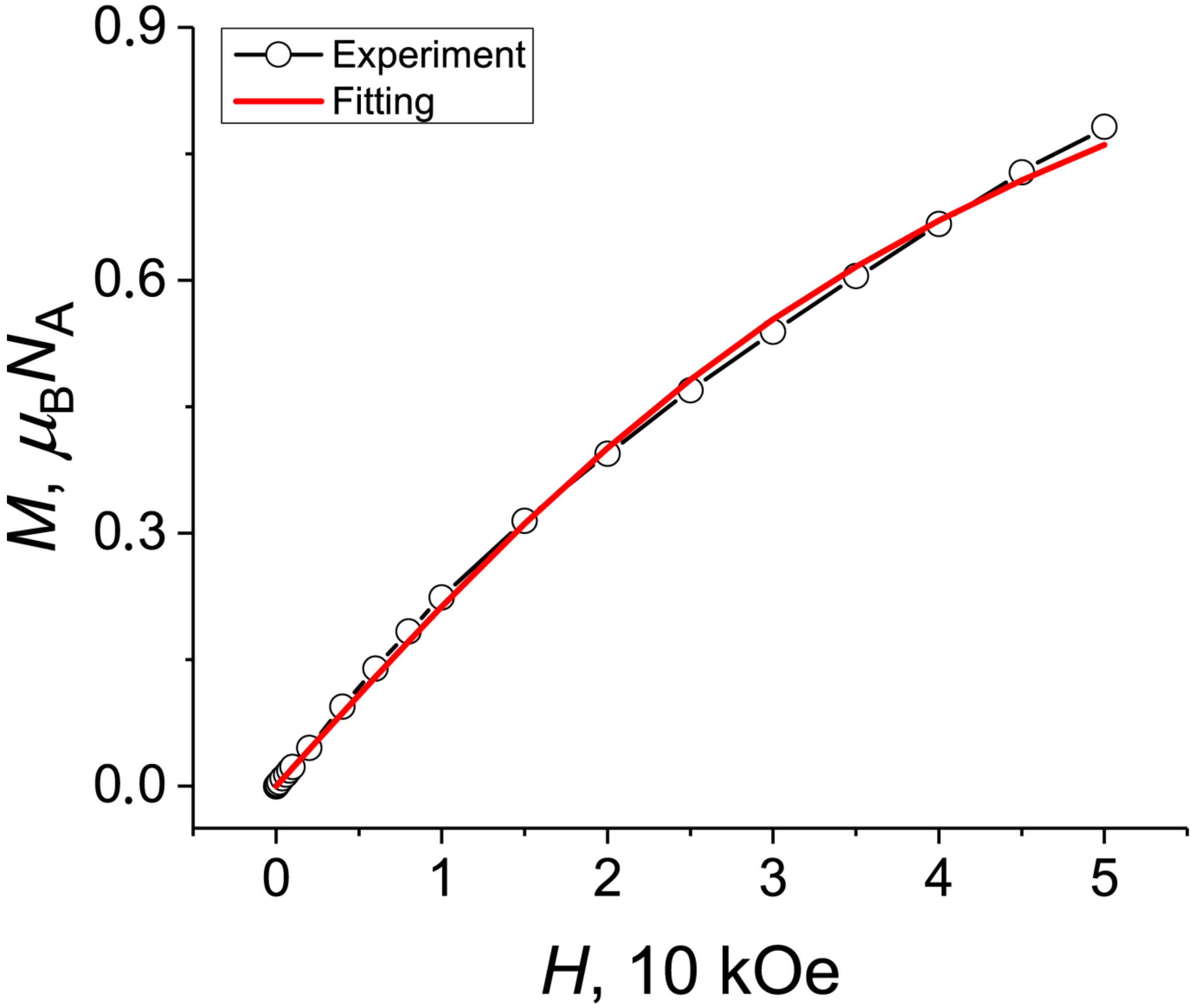

Figure S44. Dependence of magnetization of polycrystalline **10** *vs.* magnetic field (open circles) up to 50 kOe magnetic field at 2 K and and fitting of the data by PHI[7] (red curve) with the same parameters as was used for the fitting of temperature dependence of molar magnetic susceptibility (Fig. 8c in the manuscript).

Complex **11**

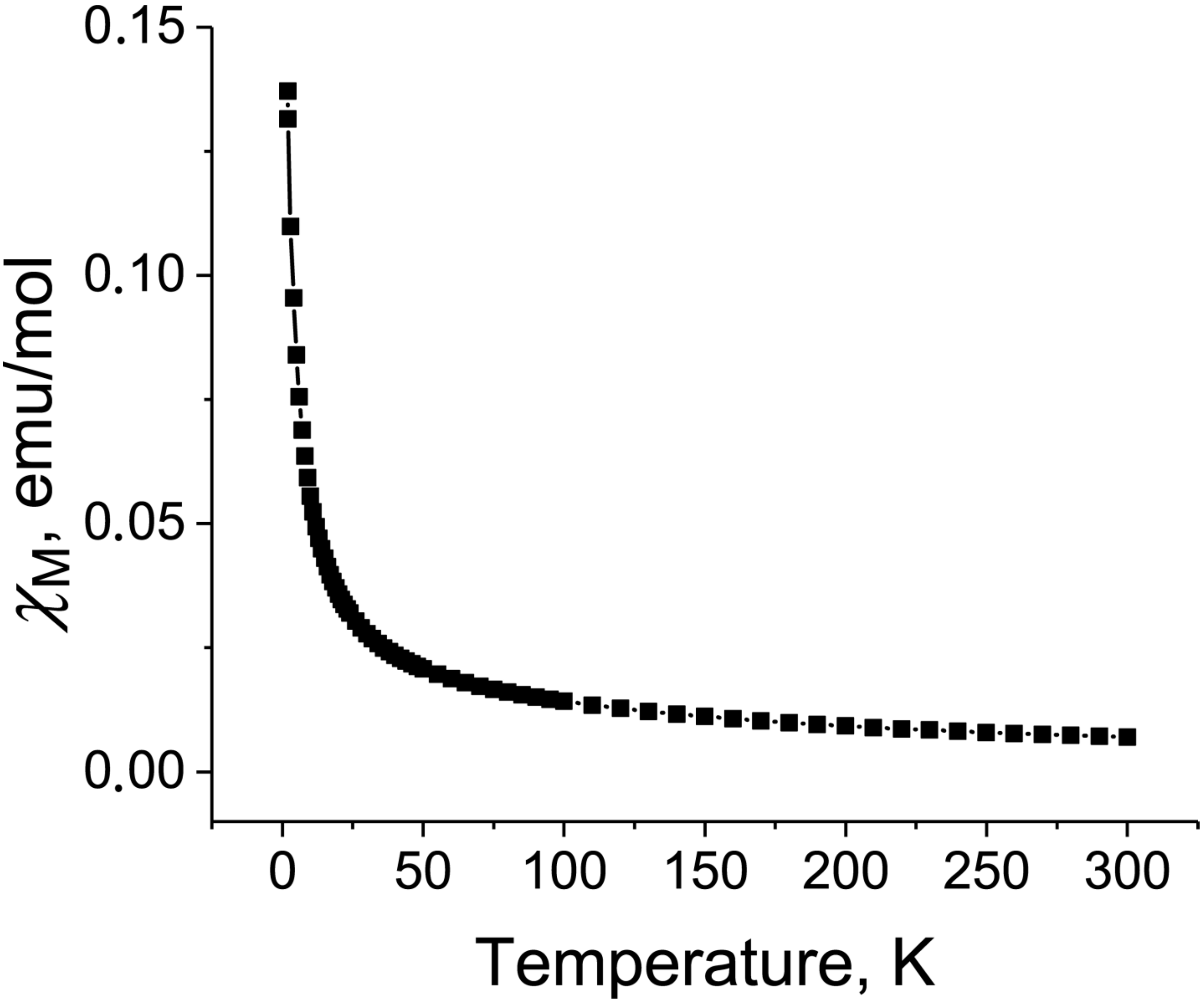

Figure S45. Temperature dependence for molar magnetic susceptibility of polycrystalline $\{(K^+)(crypt)\}_3\{(Co^{II}I_2\}_3(HATNA)\}^{3-}\cdot 3C_6H_4Cl_2\cdot 3C_6H_{14}$ (**11**) in the 1.9-300 K range after the subtraction of temperature independent contribution.

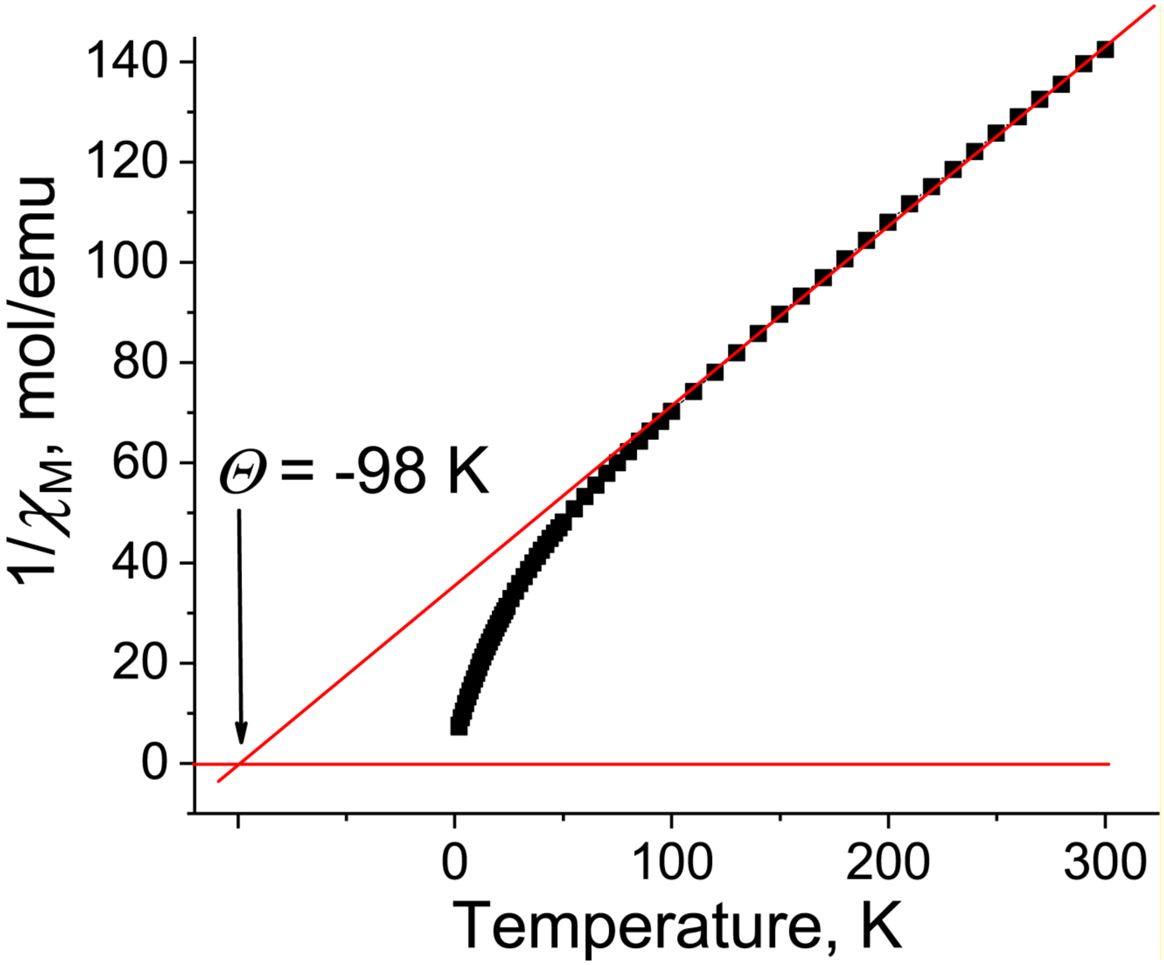

Figure S46. Temperature dependence of reciprocal molar magnetic susceptibility and approximation of the data by the Curie-Weiss law with Weiss temperature (*Θ*) of -98 K for polycrystalline **11** in the 1.9-300 K range.

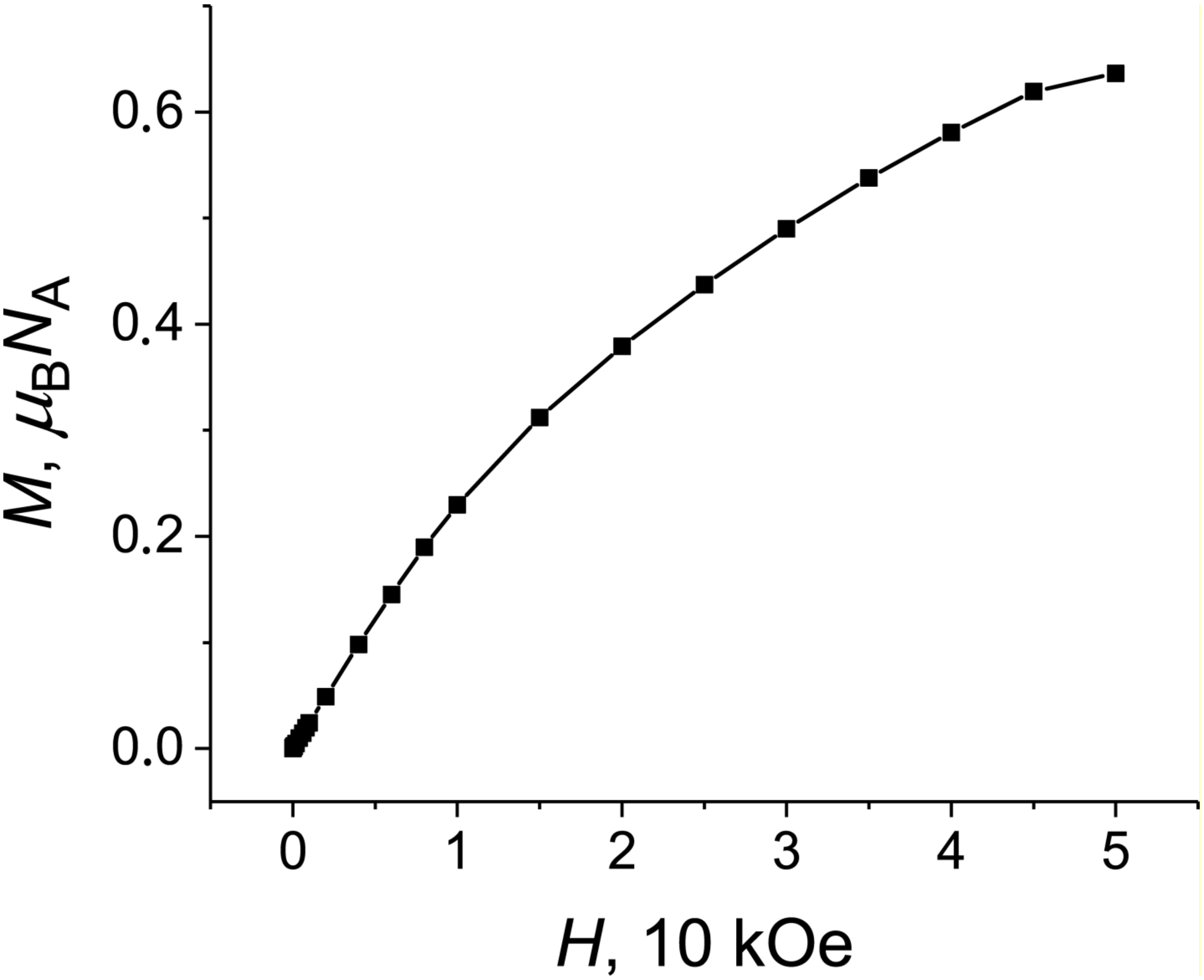

Figure S47. Dependence of magnetization of polycrystalline **11** *vs.* magnetic field up to 50 kOe at 2 K (black line is a guide to the eye).

Table S5. Magneto-structural data of known Fe^{II}, Co^{II} and Mn^{II} complexes based on HATNA, HATA, $HAT(CN)_6$ and $HATNA(CN)_6$.

Coordination units	Charge	HAT-ligand spin	M^{II}-N bond length, Å	Exchange interactions, cm^{-1}	Ref.
$[\{Mn^{II}(dedtc)_2\}_3(HATNA)]^{2-}$	2–	0	2.252(3)	$J = -1.98$	8
$\{(Mn^{II}Cl_2)_3(HATA)\}^{2-}$	2–	0	2.160(4)	$J = -2.7$	8
$\{(Mn^{II}I_2\}_3(HATNA)\}^{3-}$	3–	1/2	2.110(4)	$J_1 = -6.6$, $J_2 = -0.6$	8
$\{(Fe^{II}Cl_2)_3(HATNA)\}^{2-}$	2–	0	2.05(2)–2.14(2)	$J = -4.6$	9
$\{(Fe^{II}Cl_2)_3(HATA)\}^{2-}$	2–	0	2.106(4)	$J = -4.7$	10
$\{(Fe^{II}Cl_2)_3(HAT(CN)_6)\}^{3-}$	3–	1/2	2.092(4)	$J_1 = -164$, $J_2 = -15.4$	10
$\{(Fe^{II}I_2\}_3(HATNA(CN)_6)\}^{3-}$	3–	1/2	2.074(6)	$J_1 = -82.1$, $J_2 = -7$	11
$[\{Co^{II}(hfac)_2\}_2(HATNA)]^0$	0	0	2.178(2)	$J = -0.1$	12
$[Co^{II}\{N(SiMe_3)_2\}_2]_3(HATNA)]^0$	0	0	2.094	$J = -4.4$	13
$[Co^{II}\{N(SiMe_3)_2\}_2]_3(HATNA)]^-$	1–	1/2	2.099	$J_1 = -290$, $J_2 = -5$	13
$\{(Co^{II}I_2\}_3(HATNA(CN)_6)\}^{3-}$	3–	1/2	1.996(13)	$J_1 = -442$, $J_2 = -100$	11
$\{(Co^{II}Cl_2)_3(HAT(CN)_6)\}^{3-}$	3–	1/2	2.02(2)	$J_1 = -349$, $J_2 = -84$	11

Computational details

All calculations were carried out using ORCA rev. 5.0.4 program.[14] The geometries of complexes **1**, **2**, **5** and **8** were taken from the X-ray crystal structure data. Positions of hydrogen atoms were optimized at DFT level theory using the BP86[15] functional, while the positions of the other atoms were frozen according to the crystal structure data. Coordinate system orientations for complexes are shown in Fig. S48. All calculations were performed in conductive media taken into account in CPCM model ($\varepsilon = \infty$).

In all calculations, the relativistically reduced Karlsruhe basis set DKH-def2-TZVP[16] was used for all elements except iodine, for which the basis set SARC-DKH-TZVP was used.[17] The RIJK accelerating approximation was used in combination with the segmented all-electron relativistically contracted auxiliary Coulomb fitting basis SARC/J.[18,19] The RIJCOSX approximation[20] in combination with AUTOAUX auxiliary basis[21] was used to accelerate DFT HF exchange functionals and *ab initio* calculations. Scalar relativistic effects were taken into account through the second-order Douglas-Kroll-Hess (DKH2) Hamiltonian.[22]

Single-point DFT broken symmetry (BS) calculations were performed using various methods: GGA (BP86)[23], PBE[24], TPSS[25] and hybrid functionals with different HF exchange (TPSSh), B3LYP/G[26], B3LYP[27], B1LYP[28], PBE0[29], REVPBE38[30] (Tables S6-S8).

The multi-reference *ab initio* complete active space self-consistent field calculations (CASSCF) were performed for all the complexes under study. The following parameters of the state-averaged CASSCF (SA-CASSCF) calculations were used: seven electrons on five active orbitals (CASSCF(7,5)) for 10 quartet and 40 doublet roots for mononuclear complex **1**; fifteen electrons on eleven active orbitals (CASSCF(15,11)) for 50 octet, 50 sextet, 50 quartet and 50 doublet roots for binuclear complexes **2** and **5**; fourteen electrons on eleven active orbitals (CASSCF(14,11)) for 50 nonet, 50 septet, 50 quintet, 50 triplet and 50 singlet roots for binuclear complex **8**.

The second-order N-electron valence perturbation theory (NEVPT2) calculations were used to improve the excitation energies by accounting for dynamical correlation.[31] SA-CASSCF/NEVPT2 calculations were performed on SA-CASSCF wavefunctions. The following states were chosen for NEVPT2 calculation: all 10 quartet and 40 doublet roots for mononuclear complex **1**; lowest 5 octet, 10 sextet, 10 quartet and 10 doublet roots for binuclear complexes **2** and **5**; lowest 4 nonet, 4 septet, 4 quintet, 4 triplet and 4 singlet roots for binuclear complex **8**. All roots were taken with the equal weights.

The local magnetic properties (the axial zero field splitting (ZFS) parameters (D), rhombicity ratio in the ZFS (E/D), g-factor) of all the complexes under study were obtained from SA-CASSCF/NEVPT2 calculations according to quasi-degenerate perturbation theory (QDPT)[32], which used an approximation to the Breit-Pauli form of the spin-orbit coupling operator (SOMF(1X) approximation).[33] Splitting of the d-orbitals was analyzed within the *ab initio* ligand field theory (AILFT).[34,35]

For mononuclear complex **1,** the dependence $\chi_M T$ was obtained using the SINGLE_ANISO module in ORCA (Fig. S59).

For binuclear complexes **2**, **5** and **8**, additional calculations were carried out for auxiliary mononuclear paramagnetic fragments, where one of the paramagnetic ions was replaced by diamagnetic ion Zn(II). Seven electrons on five active d-orbitals were used in SA-CASSCF calculation for Co(II) mononuclear paramagnetic fragment, all 10 quartet and 40 doublet roots were taken with equal weights. Six electrons on five active d-orbitals were used in SA-CASSCF calculation for Fe(II) mononuclear paramagnetic fragment, all 5 quintet, 45 triplet and 50 singlet roots were taken with the equal weights. POLY_ANISO module was used to obtain the dependences $\chi_M T$ on the basis of the calculated local magnetic properties of auxiliary mononuclear paramagnetic fragments (Fig. S59).

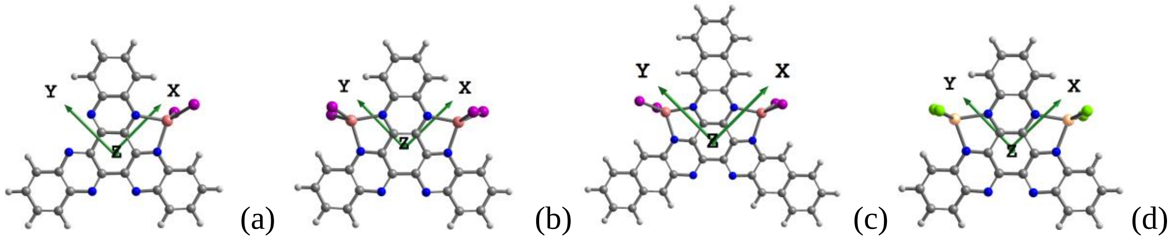

(a) (b) (c) (d)

Fig. S48. Coordinate system orientation for complexes **1** (a), **2** (b), **5** (c) and **8** (d).

For complex **1**, the calculations confirmed HS state (S = 3/2) of Co ion. The calculated $\chi_M T$ dependence (Fig. S59a) is in a good agreement with the experimental one at temperatures higher than 150 K, and at room temperature the calculated and experimental $\chi_M T$ are practically equal (experimental 2.87 vs. calculated 2.82 emu·K/mol at 300 K). However, at lower temperatures the calculated $\chi_M T$ values were higher than the experimental ones. It can be related to small antiferromagnetic intermolecular exchange coupling in the π-stacked chains of **1**. The calculated average D value was -12.71 cm^{-1}, E/D value was approximately 0.33, and g = 2.34 (g_x = 2.24, g_y = 2.33, g_z = 2.46) (Table S11).

For complexes **2** and **5**, the calculations indicated HS S_T = 5/2 ground states with ferromagnetic interaction between high-spin (S = 3/2) Co ions and antiferromagnetic interaction between the ligand (S = 1/2) and both Co ions. The calculated local magnetic properties are very close for both complexes. For complex **2**, the calculated average D value was -15.65 cm^{-1}, E/D value was approximately 0.19, and g = 2.26 (g_x = 2.05, g_y = 2.19, g_z = 2.55) (Table S11). For complex **5**, the calculated average D value was -14.62 cm^{-1}, E/D value was approximately 0.17, and g = 2.27 (g_x = 2.08, g_y = 2.17, g_z = 2.55). The calculations revealed strongly antiferromagnetic interaction between Co centers and ligand radical with the magnetic exchange values -627.2 and -611.3 cm^{-1} for complexes **2** and **5**, respectively (Table S9). The calculated magnetic exchange values for complexes **2** and **5** resulted in close $\chi_M T$ dependences, while their experimental dependencies are rather different. The experimental $\chi_M T$ of complexes **2** and **5** are close at room temperature, and $\chi_M T$ (Fig. S59b,c) of complex **5** is much less than that of complex **2** at low temperatures. Clearly, it indicates the presence of significant antiferromagnetic intermolecular exchange interaction within the π-stacked spirals of **5** (see Crystal structure segment).

For complex **8**, the calculations indicated $S_T = 0$ ground state with the antiferromagnetic coupling between high-spin ($S = 2$) Fe ions with the magnetic exchange value of -3.0 cm^{-1}. This magnetic exchange value resulted in $\chi_M T$ (Fig. S59d) dependence is very close to the experimental one.

It can be seen from Figures S50, S54 and S51, S55 as well as from *ab initio* ligand field analysis Figure S57, that the unpaired electrons in complexes **2** and **5** are located at dxy, dz^2 and dxz/dyz (Co$_1$/Co$_2$) orbitals. The only orbital providing overlap with the ligand's π system is dxz/dyz and thus mixing of the dxz/dyz orbital and π orbital of the ligand induces an efficient spin density delocalization in the high-spin dicobalt complexes **2** and **5** which causes strong magnetic exchange.

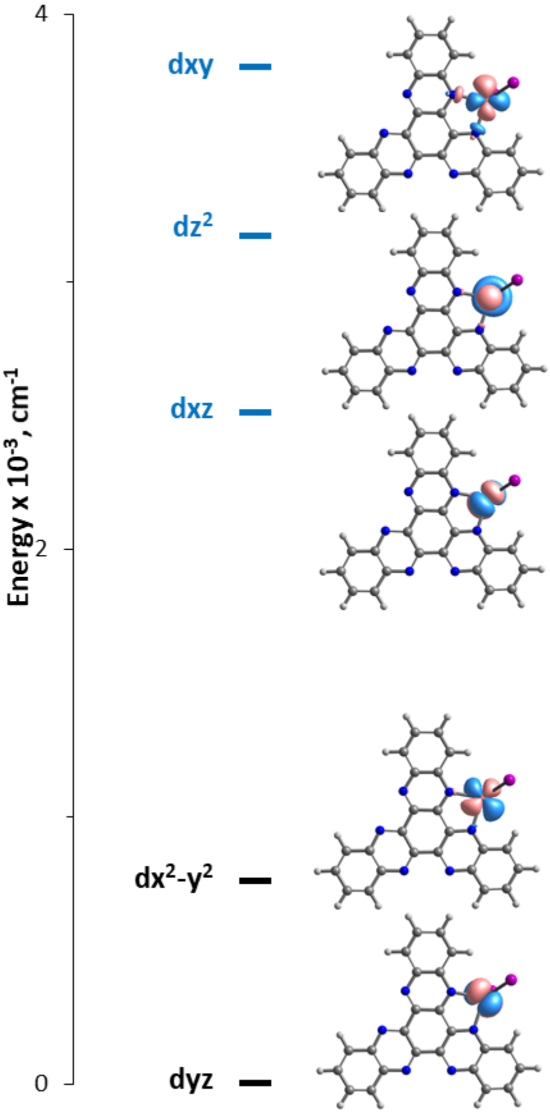

Fig. S49. The orbital energies diagram from SA-CASSCF(7,5)/NEVPT2 of complex **1** (black line – double occupied molecular orbital of Co, blue line– single occupied molecular orbital of Co).

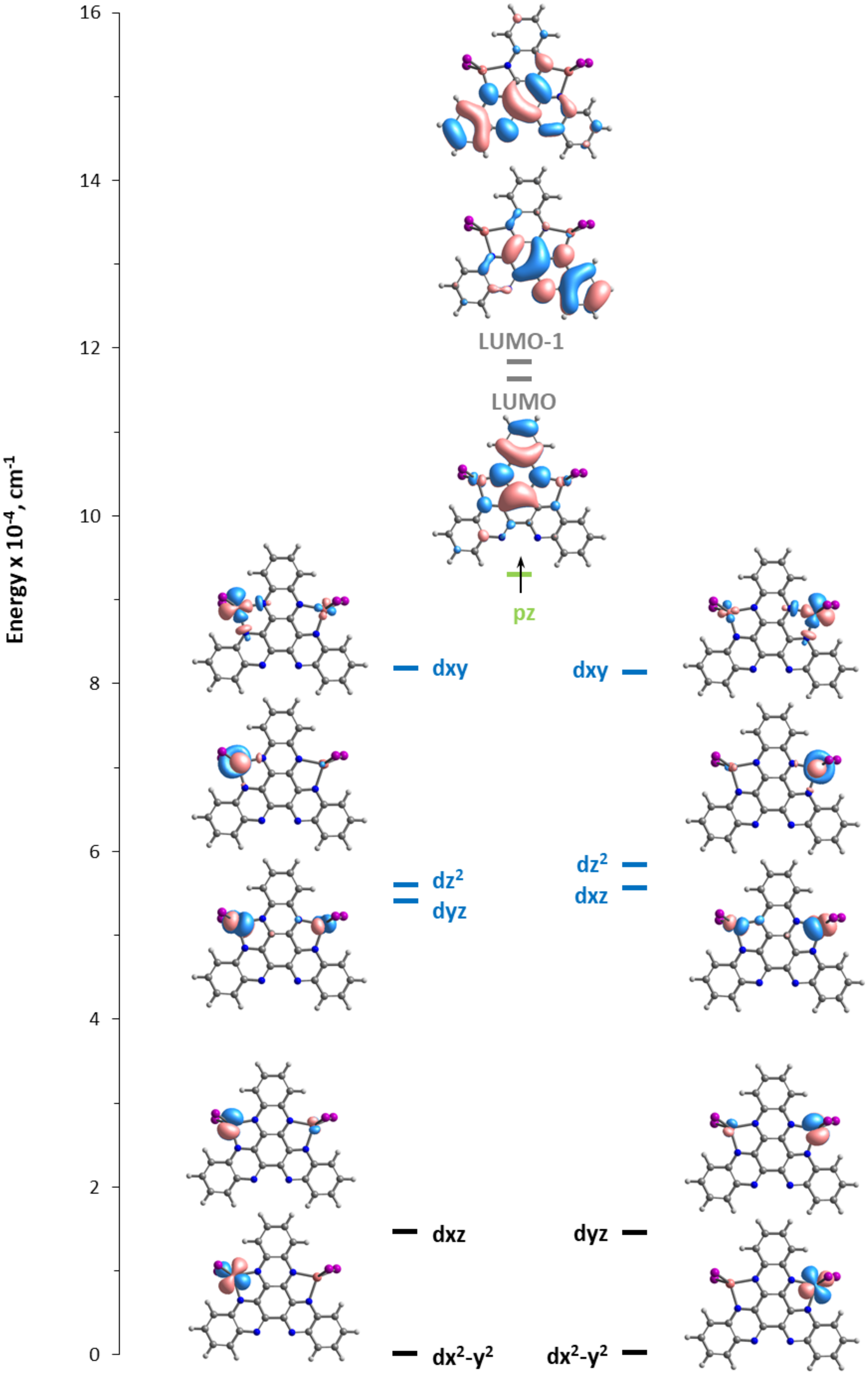

Fig. S50. The orbital energies diagram from SA-CASSCF(15,11)/NEVPT2 of complex **2** (Co$_1$ (right), Co$_2$ (left), black line – double occupied molecular orbital of Co, blue line– single occupied molecular orbital of Co, green line – single occupied molecular orbital of ligand, grey line – low-lying LUMO orbital).

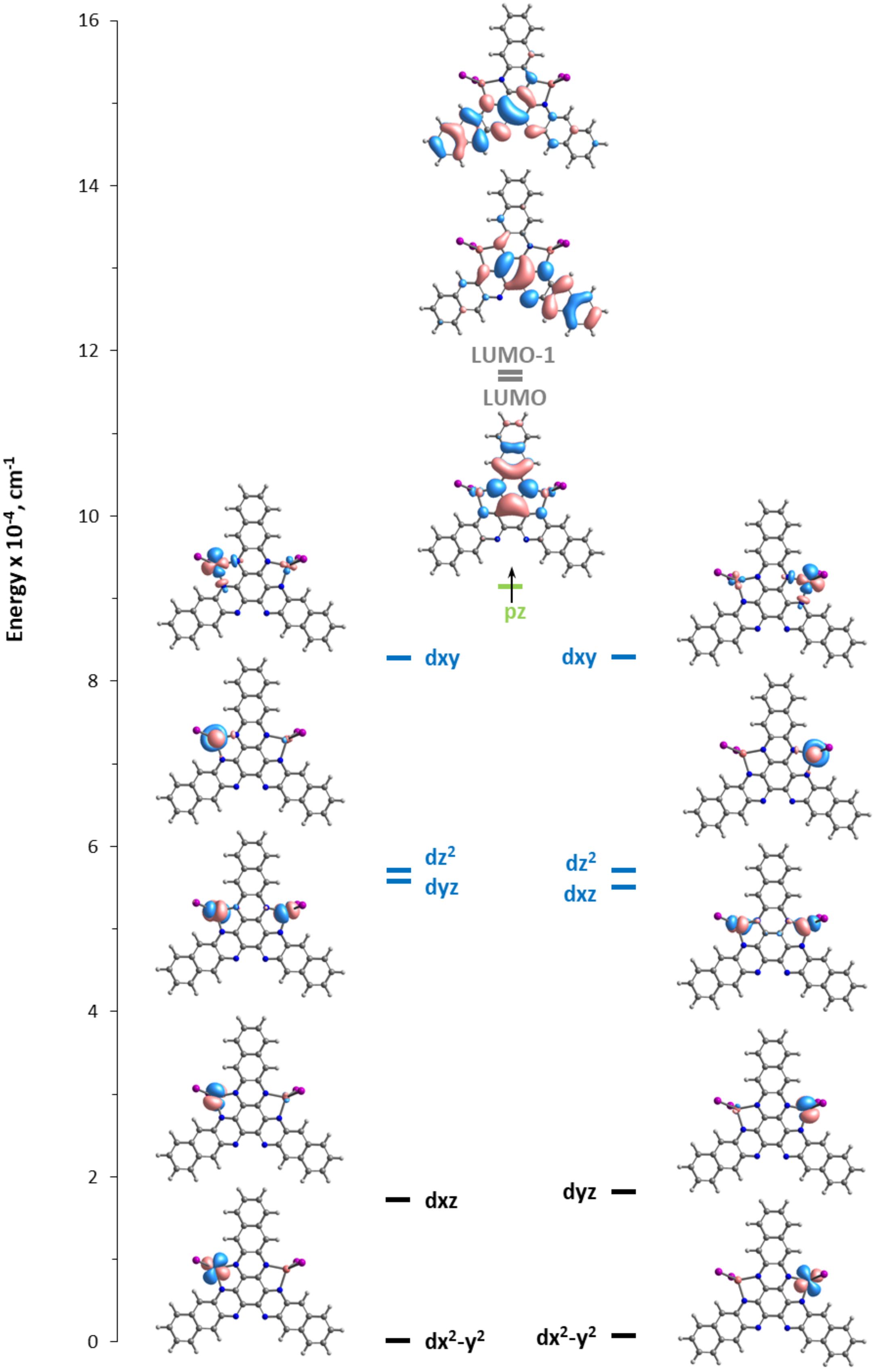

Fig. S51. The orbital energies diagram from SA-CASSCF(15,11)/NEVPT2 of complex **5** (Co_1 (right), Co_2 (left), black line – double occupied molecular orbital of Co, blue lines – single occupied molecular orbital of Co, green line – single occupied molecular orbital of ligand, grey line – low-lying LUMO orbital).

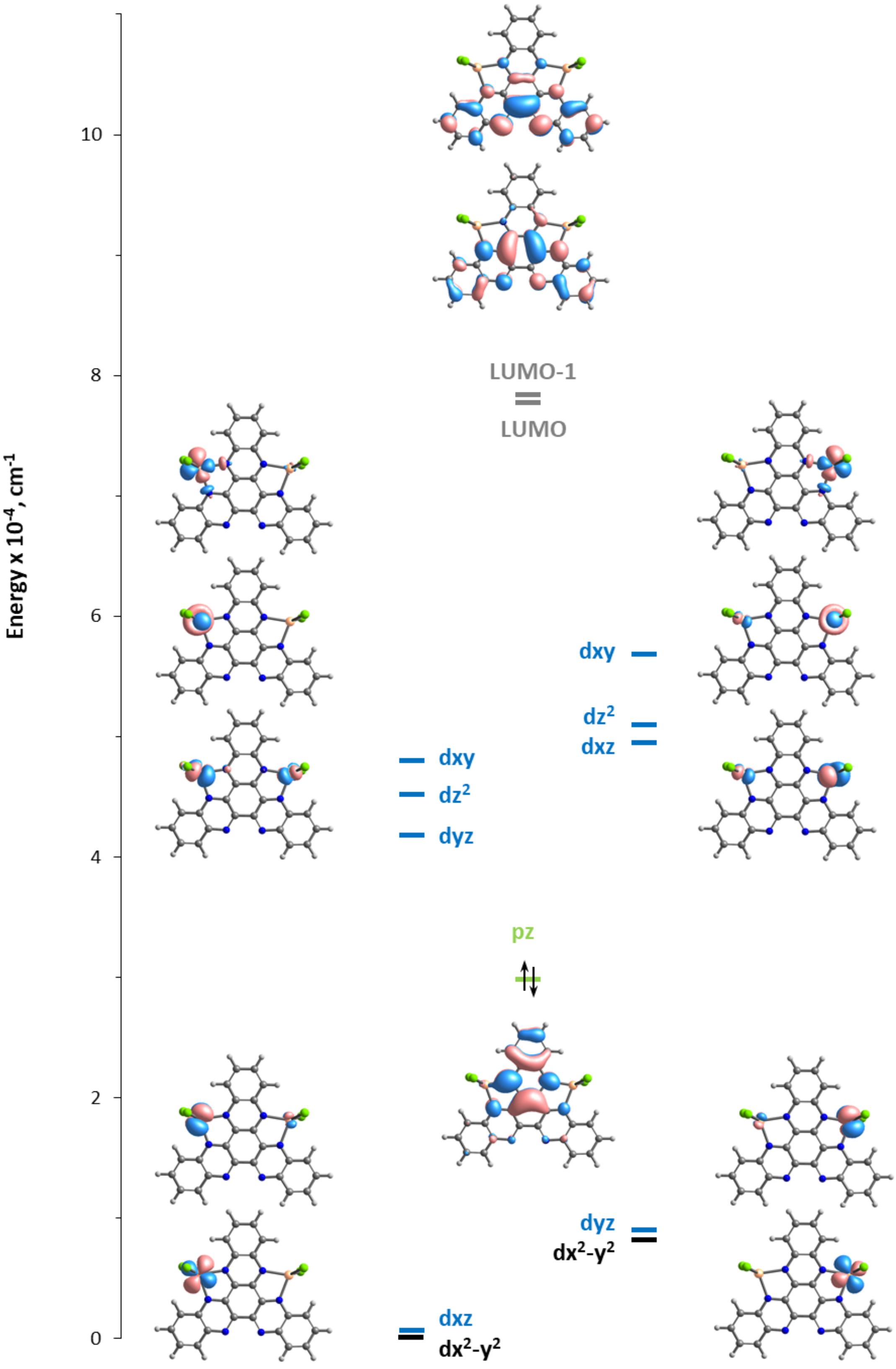

Fig. S52. The orbital energies diagram from SA-CASSCF(14,11)/NEVPT2 of complex **8** (Fe$_1$ (right), Fe$_2$ (left), black line – double occupied molecular orbital of Fe, blue line– single occupied molecular orbital of Fe, green lines – double occupied molecular orbital of ligand, grey line – low-lying LUMO orbital).

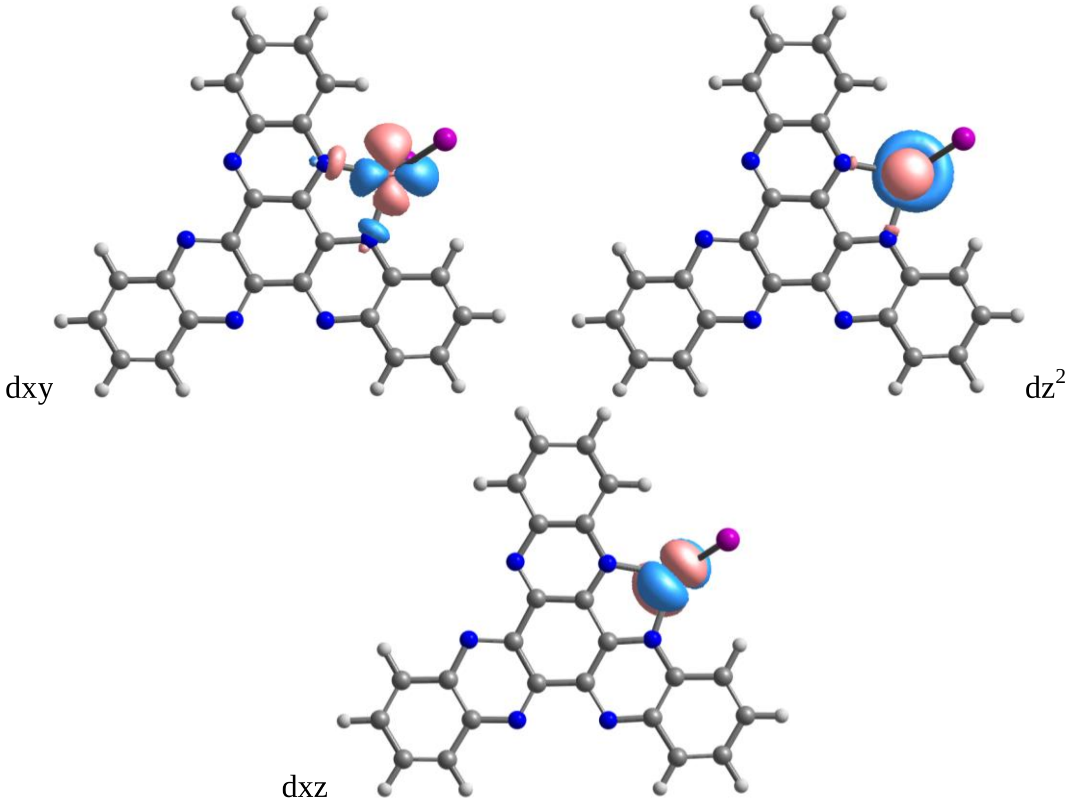

Fig. S53. The SOMO orbitals Co of complex **1** with uncharged ligand from SA-CASSCF(7,5)/NEVPT2.

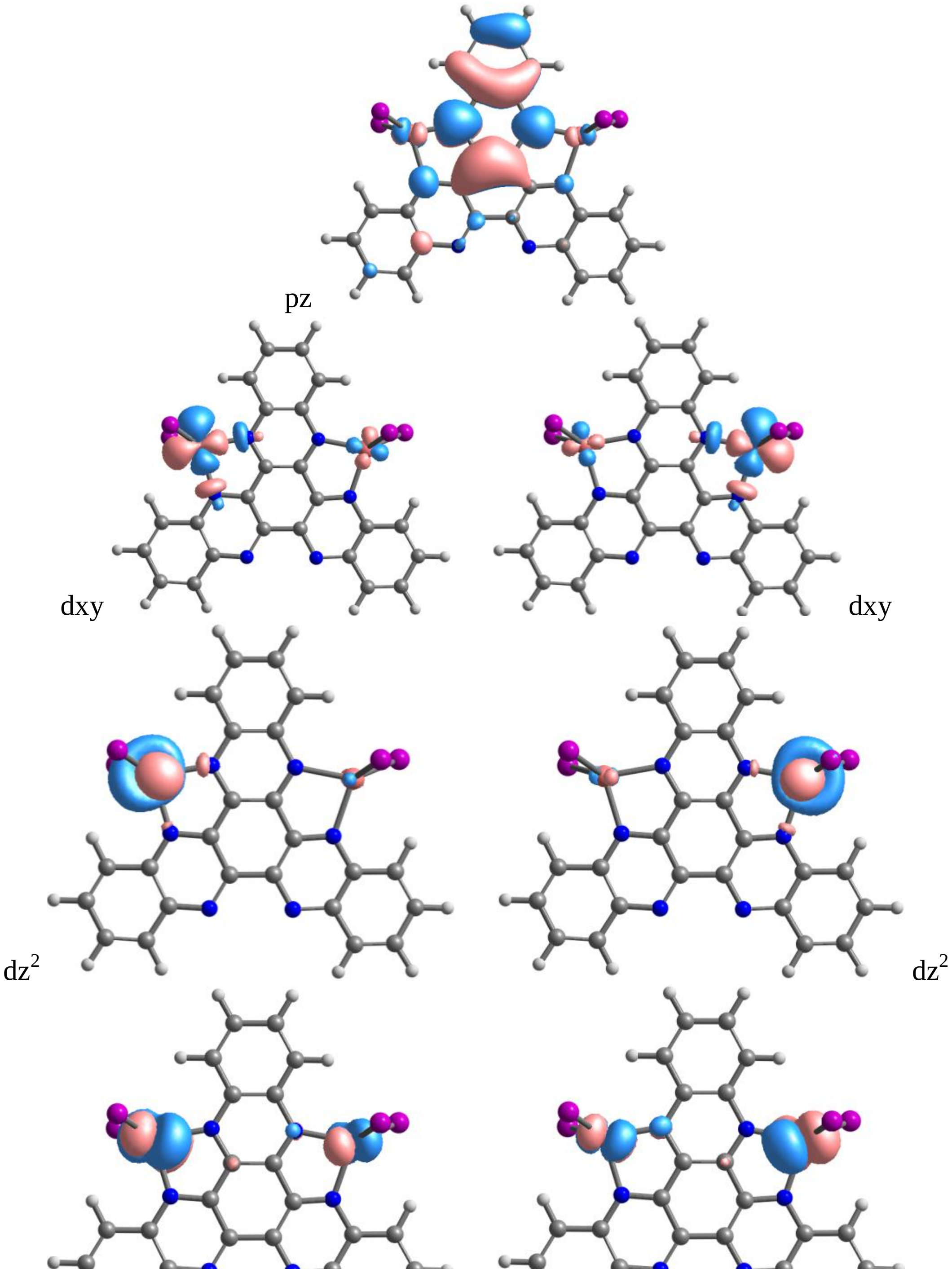

Fig. S54. The SOMO orbitals Co$_1$ (right), Co$_2$ (left) and SOMO ligand of complex **2** with charged (-1) ligand from SA-CASSCF(15,11)/NEVPT2.

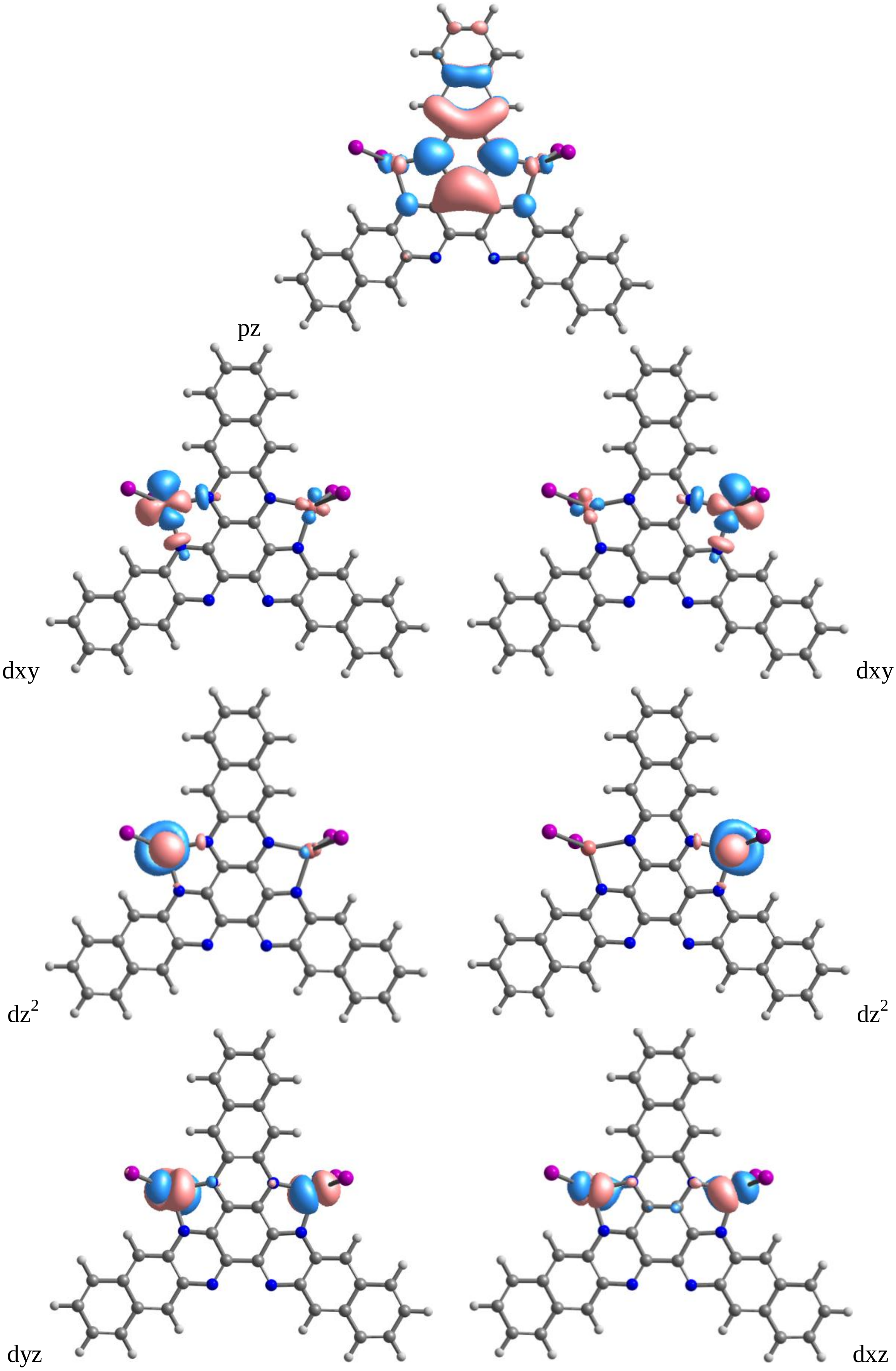

Fig. S55. The SOMO orbitals Co$_1$ (right), Co$_2$ (left) and SOMO ligand of complex **5** with charged (-1) ligand from SA-CASSCF(15,11)/NEVPT2.

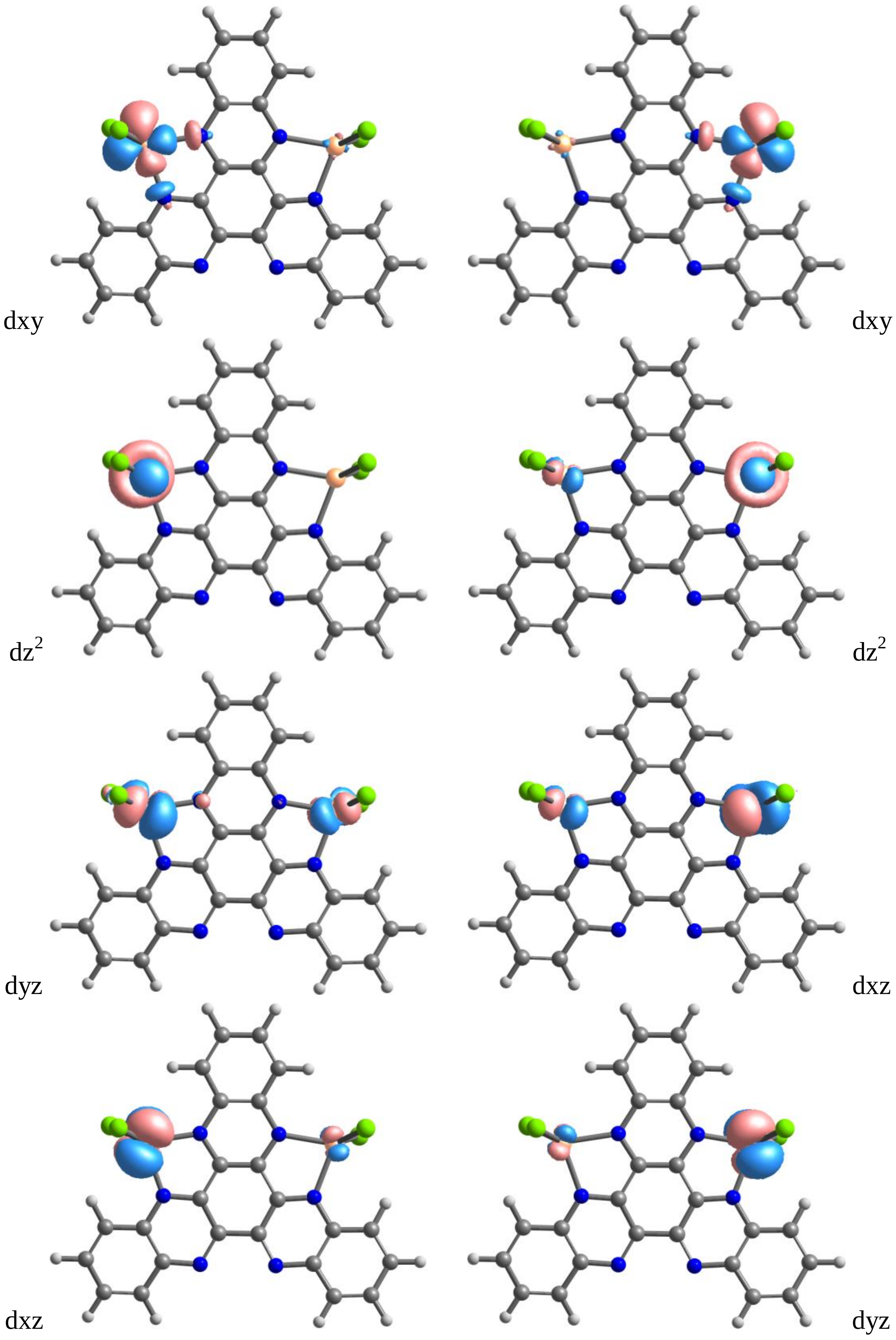

Fig. S56. The SOMO orbitals Fe$_1$ (right), Fe$_2$ (left) of complex **8** with charged (-2) diamagnetic ligand from SA-CASSCF(14,11)/NEVPT2.

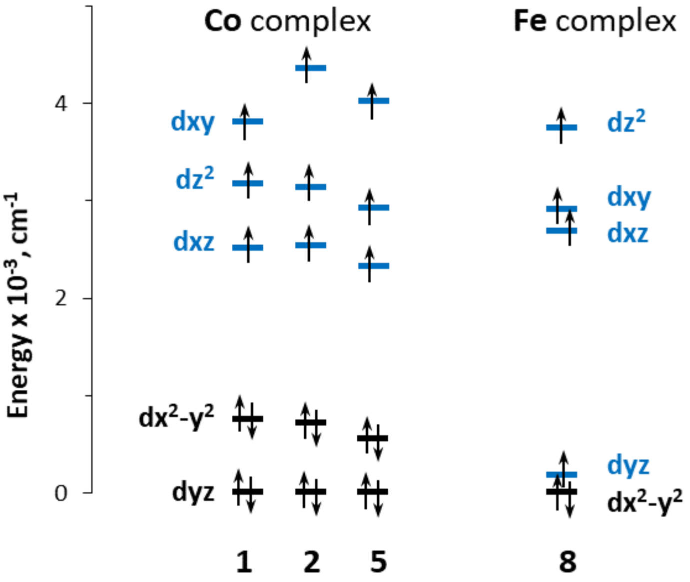

Fig. S57. Ligand field splitting for the Co/Fe metal sites in complexes **1** (neutral ligand), **2** (charged ligand (-1), **5** (charged ligand (-1), **8** (charged diamagnetic ligand (-2) obtained from SA-CASSCF/NEVPT2 calculations.

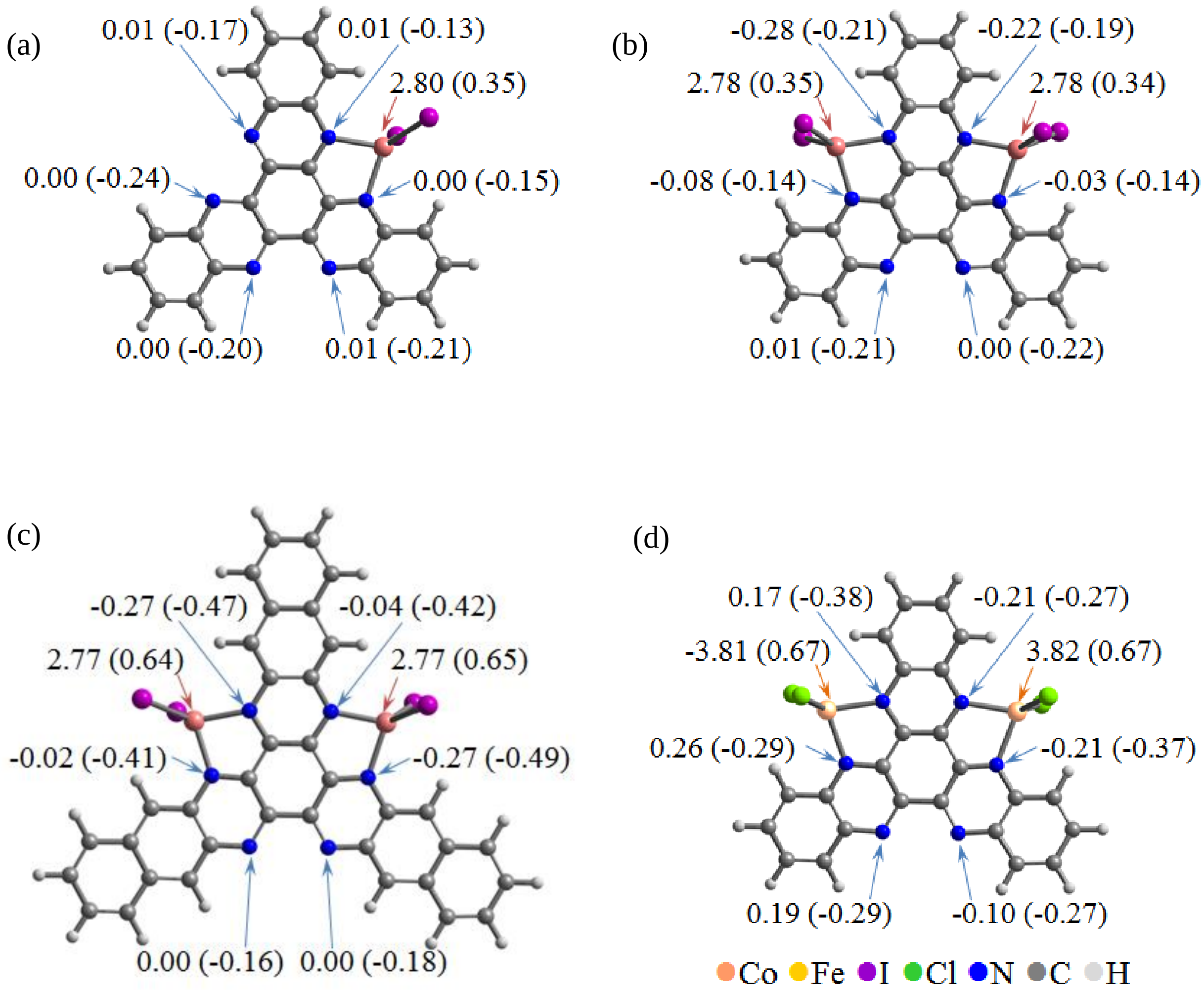

Fig. S58. The Mulliken spin densities and charges (in brackets) on selected atoms of complex **1** (a), **2** (b), **5** (c) and **8** (d) for RevPBE38 DFT functional.

Table S6. Spin expectation and exchange-coupling values from DFT BS calculation for complex **2.**

Functional	%HF	S^2_{UUU}	S^2_{UDU}	S^2_{UUD}	$\boldsymbol{J}_1$(M-L)
BP86	0	15.7799	9.1313	3.1886	**-651.5**
PBE	0	15.7818	9.1368	3.1943	**-646.4**
TPSS	0	15.7729	9.1954	3.2819	**-816.8**
TPSSh	10	15.7778	9.4117	3.5053	**-763.1**
B3LYP/G	15	15.7831	9.4949	3.574	**-752.5**
B3LYP	20	15.7834	9.4968	3.5757	**-750.0**
B1LYP	25	15.7862	9.5593	3.2994	**-712.9**
PBE0	25	15.7875	9.5719	3.5053	**-684.6**
REVPBE38	37.5	15.8014	9.6705	3.5764	**-667.8**

Table S7. Spin expectation and exchange-coupling values from DFT BS calculation for complex **5.**

Functional	%HF	S^2_{UUU}	S^2_{UDU}	S^2_{UUD}	$\boldsymbol{J}_1$(M-L)
BP86	0	15.7796	9.1697	3.2507	**-542.6**
PBE	0	15.7849	9.1743	3.2554	**-622.5**
TPSS	0	15.7743	9.2311		**-713.6**
TPSSh	10	15.7793	9.4421	3.5630	**-697.7**
B3LYP/G	15	15.7843	9.5236		**-700.7**
B3LYP	20	15.7846	9.5253	3.6252	**-698.0**
B1LYP	25	15.7822	9.5194	3.6612	-784.3
PBE0	25	15.7892	9.3939	3.672	**-925.9**
REVPBE38	37.5	15.8007	9.6785	3.7347	**-585.6**

Table S8. Spin expectation and exchange-coupling values from DFT BS calculation for complex **8.**

Functional	%HF	S^2_{UU}	S^2_{UD}	$\boldsymbol{J}_2$(M-M)
BP86	0	20.1255	4.1022	**-40.6**
PBE	0	20.1497	4.1214	**-36.6**
TPSS	0	20.0692	4.0962	**-48.4**
TPSSh	10	20.1285	4.2611	**-47.7**

B3LYP/G	15	20.2491	4.3629	**-49.5**
B3LYP	20	20.2535	4.3654	**-49.3**
B1LYP	25	20.3996	4.4431	**-48.3**
PBE0	25	20.4136	4.4575	**-46.5**
REVPBE38	37.5	20.6621	4.6335	**-53.6**

Table S9. Exchange-coupling values from SA-CASSCF/NEVPT2 calculation for complexes **2**, **5** and **8.**

Complex	**2**	**5**	**8**
	J_1(M-L)	J_1(M-L)	J_2(M-M)
J	-627.2	-611.3	-3.0

Table S10. Spin density from DFT BS Mulliken spin population analysis.

Complex	Unpaired electrons	Spin population Co/Fe site		% delocalization to ligand	
		B3LYP	RevPBE38	B3LYP	RevPBE38
1	3	2.63	2.80	12.3	6.5
2	3	2.58	2.78	14.0	7.2
5	3	2.63	2.77	12.3	7.8
8	4	3.66	3.82	8.5	4.6

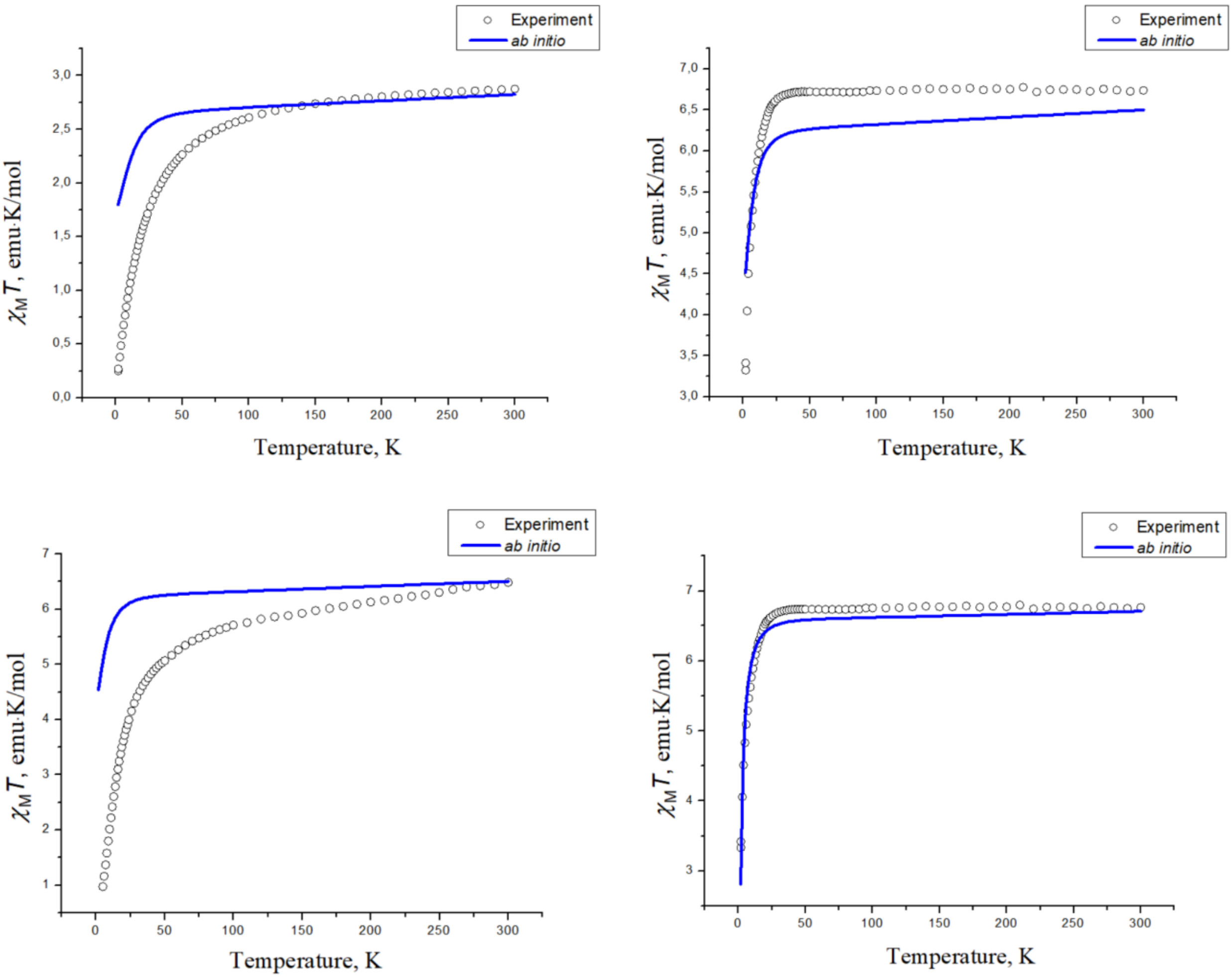

Fig. S59. $\chi_M T$ dependences for complexes **1** (a), **2** (b), **5** (c) and **8** (d): experimental and theoretical (constructed using the data obtained by SA-CASSCF/NEVPT2 method).

Table S11. ZFS parameters and *g*-tensor value from SA-CASSCF/NEVPT2 calculation for complexes **1**, **2**, **5.**

Complex	**1**	**2**	**5**
Parameters			
D, cm^{-1}	-12.71	-15.65	-14.62
E/*D*	0.33	0.19	0.17
g_x	2.24	2.05	2.08
g_y	2.33	2.19	2.17
g_z	2.46	2.55	2.55

The exchange coupling constant calculations details

The magnetic exchange interaction was described by the Heisenberg spin Hamiltonian, which has the following form for three magnetic centers like Me_1-ligand-Me_2 (Me is Co(II) or Fe(II) metal atoms):

$$\hat{H} = -2J_1 S_{\mathrm{Me}_1} S_{\mathrm{L}} - 2J_1 S_{\mathrm{Me}_2} S_{\mathrm{L}} - 2J_2 S_{\mathrm{Me}_1} S_{\mathrm{Me}_2} \qquad (1)$$

Here J_1 is the exchange coupling constant between Me (Me_1 or Me_2) and the ligand, J_2 is the exchange coupling constant between two Me atoms, and S_{Me1}, S_{Me2} and S_L are spins on Me_1, Me_2 and ligand magnetic centers, respectively.

In the case of two magnetic centers *a* and *b*, the Yamaguchi's approximate spin projection procedure (AP) [36] results in the following expression:

$$J_{ab}^{(\mathrm{AP})} = -\frac{E_{\mathrm{HS}} - E_{\mathrm{LS}}}{\langle S^2 \rangle_{\mathrm{HS}} - \langle S^2 \rangle_{\mathrm{LS}}} \qquad (2)$$

E_{HS} and $<S^2>_{HS}$ and E_{LS} and $<S^2>_{LS}$ are the energy and the expectation values of the squared spin operator for high-spin and low-spin states, respectively. The generalization of AP approach to multispin systems was done in Ref [37].

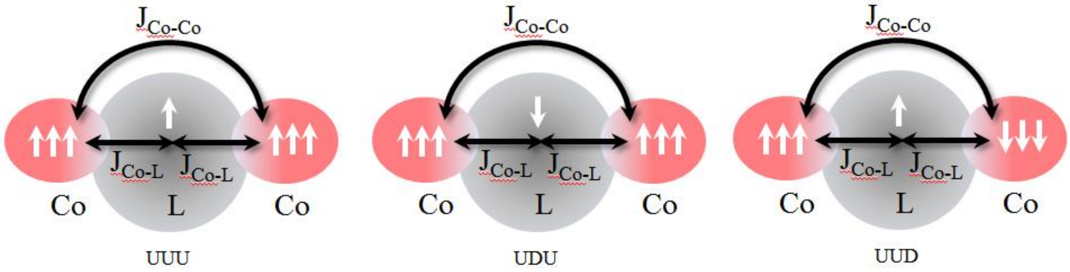

Fig. S60. Calculated solutions for Co(II)-ligand-Co(II) systems: UUU - all spin up ($S_{Co1} = 3/2$, $S_L = 1/2$, $S_{Co2} = 3/2$); UDU – spin down only on ligand ($S_{Co1} = 3/2$, $S_L = -1/2$, $S_{Co2} = 3/2$); UUU – spin down only on one of metals ($S_{Co1} = 3/2$, $S_L = 1/2$, $S_{Co2} = -3/2$).

In the case of a three-spins system like Co(II)-ligand-Co(II) (complexes **2**, **5**), three solutions with different spins orientations were used for calculation metal-ligand and metal-metal coupling constants. These solutions are "UDU", "UUU" and "UUD", where U (up) and D (down) denote the spin orientation at the Co(II)-ligand-Co(II) magnetic centers (see Fig.S60). Both BS-DFT and SA-CASSCF calculations yielded the "UDU" solution as the ground state. For BS-DFT calculations, Eq.(2) results in the following expression for metal-ligand $J_{\text{Co-L}}$ exchange coupling constant in Co(II)-ligand-Co(II) systems:

$$J_{\text{Co-L}} = -\frac{E_{\text{UUU}}-E_{\text{UDU}}}{\langle S^2\rangle_{\text{UUU}}-\langle S^2\rangle_{\text{UDU}}} \tag{3}$$

The generalization of AP approach to multispin systems [37] results in the following expression for metal-metal $J_{\text{Co-Co}}$ exchange coupling constant in Co(II)-ligand-Co(II) systems:

$$J_{\text{Co-Co}} = -\frac{\frac{1}{2}(E_{\text{UUU}}+E_{\text{UDU}})-E_{\text{UUD}}}{\frac{1}{2}(\langle S^2\rangle_{\text{UUU}}+\langle S^2\rangle_{\text{UDU}})-\langle S^2\rangle_{\text{UUD}}} \tag{4}$$

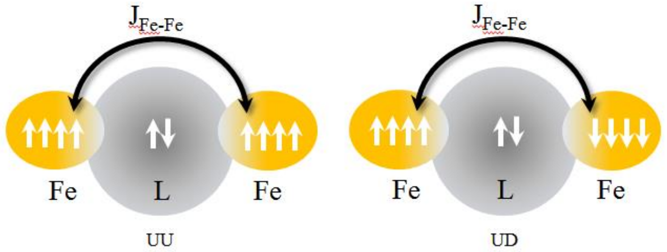

Fig. S61. Calculated solutions for Fe(II)-ligand-Fe(II) system: UU – ferromagnetic spins orientation on Fe atoms (S_{Fe1} = 2, S_{Fe2} = 2); UD – antiferromagnetic spins orientation on Fe atoms (S_{Fe1} = 2, S_{Fe2} = -2).

For CASSCF calculations, $J_{\text{Co-L}}$ and $J_{\text{Co-Co}}$ exchange coupling constants were calculated from energies of three solutions: “UDU” (M = 8, S_{Co1} = 3/2, S_{L} = 1/2, S_{Co2} = 3/2), “UUU” (M = 6, S_{Co1} = 3/2, S_{L} = -1/2, S_{Co2} = 3/2) and “UUD” (M = 2, S_{Co1} = 3/2, S_{L} = 1/2, S_{Co2} = -3/2) according to Eq.(1).

The calculated $J_{\text{Co-L}}$ values according to Eq. (3) for complexes **2**, **5** are presented in Table S6, S7. The calculated $J_{\text{Co-Co}}$ values according to Eq. (4) for complexes **2**, **5** vary in wide range (from -50 to -100 cm^{-1}) in BS-DFT calculations demonstrating antiferromagnetic exchange between Co atoms. In SA-CASSCF/NEVPT2 $J_{\text{Co-Co}}$ values for complexes **2**, **5** also demonstrate antiferromagnetic exchange between Co atoms (-21.1 cm^{-1} for **2** complex and -10.5 cm^{-1} for **5** complex).

In the case of Fe(II)-ligand-Fe(II) system with formal diamagnetic ligand (complex **8**), there are two magnetic centers on both Fe atoms. In this case the expression for metal-metal $J_{\text{Fe-Fe}}$ exchange coupling constant for BS-DFT calculations is the following

$$J_{\text{Fe-Fe}} = -\frac{E_{\text{UU}} - E_{\text{UD}}}{\langle S^2 \rangle_{\text{UU}} - \langle S^2 \rangle_{\text{UD}}} \tag{5}$$

E_{UU} and $<S^2>_{\text{UU}}$ and E_{UD} and $<S^2>_{\text{UD}}$ are the energy and the expectation value of the squared spin operator for ferromagnetic (UU) and antiferromagnetic (UD) orientations of spins on Fe atoms (see **Fig. S61**).

For CASSCF calculations, $J_{\text{Fe-Fe}}$ exchange coupling constant was calculated from energies of two solutions: “UU” (M = 9, $S_{\text{Fe1}} = 2$, $S_{\text{Fe2}} = 2$) and “UU” (M = 1, $S_{\text{Fe1}} = 2$, $S_{\text{Fe2}} = -2$) according to Eq.(1).

The calculated $J_{\text{Fe-Fe}}$ values according to Eq. (5) for complex **8** are presented in Table S8.

The best agreement of calculated $J_{\text{Co-L}}$ and $J_{\text{Fe-Fe}}$ values with PHI fitting of experimental data is observed for SA-CASSCF/NEVPT2 calculations.

References

1. S. Skujins, G. A. Webb, *Tetrahedron*, 1969, **25**, 3935–3945.
2. T. Rademacher, K. Kanakarajan, A. W. Czarnik, *Synthesis*, 1994, **4**, 378–380.
3. S. Kitagawa, S. Masaoka, *Coord. Chem. Rev*., 2003, **246**, 73–88.
4. CrysAlisPRO, Oxford Diffraction, Agilent Technologies UK Ltd, Yarnton, England.
5. G. M. Sheldrick, *Acta Crystallogr., Sect. A: Found. Crystallogr*., 2008, **64**, 112–122.
6. L. J. Farrugia, *J. Appl. Cryst*., 2012, **45**, 849–854.
7. N. F. Chilton, R. P. Anderson, L. D. Turner, A. Soncini, K. S. Murray, *J. Comput. Chem*. 2013, **34**, 1164–1175.
8. M.V. Mikhailenko, V.V. Ivanov, M.A. Faraonov, A.V. Kuzmin, S.S. Khasanov, A. Otsuka, H. Yamochi, H. Kitagawa, D.V. Konarev, *New J. Chem.*, 2023, **47**, 22339–22349.
9. D. V. Konarev, S. S. Khasanov, M. V. Mikhailenko, M. S. Batov, A. Otsuka, H. Yamochi, H. Kitagawa, R. N. Lyubovskaya, *Eur. J. Inorg. Chem.*, 2021, 86–92.
10. M. V. Mikhailenko, S. S. Khasanov, A. F. Shestakov, A. V. Kuzmin, A. Otsuka, H. Yamochi, H. Kitagawa, D. V. Konarev, *Chem. – Eur. J.*, 2022, **28**, e202104165.
11. M. V. Mikhailenko, V. V. Ivanov, A. F. Shestakov, A. V. Kuzmin, S. S. Khasanov, A. Otsuka, H. Yamochi, H. Kitagawa, D. V. Konarev, *Dalton Trans.*, 2023, **52**, 11222–11233.
12. M. A. Lemes, F. Magnan, B. Gabidullin, J. Brusso, *Dalton Trans.*, 2018, **47**, 4678–4684.
13. J. O. Moilanen, N. F. Chilton, B. M. Day, T. Pugh, R. A. Layfield, *Angew. Chem. Int. Ed.*, 2016, **55**, 5521–5525.
14. F. Neese, The ORCA Program System, *WILEY Interdiscip. Rev.: Comput. Mol. Sci.*, 2012, **2**, 73–78.
15. J. P. Perdew, J. Tao, S. Kummel, *ACS Symp. Ser.*, 2007, **958**, 13–25.
16. F. Weigend, R. Ahlrichs, *Phys. Chem. Chem. Phys*. 2005, **7**, 3297–3305.
17. J. D. Rolfes, F. Neese, D. A. Pantazis, *J. Comput. Chem*. 2020, **41**, 1842–1849.

18. F. Weigend, *Phys. Chem. Chem. Phys*. 2006, **8**, 1057–1065.

19. D. A. Pantazis, F. Neese, *J. Chem. Theory Comput*. 2009, **5**, 2229–2238.

20. F. Neese, F. Wennmohs, A. Hansen, U. Becker, *Chem. Phys.*, 2009, **356**, 98−109.

21. G. L. Stoychev, A. A. Auer, F. Neese, *J. Chem. Theory Comput*. 2017, **13**, 554−562.

22. T. Nakajima,K. Hirao, *J. Chem. Phys*. 2000, **113**, 7786−7789.

23. J. P. Perdew, J. Tao, S. Kummel, *ACS Symp. Ser.*, 958, **13**, (2007).

24. J. P. Perdew, K. Burke, M. Ernzerhof, *Phys. Rev. Lett*., 1996, **77**, 3865−3868.

25. J. M. Tao, J. P. Perdew, V. N. Staroverov, G. E. Scuseria, *Phys. Rev. Lett*., 2003, **91**, 146401.

26. M. Reiher, O. Salomon B. A. Hess, *Theor. Chem. Acc.* 2001, **107**, 48−55.

27. P. J. Stephens, F. J. Devlin, C. F. Chabalowski, M. J. Frisch, *J. Phys. Chem*. 1994, **98**, 11623−11627.

28. C. Adamo, V. Barone, *Chem. Phys. Lett*. 1997, **274**, 242−250.

29. C. Adamo, V. Barone, *J. Chem. Phys*. 1999, **110**, 6158−6169.

30. S. Grimme, J. Antony, S. Ehrlich, H. Krieg, *J. Chem. Phys*., 2010, **132**, 154104.

31. C. Angeli, R. Cimiraglia, S. Evangelisti, T. Leininger, J. P. Malrieu, *J. Chem. Phys*. 2001, **114**, 10252−10264.

32. D. Ganyushin, F. Neese, *J. Chem. Phys*., 2006, **125**, 024103.

33. F. Neese, *J. Chem. Phys*., 2005, **122**, 034107.

34. M. Atanasov, D. Ganyushin, K. Sivalingam, F. Neese, in Molecular Electronic Structures of Transition Metal Complexes II, ed. D. M. P. Mingos, P. Day and J. P. Dahl, Springer Berlin Heidelberg, Berlin, Heidelberg, 2012, pp. 149−220.

35. S. K. Singh, J. Eng, M. Atanasov, F. Neese, *Coord. Chem. Rev*., 2017, **344**, 2−25.

36. K. Yamaguchi, Y. Toyoda, T. Fueno, *Synth. Met*., 1987, **19**, 81

37. M. Shoji , K. Koizumi, Y. Kitagawa, T. Kawakami, S. Yamanaka, M. Okumura, K. Yamaguchi, *Chem. Phys. Lett*., 2006, **432**, 343–347